# Dynamics of episodic magma injection and migration at Yellowstone caldera: revisiting the 2004-2009 episode of caldera uplift with InSAR and GPS data

Francisco Delgado[1] and Raphael Grandin[2]

[1]Institut de Physique du Globe de Paris
[2]Université de Paris, Institut de physique du globe de Paris, CNRS

November 23, 2022

**Abstract**

The 2004-2009 caldera uplift is the largest instrumentally recorded episode of unrestat Yellowstone caldera. We use GPS and InSAR time series spanning 2004-2015, witha focus in the aforementioned event to understand the mechanisms of unrest. InSARdata recorded 25 and 20 cm of uplift at the Sour Creek (SCD) and Mallard Lake(MLD) resurgent domes during 2004-2009, and 8 cm of subsidence at the NorrisGeyser Basin (NGB) during 2004-2008. The SCD/MLD uplift was followed by sub-sidence across the caldera floor with a maximum at MLD of 1.5-2.5 cm/yr and nodeformation at NGB. The best-fit source models for the 2004-2009 period are two hori-zontal sills at depths of 8.7 and 10.6 km for the caldera source and NGB, respectively,with volume changes of 0.354 and -0.121 km3, and an overpressure of 0.1 MPa. TheInSAR and GPS time series record exponentially increasing followed by exponentiallydecreasing uplift between 2004 and 2009, which is indicative of magma injection intothe caldera reservoir. However, magma extractionfrom NGB to the caldera is unable to explain the subsidence coeval with the calderauplift. Models of magma injection can also explain other episodes of caldera uplift likethat in 2014-2015. Distributed sill opening models show that magma is stored acrossthe caldera source with no clear boundary between MLD and SCD. Since the magmaoverpressure is orders of magnitude below the tensile strength of the encasing rock,historical episodes of unrest like these are very unlikely to trigger an eruption.

# Dynamics of episodic magma injection and migration at Yellowstone caldera: revisiting the 2004-2009 episode of caldera uplift with InSAR and GPS data

**Francisco Delgado, Raphaël Grandin**

[1]Université de Paris, Institut de Physique du Globe de Paris, CNRS, F-75005 Paris, France

**Key Points:**

- We reanalyze all the InSAR and GPS data that span the 2004-2009 episode of unrest
- The GPS and InSAR time series record uplift with an exponential increase followed by an exponential decrease indicating magma injection
- Magma migration cannot explain subsidence at the Norris Geyser basin

Corresponding author: Francisco Delgado, `delgado@ipgp.fr`

**Abstract**

The 2004-2009 caldera uplift is the largest instrumentally recorded episode of unrest at Yellowstone caldera. We use GPS and InSAR time series spanning 2004-2015, with a focus in the aforementioned event to understand the mechanisms of unrest. InSAR data recorded ∼25 and ∼20 cm of uplift at the Sour Creek (SCD) and Mallard Lake (MLD) resurgent domes during 2004-2009, and ∼8 cm of subsidence at the Norris Geyser Basin (NGB) during 2004-2008. The SCD/MLD uplift was followed by subsidence across the caldera floor with a maximum at MLD of ∼1.5-2.5 cm/yr and no deformation at NGB. The best-fit source models for the 2004-2009 period are two horizontal sills at depths of ∼8.7 and 10.6 km for the caldera source and NGB, respectively, with volume changes of 0.354 and -0.121 $km^3$, and an overpressure of ∼0.1 MPa. The InSAR and GPS time series record exponentially increasing followed by exponentially decreasing uplift between 2004 and 2009, which is indicative of magma injection into the caldera reservoir, with no need for other mechanisms. However, magma extraction from NGB to the caldera is unable to explain the subsidence coeval with the caldera uplift. Models of magma injection can also explain other episodes of caldera uplift like that in 2014-2015. Distributed sill opening models show that magma is stored across the caldera source with no clear boundary between MLD and SCD. Since the magma overpressure is orders of magnitude below the tensile strength of the encasing rock, historical episodes of unrest like these are very unlikely to trigger an eruption.

## 1 Introduction

Silicic volcanoes ($SiO_2$ > 69%) are responsible for the largest explosive eruptions on Earth (VEI > 8, *Miller and Wark* (2008); *Bachmann and Bergantz* (2008)), more than two orders of magnitude larger than any eruption with recorded visual and instrumental observations. These eruptions form calderas that can remain restless even several hundreds of thousands of years after the climactic eruptions (e.g., *Hill et al.* (2020)). Several of these calderas undergo transient pulses or cycles of ground uplift followed by periods of either quiescence or ground subsidence (*Pelton and Smith*, 1979; *Dvorak and Berrino*, 1991). However, their relation to potential eruptive activity has remained elusive (e.g., *Pritchard et al.* (2019)). The advent of interferometric synthetic aperture radar (InSAR) geodesy in the early 1990s provided the first detailed images of the spatial and temporal complexities of these ground deformation cycles, which have been imaged at Yellowstone (*Wicks et al.* (1998, 2006); *Chang et al.* (2007), *Chang et al.* (2010)), Long Valley (*Fialko et al.*, 2001a; *Liu et al.*, 2011; *Montgomery-Brown et al.*, 2015), Campi Flegrei (*Lundgren et al.*, 2001; *Trasatti et al.*, 2015; *D'Auria et al.*, 2015), Santorini (*Parks et al.*, 2012), Laguna del Maule (*Feigl et al.*, 2014; *Le Mével et al.*, 2015), and Cordón Caulle (*Jay et al.*, 2014; *Delgado et al.*, 2016), (*Delgado et al.*, 2018)) volcanoes. These uplift events have velocities of ∼1-10 cm/yr, but can reach fast rates up to 28 - 45 cm/yr (*Feigl et al.*, 2014; *Delgado et al.*, 2016). The spatial and time scales of the deformation events vary from ∼15 km in Long Valley to more than 70 km at Yellowstone, and from ∼6 months for Cordon Caulle (*Delgado et al.*, 2018) up to at least half a century for Yellowstone (*Pelton and Smith*, 1979). These signals have been interpreted as being produced by either magma injection in shallow reservoirs (*Wicks et al.*, 2006; *Delgado et al.*, 2018; *Miller et al.*, 2017), volatile exsolution (*Dzurisin et al.*, 2012; *Hildreth*, 2017), fluid flow in the hydrothermal systems that are located in several of these systems (*Hurwitz et al.*, 2007a), viscoelastic relaxation (*Novoa et al.*, 2019) or a combination of these processes (*Dzurisin et al.*, 2012; *Tizzani et al.*, 2015). However, inherent ambiguities in the interpretation of the geodetic data and the lack of other constraining independent data sets like microgravity, gas chemistry, seismology and heat flow measurements have prevented scientists from unraveling the geological mechanism of ground uplift for most of them. Despite the diversity of monitoring data acquired in the past 40 years, recent studies that try to reconcile the wealth of geologic and geophysical data of Long Val-

ley (*Hildreth*, 2017; *Hill et al.*, 2020) and Campi Flegrei (*Troise et al.*, 2019; *D'Auria et al.*, 2015) calderas show no agreement upon the driving mechanism of unrest.

Understanding of these unrest signals requires a thorough knowledge of the processes that occur inside these magma reservoirs. For instance, most of the models available for modeling ground deformation data assume injection of fluid magma with Newtonian viscosity into a pressurized cavity (*Lengline et al.*, 2008; *Le Mével et al.*, 2016). Other models incorporate volatile exsolution instead of magma pressurization resulting in very similar uplift signals compared to those predicted by magma injection models (*Hurwitz et al.*, 2007a; *Hutnak et al.*, 2009; *Todesco et al.*, 2010). Viscoelastic models usually do not explicitly take magma injection into account (*Newman et al.*, 2006; *Delgado et al.*, 2018; *Novoa et al.*, 2019), but as they require a prescribed pressure function, the driving mechanism is likely magmatic up to the point when viscous relaxation dominates over the instantaneous elastic response. This is in contrast with the current understanding of the plumbing system of silicic volcanoes as crystal mushes, in which reservoirs are not molten but solid sponge-like bodies with pores filled with interstitial fluids and melt (*Bachmann and Bergantz*, 2008; *Bachmann and Huber*, 2016; *Cashman et al.*, 2017; *Cooper*, 2017). These mushes have a protracted growth history by episodic amalgamation of a stack of sill-shaped reservoirs (*Annen*, 2009; *Annen et al.*, 2015), and spend most of their lifetime below their solidus under cold storage conditions (*Cooper and Kent*, 2014; *Rubin et al.*, 2017). Crystal mushes are unlikely to produce a volcanic eruption unless they are thermomecanically unlocked and remobilized by many episodic pulses of magma injection (*Huber et al.* (2010), *Huber et al.* (2011)). However, thermomechanical remobilization is important only over long time scales of $10^2$-$10^3$ years, while on short time scales of $10^0$-$10^1$ years magma injection is the principal triggering mechanism of rhyolitic eruptions (*Huber et al.* (2011), *Huber et al.* (2012); *Degruyter and Huber* (2014); *Townsend et al.* (2019)). Other views indicate that unrest on time scales of $10^0$-$10^1$ years at large silicic systems may also be explained by melt amalgamation resulting from the inherent instability of buoyant melt layers (*Sparks et al.*, 2019). Other views that consider non-magmatic processes suggest that caldera unrest results from a combination of magma injection, volatile exsolution and/or crystallization and degassing of large magma batches without new inputs of magma. Caldera uplift is then punctuated by episodic leaks of fluids from below the brittle-ductile transition (BDT) to shallow areas that deform in a brittle way (*Fournier*, 2007). Further, seismic and geodetic data show that episodes of uplift resulting from likely magma injections are transient features and can be separated by many years (*Delgado et al.*, 2018; *Druitt et al.*, 2019) or even decades (*Sigmundsson et al.*, 2010; *Druitt et al.*, 2019) without any other clear evidence for unrest. Other views suggest that caldera resurgence is the direct consequence of episodic magma injection resulting from the incremental and protracted growth of plumbing systems. The episodic uplift is interrupted by episodes of deflation but the net result is uplift (*Acocella*, 2019). Regardless of the mechanism of unrest, a key question in volcano science still remains and has direct implications for models of hazard: when do these pulses of uplift imply a potential eruption? (e.g., *Pritchard et al.* (2019)).

If these uplift events are in turn produced by magma injection, how many of them and of what magnitude are required to actually trigger an eruption? Unfortunately, some models used to study active intrusions (*Lengline et al.*, 2008) do not have predictive capabilities and cannot predict the maximum stress in the reservoir walls produced by magma injection. This is a necessary element in eruption forecasting models because the rupture threshold for dike propagation towards the surface depends upon the reservoir pressure. Dikes form when the deviatoric hoop stress in the reservoir walls reaches a threshold above the tensile strength of the rock which is known to be within ~1-40 MPa (*Tait et al.*, 1989; *Albino et al.*, 2010). Nonetheless, given our imperfect knowledge of the shallow reservoir location, size and physicochemical state, the exact rupture threshold is unknown. Furthermore, the maximum pressurization

that reservoirs sustain before an eruption likely varies throughout the lifetime of a single edifice and between different volcanoes (*Lu et al.*, 2003; *Pinel et al.*, 2010; *Carrier et al.*, 2015).

In this study we focus on the episode of unrest during 2004-2009 at Yellowstone (*Chang et al.* (2007), *Chang et al.* (2010)), the fastest ever recorded at that volcano since systematic geodetic measurements started in 1975 (*Pelton and Smith*, 1979). Despite more than 4 decades of geodetic observations, there is still significant uncertainty on the driving mechanisms of ground deformation (*Dzurisin et al.*, 2012; *Hurwitz and Lowenstern*, 2014). For example, a detailed conceptual model does not assess the relative contributions of basalt injections and exsolved volatiles (*Dzurisin et al.*, 2012). We test the hypothesis of whether the 2004-2009 episode of unrest was caused by magma injection or other mechanisms, and particularly the nature of the fluids involved in the episodes of unrest (*Hurwitz et al.*, 2007a; *Dzurisin et al.*, 2012). To assess these questions, we use all the continuous GPS and all the ENVISAT InSAR data that recorded the complete 2004-2009 episode of uplift with improved source models of ground deformation and solid-fluid mechanics models of magma injection. These models are a function of the magma viscosity, magma compressibility and conduit radius among other parameters, and can predict the time series of ground deformation (e.g., *Lengline et al.* (2008); *Le Mével et al.* (2016); *Delgado et al.* (2018)). We compare the deformation data and models with other seismic swarms in December 2008 (*Farrell et al.*, 2010) and January 2010 (*Shelly et al.*, 2013) and discuss mechanisms of transition from caldera uplift to subsidence. We finally extend our models to the most recent periods of unrest during 2014-2015 (*Wicks et al.*, 2020).

## 2 Geological and ground deformation background of Yellowstone caldera

Yellowstone caldera is a $\sim$85$\times$45 km$^3$ topographic depression and is the youngest of three collapse calderas in the Yellowstone plateau. The eruptions that formed these calderas occurred 2.1, 1.3 and 0.64 Myrs ago erupting the Huckleberry Ridge, Mesa Falls and Lava Creek Tuffs with erupted volumes larger than 2450, 280 and 1000 km$^3$ respectively (*Christiansen*, 2001). The last of these eruptions formed the current Yellowstone caldera, which is now filled with 600-1000 km$^3$ of post caldera rhyolitic lava flows. Post caldera volcanism has been focused on the Sour Creek and Mallard Lake domes (SCD and MLD hereafter) (Figure 1) which have been active for the past 0.164 Myrs (*Christiansen*, 2001). The caldera is underlain by a large plumbing system with large but spatially variable contents of melt (*Farrell et al.*, 2014; *Huang et al.*, 2015; *Schmandt et al.*, 2019). Yellowstone hosts the largest hydrothermal system in the world with half of the world's geysers (*Hurwitz and Manga*, 2017) and several hundreds of hydrothermal vents (*Fournier*, 1989; *Lowenstern and Hurwitz*, 2008; *Hurwitz and Lowenstern*, 2014). On a geological time scale, the VEI 8 eruptions and the large hydrothermal activity are fuelled by large batches of basalt injection under the upper to mid-crustal silicic system, evidenced by a very large $CO_2$ degassing flux. This requires that the injecting basaltic magma has a $CO_2$ concentration of 400-500 ppm. Such a large amount of $CO_2$ cannot be dissolved in silicic melts because it would be completely exhausted in 1000 years. Mass balances indicate that $\sim$0.3 km$^3$/yr of basaltic melts are intruded beneath the caldera, a similar amount to that intruded at the Hawaii hot spot (*Lowenstern and Hurwitz*, 2008; *Lowenstern et al.*, 2015). These injections are also the ultimate source of caldera unrest (*Wicks et al.*, 2006; *Dzurisin et al.*, 2012).

### 2.1 Observations and models of caldera unrest

A summary of geodetic observations of ground deformation between 1923 and 2008 is described in detail in *Dzurisin et al.* (2012). Ground deformation was observed

for the first time in 1975 when leveling lines were measured after 1923 recording 0.7 m of uplift, with a time-averaged rate of ~1.4 cm/yr (*Pelton and Smith*, 1979). Systematic time-lapse leveling started in 1983 until 2007, and showed that the caldera floor uplifted until 1984 when the uplift shifted to subsidence following the largest historical swarm ever measured at Yellowstone with $M_C$ magnitudes up to 4.9 (*Waite and Smith*, 2002). Caldera subsidence continued until 1996 when a 1 year long episode of caldera uplift was recorded (*Wicks et al.*, 1998). Coevally, the area of Norris Geyser Basin (NGB hereafter) uplifted between 1996 and 2000 (*Wicks et al.*, 2006). Continuous GPS monitoring started in 1996 with a five-fold increase in the station density in 2000 (Figure 1). In July 2004, the whole caldera floor uplifted in the largest episode of historic unrest with a maximum uplift rate of 7 cm/yr and with subsidence at rates of 2 cm/yr at NGB (*Chang et al.* (2007), *Chang et al.* (2010)). The caldera uplift ended in late 2009, coevally with another seismic swarm in the NW part of the caldera (*Shelly et al.*, 2013). More recent episodes of unrest include uplift at NGB between December 2013 and March 30 2014, subsidence at NGB and uplift at the caldera between March 2014 and early 2015, and NGB uplift and caldera subsidence up until the present (*Dzurisin et al.*, 2019; *Wicks et al.*, 2020) (Figure 1). The transition from uplift to subsidence usually occurs with large seismic swarms at the distal parts of the caldera (*Waite and Smith*, 2002; *Shelly et al.*, 2013).

Previous InSAR studies have focused on ERS-1/2 data to measure caldera floor subsidence during 1992 to 1995, slight caldera floor uplift during 1995-1996, uplift at NGB during 1996-2000 (*Wicks et al.*, 1998, 2006; *Dzurisin et al.*, 1999; *Dzurisin and Lu*, 2007; *Vasco et al.*, 2007; *Aly and Cochran*, 2011; *Dzurisin et al.*, 2012; *Tizzani et al.*, 2015; *Dzurisin et al.*, 2019; *Wicks et al.*, 2020), caldera uplift with ENVISAT during 2004-2009 (*Chang et al.* (2007), *Chang et al.* (2010), *Aly and Cochran* (2011), *Dzurisin et al.* (2012), *Tizzani et al.* (2015)), and NGB uplift, subsidence and then uplift with TerraSAR-X and Sentinel-1 data during December 2013 - March 2014, March 2014 - early 2015 and then 2016 - 2017 respectively (*Dzurisin et al.*, 2019; *Wicks et al.*, 2020). Despite the good quality of the InSAR observations, all the previous studies have used a few interferograms only that provide individual snapshots of the individual episodes of unrest. The only exception is *Tizzani et al.* (2015) who calculated an InSAR time series with a descending ERS/ENVISAT track for 1992-2010.

## 3 Data analysis and deformation results

### 3.1 InSAR and GPS data analysis

We use GPS data from the stations WLWY, LKWY, OFW2, HVWY and NRWY operated by the University of Utah and the EarthScope Plate Boundary Observatory, and processed by the Nevada Geodetic Laboratory. (Figure 1, Figure S1). These stations record the record the complete sequence of uplift and subsidence during 2004-2009 (Figure 1). We use InSAR data from the C-band ERS-1/2, ENVISAT, L-band ALOS and X-band TerraSAR-X satellites (Table 1) processed as both individual interferograms and InSAR time series depending upon the satellite platform, and data temporal resolution (Figure 2 - Figure 3, Figures S2-S5). Data processing follows standard procedures for time series analysis (e.g., *Doin et al.* (2011)) and is described in detail in the supplementary material. We calculate InSAR time series for the ENVISAT data, and from this product we extract the cumulative ground deformation during the episode of uplift as the difference in deformation between the last image in 2009 and the first image in either 2004 or 2005 (Table 1). These data span the complete episode of caldera uplift and are hereafter referred as interferograms. For the TSX data we stack the data and instead calculate rate maps of mean ground velocity (supplementary material).

### 3.2 2004 - 2009 deformation

Despite the different amount of SAR images and the variable interferogram quality in the different ENVISAT tracks, each of the time series record a total of ∼25 and ∼20 cm of line-of-sight (LOS) uplift at SCD and MLD between September 2004 and September 2009 (Figure 2 - Figure 3). The InSAR data also record ∼8 cm of subsidence at the NGB between 2004 and 2008 – one year before the end of the uplift at the resurgent domes (Figure 3). The wavelength of the deformation signals at SCD, MLD and NGB is constant during 2004-2009 and does not change during the recorded time span, indicating that the sources causing deformation do not change in depth (not shown). The GPS stations OFW2 located near the MLD, and the stations HVWY, LKWY and WLWY located near the SCD record between ∼10 and 20 cm of uplift during the same time span, in agreement with them being at variable distances from the areas of maximum uplift (Figure 1). The deformation signals are similar in location and wavelength to those analyzed in previous studies (*Chang et al.* (2007), *Chang et al.* (2010); *Aly and Cochran* (2011); *Tizzani et al.* (2015); *Wicks et al.* (2020)). A seismic swarm that occurred in December 2008 and was detected by the LKWY station (*Farrell et al.*, 2010) is not observed by the InSAR data because we do not include winter images and because the geodetic signals it produced are below the InSAR uncertainty. No clear evidence of localized fault creep triggered by magmatic deformation was observed on any of the InSAR time series. The onset of deformation cannot be assessed from the InSAR data because there are only two non-winter images in 2004 (Figure S2). Both the GPS data for stations OFW2, HVWY, LKWY and WLWY and InSAR time series during 2004-2009 display a pattern of uplift in which deformation increases exponentially until a threshold is reached and followed by an exponential decrease (Figure 1, Figure 2, described later). This exponential increase followed by exponential decrease is referred to hereafter as double exponential (*Le Mével et al.*, 2015).

### 3.3 2010 - 2013 deformation

The caldera uplift transitioned to subsidence in January 2010 until December 2013. The GPS data recorded this with a constant rate of ∼1.5 cm/yr, but only the ENVISAT IM2 descending data recorded it (Figure 2C), with an average subsidence of 1-2 cm. ALOS-1 interferograms display double-bounce signals in wetlands that introduce abrupt phase discontinuities (e.g., *Wdowinski and Hong* (2015)) and phase unwrapping errors that cannot be corrected. This data shows no deformation during 2010-2011, so it is not considered further in this study (Figure S5). The maximum caldera subsidence is at MLD instead of SCD, with a maximum of -3.5 to -2 cm/yr depending on the track and on the amount of data used in the stacks. The caldera deformation pattern of the January 2010 - December 2013 subsidence is significantly different to that of the 2004-2009 uplift (Figure 2F, G). The TSX and GPS data record no deformation at NGB during this time span.

## 4 Kinematic source modeling

To understand the sources responsible for the ground deformation at Yellowstone, we jointly invert the 2004-2009 interferograms and the GPS vectors with two sources. These include a tensile dislocation (*Okada*, 1985) representing an opening sill below the caldera floor plus an additional source to model the deflation below the NGB – either a pressurized small sphere (*McTigue*, 1987) or another tensile dislocation. We note that the combination of two Okada sills neglects the mechanical interaction between them (*Pascal et al.*, 2014), but from a computational point of view it is much faster to implement than a numerical model calculated with either finite or boundary element methods. We do not invert the 2010-2013 deformation data because the

TSX and the GPS data show velocity differences up to ∼50%. The wavelength of the deformation signals are on the order of of several tens of kilometers, suggesting that the deformation sources are likely to lie below the BDT. However, *Tizzani et al.* (2015) has shown that viscoelastic effects representative of viscous rheologies are only relevant for time scales longer than 580 years which are well below the time span of ∼5 years considered in this study. The interferograms were downsampled with a resolution-based algorithm (*Lohman and Simons*, 2005). Data were inverted with the neighborhood algorithm *Sambridge* (1999) (hereafter NA), a non-linear inversion method which iteratively searches for the best-fit model parameters avoiding local minima, and the Levenberg-Marquardt (LM) algorithm to search for global best-fit model. The inversion procedure is described in detail in the supplementary material.

### 4.1 Uniform opening model

The model of a horizontal sill below the caldera floor and a depressurized sphere below NGB do not produce a fit as nearly as good compared to that of two dislocations. Therefore we focus on a model of two Okada sills only. The best-fit geometry is made up of two horizontal sills (Figure 4, Table 2) at depths of 8.7 km for the caldera sill and 10.6 km for the NGB sill (Figure S6). The vertical components of the WLWY, LKWY and OFW2 stations are almost insensitive to the closing of the NGB sill (Figure S7), therefore the time series of vertical displacement of these stations are proportional to the caldera sill opening. The sill centroid depths uncertainties are in Figure S8.

The Okada model does not include the pressure change as a model parameter so we follow two approaches to estimate it. First, the area of the caldera source sill ($\sim 58 \times 19$ km$^2$) can be roughly approximated by that of three penny-shaped cracks with a radii $a = 9.7$ km for each one. Then, we use the formula $\Delta V = \frac{8}{3} a^3 (1-\nu) \frac{\Delta P}{G}$ (*Fialko et al.*, 2001b) to get an order of magnitude of the sill pressure change. This approach is just a very coarse approximation and does not imply that an Okada volume change is directly comparable to that of a pressurized penny-shaped crack. Using a volume change of $\Delta V \sim \frac{0.354}{3}$ km$^3$ for each of these sources, a Poisson ratio $\nu = 0.25$ and a shear modulus of $G = 2.1$ GPa (*Heap et al.*, 2020) we get a source overpressure of 0.13 MPa. Second, we use the boundary element software DEFVOLC (*Cayol and Cornet*, 1997) to calculate the source overpressure (supplementary information). This model predicts sill depths of 14 and 17.5 km for the caldera and NGB sources respectively, and a pressure change of ∼0.08 MPa, which is 60% of the value inferred from the crack approximation (Figure S9). These sources are much deeper than those inferred from the inversion of the Okada models. The overpressure for both models are several orders of magnitude below the tensile strength of the encasing rocks of 10-40 MPa (e.g., *Albino et al.* (2010)).

### 4.2 Distributed sill opening model

The inversion for dislocations with uniform opening results in non-negligible residuals near MLD and SCD (Figure S6), which potentially result from localized areas of fluid pressurization below the resurgent domes. To improve the data fit, we use a distributed sill-opening model for the caldera sill at a depth of 8.7 km (e.g., *Delgado et al.* (2018); *Henderson et al.* (2017)). In this model, the best-fit sill is augmented to 12×8 smaller sills, each one with an area of 5×5 km$^2$, and we enforce the constraint that the sill opening tapers to zero at its edges (Figure 4, Figure S10). The distributed opening model predicts volume changes for the caldera source of 0.354 km$^3$ during 2004-2009, 0.306 km$^3$ during 2005-2009, and a volume decrease for the NGB source of -0.121 km$^3$ and -0.0981 km$^3$ for the same time periods respectively. The time-averaged caldera sill opening is 0.07 km$^3$/yr. The distributed opening models show no clear boundary between the zones of volume change beneath SCD and MLD (Figure 5). A residual of ∼5 cm is observed in the E part of Yellowstone Lake par-

ticularly in the ascending interferograms and could be related to the December 2008 seismic swarm (*Farrell et al.*, 2010).

### 4.3 Temporal evolution of the sill opening model

The vertical components of the five GPS stations were inverted for the caldera sill opening and NGB sill closing models for every epoch to retrieve the cumulative volume change of the uniform opening model (Figure 6).

## 5 Dynamic source modeling

Kinematic source models like the aforementioned two sills do not provide insights on the physical mechanism driving the caldera uplift. In this study we focus solely on the mechanism of magma injection from a deep source to a shallow source because there are simple analytic formulas that can be compared directly with ground deformation time series (*Lengline et al.*, 2008; *Le Mével et al.*, 2016). Although the reviews of *Dzurisin et al.* (2012) and *Lowenstern et al.* (2015) suggest the role of both hydrothermal and magmatic fluids, including exsolved volatiles from cooling magma, in this study we neglect these effects. Hereafter we refer to magma as molten rock with a Newtonian viscosity. This is a clear oversimplification of the very complex hydrothermal-magmatic system of Yellowstone, but it is necessary to assess to what extent ground deformation can be explained by one of these end-member models. In the following we consider two cases. First, an analytic model of magma injection below Yellowstone caldera. Second, a new analytic model of magma injection below Yellowstone caldera from both a mantle source and from the reservoir below NGB.

### 5.1 A pressurized reservoir connected to a mantle magma source

We start with a magma injection model in which the caldera reservoir is connected to a magma source in the mantle, whose source pressure function increases linearly until a threshold $t^*$ when it reaches a constant. Magma ascends due to its overpressure and pressurizes the shallow reservoir, resulting in a double exponential function for both the reservoir overpressure and the ground displacement (*Le Mével et al.*, 2016). This model does not take into account the potential connection between NGB and the caldera source, which is addressed later in the study.

#### *5.1.1 Mathematical background*

The magma injection model is defined by Equation 1- Equation 2.

$$P(t) = \begin{cases} \frac{st}{t^*} + (s\tau_p - \Delta\rho g L)(e^{\frac{-t}{\tau_p}} - 1) & 0 < t < t^* \\ st(\frac{\tau_p}{t^*} e^{\frac{-t}{\tau_p}} - \frac{\tau_p}{t^*} e^{\frac{-(t-t^*)}{\tau_p}} + 1) & t > t^* \end{cases} \tag{1}$$

$$\tau_p = \frac{8\eta L V(\beta_w + \beta_m)}{\pi R^4} \tag{2}$$

Here, $P(t)$ is the pressure in the deeep mantle source, $t^*$ is the transition time between linear increasing and constant deep pressurization, $\tau_p$ is a constant that depends on the properties of the plumbing system, $R$ is the conduit radius, $L$ is the conduit length, $V$ is the reservoir volume, $\beta_w$ and $\beta_m$ are the reservoir and magma compressibility, $s$ is the pressurization rate, $\Delta\rho$ is the density difference between the magma and host rock, and $g$ is the garvity acceleration. Since the source pressure is proportional to the displacement for pressurized cavities embedded in a linear-elastic half-space (*McTigue*, 1987), the model can be scaled with an arbitrary constant to

model the GPS time series (e.g., *Henderson et al.* (2017)). In this case, $P(t)$ is an adimensional pressure function because there is no analytic expression to convert the pressure to displacement with the Okada model. Further, if no changes occur in the plumbing system, like a change in the source geometry, then transient changes in the time series are direct evidence of transient changes in the reservoir pressure and ultimately in the deep source pressure function. As stated earlier, the InSAR data does not show changes in the wavelength of the deformation signals so the sources are fixed in depth. This way, we know that changes in the time series do not result from changes in the source geometry. Nevertheless, the magma composition cannot be estimated without inferences on the conduit radius (e.g., *Pedersen and Sigmundsson* (2006); *Fukushima et al.* (2010); *Delgado et al.* (2018)) and the source volume (*Segall*, 2019), the latter of which is not available from the Okada model.

#### *5.1.2 Inverse models*

Inversions for the best-fit magma injection model using the InSAR and the vertical component of the WLKY GPS time series for the SCD predict similar time constants (Figure 7a), but a shorter transition for the InSAR-derived model parameters. This is due to the lack of InSAR data between September 2004 and May 2005 and the higher uncertainty of InSAR with respect to GPS. Therefore, the InSAR data are not considered further for these dynamic models. If the GPS stations record deformation produced by a single source, then the source pressure function is the same for all of them. The only difference between the time series is the deformation amplitude which is a function of the source geometry and is a constant for each GPS station. Hence the time series can be normalized to account for this constant (Figure 7b). The best-fit magma injection model with no buoyancy ($\Delta\rho = 0$) for the normalized vertical component of the WLWY, LKWY and OFW2 stations predicts a transition time of 0.66 years and an exponential time constant of 4 years, with a final adimensional amplitude of 1.37. The magma injection model predicts significant ground uplift for at least 5 additional years should inelastic effects be absent. The magma injection model is also applied to GPS time series during 2014-2015, when fast uplift at NGB transitioned to subsidence following a Mw 4.9 earthquake on March 30 2014. The model results in good data fits (Figure 8), but the prediction of a double exponential is nearly identical to that of the single exponential model. In this latter model the pressure in the deep magma source is constant during the whole episode (*Lengline et al.*, 2008). The InSAR and GPS data and the magma injection model suggest that caldera uplift at Yellowstone during 2004-2009 and 2014-2015 is directly indicative of magma injection into the caldera source with no need for pressurization due to volatile exsolution at the top of the plumbing system or at the bottom of the shallow hydrothermal system. This is in contradiction with a hybrid model of magma injection and volatile exsolution (*Dzurisin et al.*, 2012). The magma injection model also ignores the contemporary deflation at NGB, which we address in the following section.

### 5.2 Two pressurized reservoirs connected to a mantle magma source

The geodetic data show that uplift at the caldera floor is coeval to subsidence at the NGB during most of the 2004-2009 episode of unrest, and that two sub-horizontal sills are responsible for the deformation signals. In this section we use a simple fluid-solid mechanics model based on mass conservation to unravel the potential connection between these two sources of deformation. We test the hypothesis that uplift at the caldera can be explained by magma injection from both the mantle and the NGB sources (Figure 9). As our goal is to provide a simple physical model that allows us to understand, not model the GPS time series, we make several geometrical and mechanical simplifications.

The model of magma flow for two deformation sources embedded in a homogeneous linear elastic half-space is based on a mass balance that couples the reservoirs volume and pressure changes with the Poiseuille flow law. These equations are presented in previous studies (*Lengline et al.*, 2008; *Segall*, 2013; *Reverso et al.*, 2014; *Le Mével et al.*, 2016; *Walwer et al.*, 2019) and we adapt them for the specific case of Yellowstone. We do consider the effect of magma compressibility due to variations in the reservoir pressure (*Rivalta*, 2010). More complex rheologies like elastic layering, viscoelasticity or other mechanisms of fluid transfer such as flow in a poroelastic media (*Hurwitz et al.*, 2007a) are not considered in this study. Also, the model considers neither the mechanical interaction between the sources (*Pascal et al.*, 2014) nor the lateral offset between the sill centroids which are not symmetric and do not lie on top of each other. We assume that since the sources are very large, these boundary effects have a secondary effect. For simplicity we also neglect the short time lag between the onset of inflation at SC and ML and the deflation at NGB. We also neglect the complexity of Yellowstone's plumbing system inferred from seismic tomography (*Farrell et al.*, 2014; *Huang et al.*, 2015), including large areas of partial melt and multiphase components in the magma (crystals, dissolved and exsolved $CO_2$ and $H_2O$). We also neglect the lateral magma transfer and storage between SCD and MLD (Figure 5), because these effects are of secondary order with respect to a single zone of magma accumulation along the two domes (Figure 4, Figure S6). Since the pressure is proportional to the displacement in a linear elastic half-space, ground deformation follows the same trend as the source pressure function.

#### *5.2.1 Mathematical background*

The volume change rate in the two reservoirs connected with each other, were one of them is fed by a mantle magma source (Figure 9), is derived from mass conservation and is given by Equation 3 - Equation 4 (e.g., *Reverso et al.* (2014); *Walwer et al.* (2019))

$$\frac{d\Delta M_s}{dt} = \rho_m \frac{d\Delta V_s}{dt} = \rho_m (Q_{in} + Q) \tag{3}$$

$$\frac{d\Delta M_d}{dt} = \rho_m \frac{d\Delta V_d}{dt} = -\rho_m Q_{in} \tag{4}$$

with $\Delta M_s, \Delta M_d$ the mass change in the shallow ($_s$) and deep reservoirs ($_d$), $\rho_m$ the magma density, $\Delta V_s, \Delta V_d$ the volume change in the shallow and deep reservoirs, $Q$ the volume flux from a deep mantle source, and $Q_{in}$ the volume flux from the NGB to the caldera source reservoir. Here the shallow and deep reservoirs represent the caldera source and the NGB sill-like sources. The relation between the volume change $\Delta V_{s,d}$ and the resulting reservoir overpressure $\Delta P_{s,d}$ under the assumption that magma is incompressible and the density is constant is Equation 5

$$\Delta V_{s,d} = \Delta P_{s,d} \frac{\pi a_{s,d}^3 \gamma}{G} \tag{5}$$

with $\gamma$ equal to 1 for a sphere (*McTigue*, 1987) and $\frac{8(1-\nu)}{3\pi}$ for a penny-shaped crack (*Fialko et al.*, 2001b), $G$ the shear modulus and $a_{s,d}^3$ the sphere/crack radius.

The volume flux in a vertical conduit connecting a mantle magma source $\Delta\bar{P}$ to a shallow source $\Delta P_s$ is given by the Poiseuille law in Equation 6

$$Q = \frac{\pi a^4}{8\mu H} (\Delta\rho g H + \Delta\bar{P} - \Delta P_s) \tag{6}$$

with $a$ the conduit radius, $\mu$ the magma viscosity, $H$ the conduit length, $\Delta\rho$ the magma-host rock density contrast, $g$ the gravitational acceleration and $\Delta\bar{P}$ the mantle magma pressure (*Jaupart and Tait*, 1990; *Lengline et al.*, 2008). The expression is nearly identical for the conduit connecting the shallow and the deep source in Equation 7

$$Q_{in} = \frac{\pi a_2^4}{8\mu_2 H_2}(\Delta\rho_2 g H_2 + \Delta P_d - \Delta P_s) \tag{7}$$

with $H_2$, $a_2$ and $\mu_2$ the conduit length, radius and magma viscosity and $\Delta P_d$ the deeper reservoir pressure. Here the flow from the deep reservoir depends upon the pressure gradient (*Segall*, 2013) instead of a constant magma flow (*Reverso et al.*, 2014). Combining Equation 3 - Equation 7 results in two equations for the pressure change of the two pressurized reservoirs (Equation 8 - Equation 9).

$$\frac{d\Delta P_s}{dt} = \frac{a_2^4 G}{8\mu_2 H_2 a_s^3 \gamma}(\Delta\rho_2 g H_2 + \Delta P_d - \Delta P_s) + \frac{a^4 G}{8\mu H a_s^3 \gamma}(\Delta\rho g H + \Delta\bar{P} - \Delta P_s) \tag{8}$$

$$\frac{d\Delta P_d}{dt} = -\frac{a_2^4 G}{8\mu_2 H_2 a_d^3 \gamma}(\Delta\rho_2 g H_2 + \Delta P_d - \Delta P_s) \tag{9}$$

We set

$$\begin{aligned} \tau_2^{-1} = \beta &= \frac{a_2^4 G}{8\mu_2 H_2 a_s^3 \gamma} \\ \tau_1^{-1} = \alpha &= \frac{a^4 G}{8\mu H a_s^3 \gamma} \\ \tau_3^{-1} = \epsilon &= \frac{a_2^4 G}{8\mu_2 H_2 a_d^3 \gamma} \end{aligned} \tag{10}$$

Instead of a piecewise mantle source pressure function of a linear increase followed by a constant after a time threshold (*Le Mével et al.*, 2016), we use an exponential function of the form $\Delta\bar{P} = \bar{P}(1 - e^{-\frac{t}{\tau_m}})$ because it is easier to integrate. We use $\tau_m = 0.36$ years from the data (Figure 7).

The solution method is outlined in the supplementary material. The final solution for initial conditions $P_s(0) = 0, P_d(0) = P_{d_0}$ is Equation 11

$$\begin{bmatrix} \Delta P_s \\ \Delta P_d \end{bmatrix} = C_1 e^{\lambda_1 t}\begin{bmatrix} 1 + \frac{\lambda_1}{\epsilon} \\ 1 \end{bmatrix} + C_2 e^{\lambda_2 t}\begin{bmatrix} 1 + \frac{\lambda_2}{\epsilon} \\ 1 \end{bmatrix} + \begin{bmatrix} a_1 \\ a_2 \end{bmatrix} e^{-\frac{t}{\tau_m}} + \begin{bmatrix} b_1 \\ b_2 \end{bmatrix} \tag{11}$$

with the eigenvalues $\lambda_{1,2}$

$$\lambda_{1,2} = \frac{-(\alpha + \beta + \epsilon) \pm \sqrt{(\alpha^2 + \beta^2 + \epsilon^2 + 2\alpha\beta + 2\beta\epsilon - 2\alpha\epsilon)}}{2} \tag{12}$$

and constants

$$\begin{aligned} b_1 &= \bar{P} + \Delta\rho g H \\ b_2 &= \bar{P} + \Delta\rho g H - \Delta\rho_2 g H_2 \\ C_1 &= P_{d_0} - (C_2 + a_2 + b_2) \\ C_2 &= \epsilon\frac{(P_{d_0} - a_2 - b_2)(1 + \lambda_1/\epsilon) + a_1 + b_1}{\lambda_1 - \lambda_2} \end{aligned} \tag{13}$$

Here $P_{d_0}$ is the overpressure produced by injection of basaltic magma at the NGB reservoir during 1996-2000 (*Wicks et al.*, 2006). Since basaltic magma is unlikely to significantly cool to produce a significant density and viscosity change in 4 years, for simplicity we assume that $\Delta\rho = \Delta\rho_2$, $\mu = \mu_2$.

The selected model parameters are in Table 3. Since there are no geophysical constraints on the fourth power of the conduit radius $R^4$ and the viscosity of the injecting basalt $\mu$, we parametrize the model in terms of the conduit conductivity $\bar{c} = R^4/\mu$ (*Anderson and Segall*, 2013). Basaltic melts have viscosities of $10 - 10^2$ Pa s (*Giordano and Dingwell*, 2003) and conduit flow models during episodes of unrest in basaltic volcanoes show radii of ∼1 m (*Pedersen and Sigmundsson* (2006); *Fukushima et al.* (2010)), resulting in $\bar{c} \sim 0.1 - 0.01 \frac{m^4}{Pas}$. The initial pressure with respect to lithostatic conditions are $P_s^0 = 0$ MPa and $P_d^0 = 0 - 0.5$ MPa, the latter value arising from the potential magma injection at NGB during 1996-2000 (*Wicks et al.*, 2006). The amplitude of the source pressure just scales the pressurization of the reservoirs, so it is not relevant since we are interested in the temporal evolution of the reservoir pressures. We consider cases with and without a magma density difference, in which the magma ascends due to its overpressure and due to the combined overpressure and buoyancy effects.

### *5.2.2 Forward models*

The simulations show that magma ascent due to its overpressure predicts double exponential pressure functions for both the caldera and the NGB sources, albeit with a lower amplitude for the latter (Figure 10a-b). For $P_d^0 = 0$ MPa, the model cannot predict a linear depressurization for the NGB source. The model implies that magma ascends from the mantle to the shallow reservoir, and then the high magma overpressure drives magma 2 km down into the NGB reservoir, which is unrealistic. Magma compressibilities for a gas-poor basalt have a second order effect and do not change the predicted pressure change (not shown), but increasing the magma compressibility significantly increases the amount of intruded magma (e.g., Figure 9 in *Le Mével et al.* (2016)). When magma ascends due to its buoyancy and overpressure, the model predicts double exponential pressurization at the caldera source and both depressurization and pressurization at NGB with near linear trends (Figure 10c-d). We note that the magnitude of the pressurization of the buoyancy and overpressure model is one order of magnitude larger than the model with magma overpressure only.

The only possibility to significantly depressurize the NGB source due to magma flow to the caldera source is to set $P_d^0 = 0 = 0.5$ MPa (Figure 11b,f) and with $\bar{c} \sim 10^0 \frac{m^4}{Pas}$ or smaller. As this value is increased, the magnitude of the subsidence decreases in response to a better hydraulic connection. The simulation predicts depressurization at NGB and double exponential pressurization at the caldera, but eventually all the subsidence from material extracted from NGB is counterbalanced by the fluid influx from the caldera source to NGB. The MBEM model predicts $\Delta P$ ∼0.08 MPa for the caldera source, so it is very unlikely that the NGB reservoir overpressure reached 0.5 MPa during the 1996-2000 episode of unrest because uplift during that time span was much lower than the caldera uplift during 2004-2009 (Figure S4, Figure 2). This implies that the NGB reservoir should have been pressurized decades before 1996, which is a geologically plausible scenario (*Wicks et al.*, 2020), but for which we have no quantitative constraints.

An alternative model considers that the mantle magma source is located below NGB instead below the caldera. Here magma ascends to NGB, and then from NGB to the caldera sill (*Reverso et al.*, 2014), potentially resulting in depressurization during several years at NGB. In this case the second term in the right hand side of Equation 8 must be moved in the right hand side of Equation 9, after switching $\Delta P_s$ with $\Delta P_d$

and modifying the time constant of this term with factors appropriate for the NGB reservoir. We also assume a slight overpressure for the NGB source. In this model the NGB source deflates for ∼1.5 years, while the caldera source inflates with an exponential. Afterwards, both sources linearly inflate (not shown), which does not match the trends recorded in the GPS data.

Regardless of the model, none of these simulations can predict at the same time the trends observed in the InSAR and GPS time series at both the caldera floor and NGB and with a constrained set of assumptions available since geodetic measurements only started in 1975.

# 6 Discussion

## 6.1 Source models and comparison with previous studies

Two families of source models have been proposed for the 2004-2009 episode of unrest: those that rely on horizontal dislocations (*Chang et al.* (2007), *Chang et al.* (2010); *Wicks et al.* (2020), this study) and those that use a combination of pressure sources (*Aly and Cochran*, 2011; *Tizzani et al.*, 2015). Although both types of models can fit the data well, we consider that the dislocations are more realistic. First, they require less model parameters. Second, neglecting the mechanical interaction between two sills is less inaccurate than neglecting the interaction between at least three pressure sources (*Aly and Cochran*, 2011; *Tizzani et al.*, 2015). Our results are similar to those of *Chang et al.* (2007) and *Chang et al.* (2010) who also found two rectangular dislocations at depths of ∼7-10 and ∼7-13 km for the caldera and NGB sources, albeit modeling very small data sets. The caldera source model is located at the top of the low $V_P$ zone below the caldera imaged with three-dimensional P wave tomography. This zone has -3 to -4% of $V_P$ difference with respect to the reference velocity model and is inferred to contain little to no partial melt resolvable by this geophysical method (*Farrell et al.*, 2014; *Huang et al.*, 2015). Since magma injection is a discrete event with respect to the spatially and time averaged resolution of seismic tomography, we see no contradiction between the geodetic sources and lack of a clear $V_P$ anomaly. *Wicks et al.* (1998, 2006) have argued that two discrete sources of deformation exist below the caldera floor, and are episodically active over different times. However, both the uniform and distributed (Figure 4, Figure S6) opening models indicate that a single dislocation can explain most of the deformation signal during 2004-2009. The caldera source has no clear boundary between the magma accumulation zones below SCD and MLD, except for localized uplift at the SCD, resulting in an additional 5 cm of uplift with respect to MLD. Given the few cycles of deformation observed with detailed geodetic observations, it is not possible to assess if the discrete storage zones below the MLD and SCD (*Wicks et al.*, 2006, 1998) are representative of caldera uplift during longer periods of time. The NGB source is significantly shallower with respect to the source that uplifted during 1996-2000 located at a depth of 14 km (*Wicks et al.*, 2020), vs 10.7 during 2004-2009. However, *Wicks et al.* (2020) concluded that the same NGB source can model the 1996-2000, 2004-2009 but with different amounts of sill opening and closing. Another difference with respect to *Chang et al.* (2007) and *Chang et al.* (2010) models is that a significant part of the NGB source is located below the caldera floor, and not adjacent to it.

Changes in the source geometry can be assessed comparing the location and wavelength of the deformation signals for the different episodes of uplift for InSAR data that were acquired with the same or very similar flight direction, radar beam and look angle. These data sets include ERS-1/2 descending interferograms and a stack (Figure S4), the ENVISAT IM2 data (Figure 2) and the TSX descending stack. Here the ERS-1/2 and ENVISAT IM2 data have the same line-of-sight. This analysis shows that the wavelength and location of the deformation signals varies during the periods of caldera

subsidence in 1992-1995 (*Wicks et al.* (1998); *Aly and Cochran* (2011), Figure S4), uplift in 1996-1997 (Figure 2F in *Wicks et al.* (1998)), subsidence in 2000-2002 (Figures 2b-c in *Wicks et al.* (2006)), uplift in 2004-2009 (Figure 2), subsidence in 2010-2013 (Figure 2), uplift in 2014-2015 (*Wicks et al.* (2020), Figure 8) and subsidence in 2015-2020 (Figure 1 in *Wicks et al.* (2020)). The deformation signals at NGB also shows differences in location and wavelength during the episodes of unrest between in 1996-2008 (*Wicks et al.* (2020), Figure 2, Figure S4), uplift during early 2014, subsidence during the rest of 2014 and uplift during 2015-2019 (Fig 2b-c in *Wicks et al.* (2020)). This implies that the deformation sources are not stable during several cycles of uplift and subsidence, and they slightly change from one cycle to the next one. In contrast, other volcanoes show stable deformation sources over several cycles of deformation, even after eruptions (*Lu et al.*, 2010; *Lu and Dzurisin*, 2010; *Delgado*, 2020). The lack of stationary sources indicates patterns of migrating fluids towards shallower depths (*Wicks et al.*, 2020) and hampers the use of magma dynamics models that rely on a single stable source in depth and location to explain long cycles of unrest (e.g., *Giudicepietro et al.* (2017)). The spatial variability also indicates a highly dynamic plumbing system, akin to a crystal mush where unrest occurs episodically and in discrete zones of the mush (*Cashman et al.*, 2017). On the other hand, we can ask: does the deformation data indicate a trans-crustal magmatic system in which unrest occurs at multiple depth levels in the crust? The variability in the source depths suggests that this actually occurs at Yellowstone, even on short time scales of less than one year, like during the NGB uplift in early 2014 (Figure 1). However, the exact pattern of fluid migration, potential magma mixing and mingling and stress interaction (e.g., *Albino and Sigmundsson* (2014)) are yet to be unravelled.

### 6.2 Driving mechanisms of unrest

On a geological time scale, the driving mechanism of unrest at Yellowstone caldera is discrete pulses of basalt injection at the base of the rhyolitic plumbing system below the caldera and NGB. *Lowenstern and Hurwitz* (2008) calculated that $\sim$0.3 km$^3$/yr of basalt intrusion with 1 wt% of dissolved $CO_2$ is required to account for the measured flux of passive $CO_2$ degassing at Yellowstone, 4 times larger than the time-averaged rate of $\sim$0.07 km$^3$/yr during 2004-2009. A direct comparison between these data sets is not possible due to the episodic nature of magma injection and the lack of continuous time-lapse measurements of $CO_2$ degassing, discussed in detail later. The mechanisms of unrest are less clear over shorter time scales due to the coupling of the shallow hydrothermal system with the deeper magmatic system and volatile exsolution from the injecting basalt (*Dzurisin et al.*, 2012). Also, independent data sets and models suggest contradicting mechanisms. Yellowstone lake shorelines have tilted terraces such that the caldera subsidence slightly exceeds caldera uplift during the Holocene (*Pierce et al.*, 2002). To account for the slight subsidence, the volume change of exsolved volatiles extracted from the caldera must exceed the volume of injected magma, and these events must alternate in time. This leads *Pierce et al.* (2002) to suggest that the buildup and extraction of magmatic volatiles is a more likely explanation for the slightly higher subsidence in the Holocene than magma injection. Further, *Fournier* (1989) showed that a crystallizing magma can release 0.026 km$^3$/yr of exsolved fluids from the magma trapped below a self-sealed layer. This is enough to account for the volume changes that produced the caldera uplift during 1923-1975. The swarms are likely due to the episodic breaching of a self-sealed layer at the BDT that leads to fluid extraction from the caldera (*Waite and Smith*, 2002). This process is highly enhanced by a deepening of the BDT, produced by an increase in the strain rate due to episodic magma injection (*Fournier*, 2007), contradicting the previous mechanisms for unrest due to volatile pressurization and extraction.

Thereby, *Dzurisin et al.* (2012) favor a conceptual model that reconciles a wide range of geological, geochemical and geophysical observations. This model suggests

that episodic batches of basalt are injected at the base of the rhyolitic crystal mush resulting in reservoir pressurization either at NGB or SCD. As the basalt and the mush crystallize, magmatic volatiles are exsolved. These fluids are in a supercritical state that are trapped below a self-sealed layer in the lower parts of the hydrothermal system and the upper section of the magmatic system resulting in reservoir pressurization and caldera uplift. The self-sealed layer is also the BDT. Magma injection increases the strain rate, which temporarily deepens the BDT. In this scenario, fluids in the plastic zone at near lithostatic pressures eventually breach the self-sealed layer, leading to seismic swarms in distal parts of the caldera (*Waite and Smith*, 2002), fluid migration outside of the caldera and ground subsidence (*Fournier*, 1989, 2007). Long-term subsidence at the caldera is likely produced by volatile exsolution from the crystallizing rhyolitic mush that also migrates outside of the caldera (*Dzurisin et al.*, 1990). However, the *Dzurisin et al.* (2012) model does not allow for the assessment of the relative contributions of magma injection and volatile exsolution in the reservoir pressurization (e.g., *Tait et al.* (1989)) and the fluids sink sources. Therefore, we compare our results with the previous studies.

The LKWY, WLWY and OFW2 GPS fit to the magma injection model (Figure 7) is a strong indication that the driving mechanism of uplift for the caldera source is the injection of $\sim$0.354 km$^3$ of incompressible basalt during 2004-2009, with no need to argue for exsolved volatiles (discussed later). In this model the pressure of the deep magma source increased linearly until it reached a threshold in early 2005, then it remained constant. This results in a time-variable uplift rate that increased exponentially and then decreased exponentially after 2005, until the hydraulic connection with the deep mantle source was shut down by inelastic processes (discussed later). Magma is injected in the upper part of the mushy plumbing system inferred from seismic tomography (*Farrell et al.*, 2014; *Huang et al.*, 2015). This is also valid for the caldera uplift during 2014-2015, in which magma was also likely injected, with a source pressure function that was different to that of the 2004-2009 episode, and with an unclear connection between the caldera and NGB sources. On the other hand, there are significant differences. First, the NGB reservoir during 2014-2015 is significantly shallower at a depth of 1-4.5 km (*Wicks et al.*, 2020; *Dzurisin et al.*, 2019) vs 10.7 km for 2004-2009, leading *Wicks et al.* (2020) to suggest a source of hydrothermal origin. Therefore, we discard that the subsidence at NGB during 2014 would result from magma transfer from this source into the much deeper caldera source, located at a depth of $\sim$6 km during 2014 (*Wicks et al.*, 2020). Hence, the model of two connected reservoirs cannot be applied to this episode of uplift. We speculate that the reversal from uplift to subsidence at NGB in March 2014 resulted from fluid migration into the shallow hydrothermal system following the breaching of the self-sealed layer that separates the BDT. Since the caldera source did not change its behaviour when NGB uplifted in early 2014 (Figure 8), we speculate that the BDT breaching might have changed the stress field in the deeper source (e.g., *Albino and Sigmundsson* (2014)), potentially allowing for magma to be injected from a mantle source. The exact mechanism is beyond the scope of this study.

A significant caveat of the magma injection models is that they do not consider the complex structure of Yellowstone's underlying plumbing system inferred from local and teleseismic tomographies (*Farrell et al.*, 2014; *Huang et al.*, 2015). These studies show that the volcano is underlain by a low $V_p$ anomaly at depths of 5-17 km with 5-15% of melt fraction interpreted as a rhyolitic partial melt underlain by basaltic partial melt. Another low velocity zone is located at depths of 20 to 50 km, with a melt fraction of 2%, extending to the Moho and also interpreted as basaltic partial melt. The two low velocity zones are physically separated. The magma injection models considered in this study do not consider how magma bypasses or interacts in some way with these very large areas of partial melt, nor how the melt can segregate through the porous crystalline matrix to ascend through the crystal mush that likely

exists in the upper crust. Further, the magma injected during 2004-2009 likely has a basaltic chemical composition compared to that of the mushy rhyolitic reservoir, and they might eventually coalesce on time scales of $10^4$ - $10^4$ years (e.g., *Biggs and Annen* (2019)). Magma can also stall somewhere in the crust in a level of neutral buoyancy and undergo viscosity changes resulting in reservoir pressurization. Despite the data show that the deformation sources do not change during the episode of uplift, it is unclear how the ascending basalt interacts with the plumbing system in the framework of a transcrustal model of unrest on multiple levels in the crust (*Cashman et al.*, 2017; *Sparks et al.*, 2019; *Sparks and Cashman*, 2017). These are all points that have to be addressed in future studies that relax the restrictive assumptions made in the models of magma injection (Figure 9).

The spatial coincidence of the SCD with the area of maximum uplift has led other studies to suggest that this is the main area of magma injection (*Wicks et al.*, 2006; *Chang et al.*, 2007). Despite the fact that uplift started simultaneously for SCD and MLD in July 2004, we see no clear evidence in the OFW2, WLWY and LKWY stations (Figure 1, Figure S1) to state that magma was first intruded at SCD and then it migrated to MLD, or that magma was injected at MLD and then was stored at SCD. Whatever the situation, this suggests a highly connected area of magma storage that responded coevally to the onset of magma injection with no clear boundary as shown by the distributed sill opening models (Figure 5). GPS observations in the middle of the caldera floor might help to address this point during future episodes of unrest.

Magma ascent resulting in reservoir pressurization is due to both its overpressure and its buoyancy with respect to the host rock (Equation 6-Equation 7). The model of connected reservoirs provides insights in this aspect (Figure 10). First, the model with both magma buoyancy and magma overpressure is unable to reproduce the double exponential signals observed at the caldera floor and the NGB, indicating that the signal observed in the GPS time series is indicative of magma overpressure only. This is not a unique characteristic of Yellowstone and has been observed at other volcanoes (e.g., *Le Mével et al.* (2016)). Second, if buoyancy effects are neglected, then the NGB source inflates in response to the magma flux, resulting in a pressure function very similar to that of the caldera source, but this is not observed. Whatever the case, the model suggests that magma ascends solely due to its overpressure, and that the subsidence at NGB cannot be explained by a mechanism of magma flow with Newtonian viscosity extraction towards the caldera source.

Any mechanism that explains the subsidence at NGB must take into account the very similar onset of uplift with respect to the caldera source, and that the subsidence at NGB ends as the caldera uplift decreases. This implies that the subsidence is therefore triggered by magma injection at the caldera. The hydrothermal system is shallower than 5 km (*Fournier*, 1989), so the 2004-2009 NGB source is too deep to be considered of hydrothermal origin. *Chang et al.* (2007) explained the subsidence at NGB with a mechanism in which the caldera sill opening produces positive dilatation up to $3 \times 10^{-5}$ strain next to the crack tip. This value is one order of magnitude above the smallest measured strain change produced by dynamic earthquake triggering that can induce transient increases in the medium permeability (*Manga et al.*, 2012). This mechanism can induce flow of magmatic volatiles from NGB to the caldera and trigger microseismicity between these two sources. Although the mechanism is plausible, there is a caveat. The NGB sill is located below the BDT and the surrounding medium is plastic with little to no permeability that fluids can use to migrate between the sources. Therefore an opening sill should not produce an increase in the medium permeability because there is no primary porosity (*Fournier*, 2007). The permeability can be increased by magma injection which increases the strain rate, deepening the BDT by $\sim$1 km, resulting in a change in the rheological properties and bringing deep zones that are plastic into a brittle behavior for a short period of time. However, the

NGB and caldera sills lie at depths of 8.7 and 10.6 km (Figure S8), too deep to lie in the brittle region even after the transient increase in the strain rate. Further, lowering the BDT usually results in the breaching of the layer that separates the BDT, not in fractures in zones that are deep into the plastic zone. This implies that the permeability mechanism of magma transport is also not feasible and the connection between NGB and the caldera is uncertain.

We have shown that the geodetic signals during the episode of caldera uplift can be explained entirely by magma injection, with no need to invoke volatile exsolution. But this model is neither unique nor necessarily the best explanation. It does not imply that during other episodes of ground uplift magma injection or other mechanisms of unrest can also produce the exact same geodetic signal. For example, rhyolitic plumbing systems are crystal mushes (e.g., *Bachmann and Bergantz* (2008)) and Yellowstone's plumbing system has limited amounts of melt (*Farrell et al.*, 2014; *Huang et al.*, 2015). Here, exsolved fluids can percolate through the porous matrix and ascend to the top of the mush where they accumulate in sill-like discrete areas. As the volume of fluids increases this can also result in sill pressurization and ground deformation (*Sparks et al.*, 2019). Therefore, we can ask: is it possible that the fluid exsolution, permeable flow and fluid accumulation at the liquid-rich mush cap does not result in detectable pressurization during the caldera uplift? Is it possible that any significant fluid exsolution occurs only in response to the depressurization of the self-sealed layer after it is breached? This seems unlikely. For example, fluid exsolution is not enhanced if the minimum principal stress equals the lithostatic load until the latter equals the pore-fluid pressure (section 10.4.2 in *Fournier* (2007)), and this could be attained only after a certain amount of magma has been injected. Further, the mechanisms can vary significantly from an episode to the next one (*Fournier*, 2007), and mechanisms of unrest that last $10^0$ - $10^1$ years might not be representative of the overall caldera behaviour during time scales of $10^4$ - $10^5$ years (*Pierce et al.*, 2002). These scenarios were not considered in this study but are geologically plausible, so future studies should address them.

### 6.3 Comparison with seismicity, microgravity and stream/gas geochemistry

Ground deformation is one of the several indicators of volcano unrest but uncertainties in the mechanisms that result in ground uplift imply that these data should be analyzed and compared jointly with other independent data sets (*Pritchard et al.*, 2019). Here we compare the deformation during the episode of uplift with the dense seismic (*Waite and Smith*, 2002; *Farrell et al.*, 2014) and geochemical (*Lowenstern et al.*, 2017) data acquired during more than 30 years at Yellowstone.

Statistics of the number of earthquakes per quarter do not show any abnormal trends during 2004-2008 (Figure 1B in *Chang et al.* (2007), *Chang et al.* (2010), Figure 8 in *Shelly et al.* (2013), Figure 1 in *Farrell et al.* (2014)). The largest clusters of earthquakes with $M_L > 2.5$ in the caldera during the episode of uplift (Figure 1) occurred during 2004-2006 with microseismicity located at the northern edge of the caldera floor (*Chang et al.* (2007), not shown in Figure 1), and during the December 2008 swarm at Yellowstone Lake (*Farrell et al.*, 2010). The seismicity at the onset of uplift is scattered across the caldera with no clear clusters and significantly less than the seismicity triggered when the uplift transitions to subsidence (*Shelly et al.*, 2013). Focal mechanisms calculated from waveform first arrivals show normal faulting with seismicity clusters towards the N and S parts of the caldera and with only four events at the SCD (*Russo et al.*, 2017). *Taira et al.* (2010) analyzed five M3+ earthquakes during 2007-2009, and two of these events were the first non-double couple focal mechanisms since monitoring started in 1975. These earthquakes are triggered by fluid migration due to an increase in dilatation from the sill towards shallower opening

cracks. *Farrell et al.* (2009) calculated the b-value from the Gutenberg-Richter law in a de-swarmed earthquake catalog from 1973 to 2006, showing high b-values next to MLD, but no abnormal values indicative of fluid injection at the SCD. We conclude that the 2004-2009 caldera uplift was not related to abnormal seismicity in response to magma injection compared with the seismic swarms when deformation shifts from uplift to subsidence (*Waite and Smith*, 2002; *Shelly et al.*, 2013). This is in contrast with other volcanoes, like Long Valley caldera where the onset ground uplift is correlated with increases in seismicity (Fig 3a in *Hill et al.* (2020)). The lack of abnormal seismicity during 2004 is not unique to Yellowstone, as other volcanoes with very fast deformation, either basaltic like Sierra Negra (*Davidge et al.*, 2017), or rhyolitic like Cordón Caulle (*Delgado et al.*, 2018) are accompanied by limited amounts of seismicity. One potential explanation for the overall lack of abnormal seismicity is that the plastic rocks around the rhyolitic reservoir cannot be fractured except at the end of the cycles of uplift when the rocks behave in a brittle way for short periods of time. Another alternative is that the 2004-2009 cycle of uplift did not produce significant seismicity due to the Kaiser effect (*Heimisson et al.*, 2015). Here fracturing and seismicity are produced only if the medium is stressed above a threshold in a loading cycle that had already resulted in fracturing. However, this hypothesis can not be proved as either true or false because only two cycles of uplift in 1923-1984 and 1996-1997 before 2004 were recorded with instrumental observations, both with a significantly worse temporal sampling than the 2004-2009 cycle.

Micro-gravity data were only measured during 2007-2012 (*Farrell*, 2014), and then since 2017 (*Poland and Zeeuwvan Dalfsen*, 2019). The 2007-2012 data did not show clear gravity changes but as the data did not include high quality elevation measurements for each gravity station, it did not provide insights on any particular geological process (*Poland and Zeeuwvan Dalfsen*, 2019). Therefore the gravity data cannot be directly compared with the InSAR and GPS observations during 2004-2009. *Poland and Zeeuwvan Dalfsen* (2019) measured gravity variations four times during 2017 and concluded that the gravity uncertainty of ∼20 mGal on stable benchmarks is low enough to detect mass changes due to magma injection.

In terms of gas and fluid geochemistry, despite the many decades of sampling at Yellowstone's hydrothermal fields (e.g., *Lowenstern et al.* (2017)), there is a dearth of long-term geochemical time series. Continuous measurements of $CO_2$ with eddy covariance instruments have been underway only since 2016 (*Lewicki et al.*, 2017). High temporal resolution water chemistry measurements at the Upper Geyser Basin during 2007-2008 (*Hurwitz et al.*, 2012) and in major rivers during 2001-2004 and 2006-2007 (*Hurwitz et al.* (2007b), *Hurwitz et al.* (2010)) cannot be compared with the episode of caldera uplift due to their low temporal sampling, or being too distant from the areas of unrest. Decadal time-lapse measurements are only available for chloride discharges in streams with a yearly temporal sampling, but these measurements did not show any unambiguous trend that deviates from the base level values during the period of caldera uplift (*Hurwitz and Lowenstern*, 2014). Furthermore, a lateral redistribution of the abnormal chloride flux due to basalt injection would take years to decades until it would result in abnormal fluxes in streams and therefore correlations with ground deformation are not expected to be detected (*Hurwitz et al.*, 2007b). These authors also concluded that it would be more feasible to detect perturbations in the shallow hydrothermal system due to deep magma injection by tracking changes in the gas and steam flux instead of the river solute fluxes. Finally, the correlation between older episodes of unrest with geochemistry of springs in the NW part of the caldera do not provide meaningful insights (*Evans et al.*, 2006).

We conclude that the 2004-2009 episode of caldera uplift was not correlated with other large-scale signs of unrest except during the December 2008 dike intrusion

(*Farrell et al.*, 2010) and the transition from uplift to subsidence in January 2010 (*Shelly et al.*, 2013).

### 6.4 Eruptive potential of Yellowstone

Eruptions occur under tensile failure when the deviatoric stress in a pressurized reservoir reaches the tensile strength of the rock (∼10-40 MPa), and resulting in a mode I crack that propagates to the Earth surface (*Tait et al.*, 1989; *Pinel and Jaupart*, 2003; *Albino et al.*, 2010). Other studies show that shear failure occurs before tensile failure (*Gerbault*, 2012). We use the source pressure change as a proxy for the tensile strength of the encasing rock at Yellowstone's magma reservoir. The MBEM inversion predicts source overpressures of ∼0.08 MPa (Figure S9), several orders of magntiude below the tensile strength of the rock (∼10 MPa). Therefore individual pulses of uplift like those in 2004-2009 are very unlikely to lead to an eruption, unless the reservoir is very close to failure, for which there is no evidence. Eruptions should occur every ∼100 cycles of uplift similar to that of 2004-2009. The recurrence interval of large-scale caldera uplift and then pressurization is not well constrained since geodetic observations with yearly temporal resolution started in 1975. If pressurization cycles last on the order of ∼5 years, the eruption recurrence is at least 500 years, although there is considerable uncertainty because the caldera uplift is highly transient, with variable duration and length of the quiescence periods. If we assume that for every episode of uplift there is an episode of quiescence or caldera subsidence of similar duration, then the eruptive frequency increases to 1,000 years. The last eruptions at Yellowstone occurred ∼70 Kyrs ago (*Christiansen*, 2001), which is more than one order of magnitude longer than our eruption interval. If the net record of deformation in the Holocene is slight subsidence, it implies that reservoir deflation is slightly larger than reservoir pressurization and hence the pulses of uplift are even less likely to result in an eruption (*Pierce et al.*, 2002).

Despite the small amount of pressurization, which are much lower than pressure changes in smaller sills elsewhere (e.g., *Le Mével et al.* (2016); *Delgado et al.* (2016)), a seismic swarm interpreted as a small dike intrusion occurred in December 2008 - January 2009. The material that intruded the dike was either rhyolitic magma or magma-derived aqueous fluids (*Farrell et al.*, 2010). The dike is offset with respect to the locus of maximum magma injection at the SCD. This dike produced small displacements recorded by the LKWY station (< 1 cm, *Farrell et al.* (2010)), but the distributed opening model shows residuals in the eastern part of Yellowstone Lake that could be explained by this small dike (Figure 4). One explanation is that this intrusion was triggered by reaching the tensile strength of the rock after thousands of loading cycles. Another alternative is that successive cycles of uplift and subsidence at the caldera floor might have decreased and permanently fractured the surrounding rock due to damage loading, effectively lowering the wall rock shear modulus and decreasing the rupture threshold (*Carrier et al.*, 2015). If this is true, cyclic pressurization that is unable to trigger a dike intrusion under the aforementioned standard rupture models (*Pinel and Jaupart*, 2003; *Tait et al.*, 1989; *Albino et al.*, 2010) can result in small dike intrusions that would not be observed otherwise. Another alternative is that these rupture criteria are not valid for the geologic conditions of Yellowstone due to the very large plumbing system of this volcano and the weak surrounding crust. Another alternative is that it was not a dike intrusion but only a small swarm (*Shaul Hurwitz*, personal communication). A final alternative is that the swarm was produced by leakage of a small amount of magmatic fluids above the BDT, but with no resulting subsidence until the next leakage one year later. Whatever the case, the eruptive potential of Yellowstone deserves a more thorough analysis relating the cyclic loading model with a detailed analysis of the seismic data (e.g., *Carrier et al.* (2015)).

### 6.5 Transition of uplift to subsidence

One of the most intriguing features of Yellowstone is the cyclic transition of uplift to subsidence with periods of ∼10 years (Figure 1). This transition has been explained by the breaching of a self-sealed layer at the BDT due to transient pressurization by either magma injection or exsolved fluids which migrate outside the bounds of the caldera upon the layer breaching (*Waite and Smith*, 2002; *Dzurisin et al.*, 2012). The fluid migration occurs at the end of an uplift cycle and is coeval with seismic swarms in the distal parts of the caldera (*Waite and Smith*, 2002; *Shelly et al.*, 2013). Afterwards, the caldera subsides in response to migration of exsolved fluids from a crystallising mush for several years until another cycle resumes (*Dzurisin et al.*, 1990). Volumetric changes due to a cooling intrusion produce negligible volume changes and are unable to explain the caldera subsidence (*Dzurisin et al.*, 1990). In this model of cyclic deformation, the secular trend of subsidence due to volatile exsolution is reversed by highly transient pulses of basalt injection at the caldera, as in 2004-2009. The Madison Plateau swarm in January 2010 (*Shelly et al.* (2013), Figure 1) is interpreted as the breaching of the self-sealed layer in the NW part of the caldera, and occurred during the transition from uplift to subsidence. In general, non-eruptive subsidence at volcanoes and calderas like Cerro Blanco (*Pritchard and Simons*, 2004), Askja (*de Zeeuw-van Dalfsen et al.*, 2013) and Medicine Lake (*Poland et al.*, 2006) show linear rates of ∼2-3 cm/yr on time spans of decades. These have been related to cooling intrusions and a combination of other mechanisms like tectonic extension, but in the absence of a clear sink area, the exact mechanism of subsidence is quite uncertain.

The InSAR and GPS observations raise more questions than answers on the mechanisms of caldera subsidence. First, what is the sink of the magmatic fluids extracted from the NGB? *Wicks et al.* (2020) suggested that fluids extracted from NGB are injected either in the Norris-Mammoth corridor or the Hebgen Lake fault zone which are the zones with the highest amount of seismicity at Yellowstone. None of the post 2010 data show clear deformation signals outside of the caldera that could be sink sources for some fluids extracted from NGB and the caldera, although the small swath of the TSX data also introduces some uncertainty in this regard (Figure 2). It is also possible that the escaping fluids do not leave a clear geodetic signal if there is no sink reservoir to store them. This is in contrast with the post 2014 deformation which shows small-scale deformation that could reflect fluid pathways outside of the caldera (Fig 7 in *Wicks et al.* (2020)). Second, if the end of the caldera uplift is due to some inelastic mechanism of fluid migration above the BDT, then it implies that breaching the self-sealed layer changed the force balance on the conduit that feeds the caldera reservoir. Fluid migration outside of the caldera source implies that the pressure gradient driving this flow is much higher than the pressure gradient between the caldera and the mantle source, suggesting a feedback mechanism. We speculate that the breaching of the self-sealed layer stopped the connection between the deep mantle and the caldera sources as the magma injection model predicts several years of continuing uplift had the breaching not occurred (Figure 7). From a fluid mechanics point of view, this situation is analogous to reservoirs that were inflating prior to an eruption and erupt with reservoir deflation and without co-eruptive magma recharge (e.g., equation 7 in *Segall* (2013), equation S.29 in *Delgado et al.* (2019)). Finally, the pattern of cyclic uplift and subsidence (Figure 1) indicates that Yellowstone might behave as a harmonic oscillator with periods of ∼10 years (e.g., *Walwer et al.* (2019)), and this should also include the effect of viscoelastic relaxation on time scales of several decades. More geodetic data recording future episodes of unrest will shed light on this.

## 7 Conclusions

In this study we revisit InSAR and GPS time series that span the 2004-2009 episode of ground uplift at Yellowstone caldera, the largest instrumentally detected

at this volcano. For the first time, simple solid and fluid mechanics models derived from geophysical data provide quantitative evidence that the caldera uplift during this time period results from magma injection from a deep mantle source into a shallow source at ~8.7 km. Magma ascent and injection results only from its overpressure, not from the effects of buoyancy. In contrast, transient increases in permeability and/or magma extraction from the NGB source towards the caldera source cannot explain the subsidence that is recorded at the former area. The caldera uplift can be modeled with no need to invoke pressurization due to exsolved volatiles, which raises the question on the non-uniqueness of models that can explain the geodetic observations. In general, the episode of uplift was only related to small increases in the microseismicity in areas neighboring the caldera, with no clear correlation with other instrumental observations. A more complete view of episodes of unrest can result from a more integrated view of the different geochemical, geodetic and seismological data sets. Future studies should consider more complex mechanisms of volatile exsolution, stress-driven fluid migration and abrupt changes in the force balance that drives the fluid transport and storage between the caldera, the NGB source and potential sink regions.

**Acknowledgments**

F.D. acknowledges the French Centre National d'Etudes Spatiales (CNES) for a post-doctoral fellowship, Charles Wicks (U.S. Geological Survey) for discussions and granting access to TSX data, Valérie Cayol (Université Clermont Auvergne) for her help with the DEFVOLC boundary element software, Tara Shreve (Carnegie Institution for Science), Michael Poland, Jacob Lowenstern, Shaul Hurwitz (U.S. Geological Survey), Juliet Biggs (University of Bristol) for discussions, and Paula Burgi (Cornell University) for her grammar review. The InSAR data was processed at IPGP's S-CAPAD cluster and we thank Geneviève Moguilny for her help with this computing facility. We thank Editor Paul Tregoning and two anonynous reviewers for their comments that improved the quality of the manuscript. This is IPGP contribution XXXX.

## Data Availability statement

ERS-1/2 and ENVISAT data are property of the European Space Agency (ESA) and were provided through GEO Geohazard Supersites and Natural Laboratories and UNAVCO. ALOS-1 data are property of the Japanese Ministerium of Trade and Commerce and were provided by NASA through the Alaska Satellite Facility. TerraSAR-X data are property of Deutsche Zentrum fr Luft- und Raumfahrt (DLR) and are available at UNAVCO upon request to Principal Investigator Charles Wicks (USGS). GPS data were provided by Nevada Geodetic Laboratory and also available by the USGS Earthquake Hazard Program. Earthquakes in Figure 1 are from the USGS Earthquake Catalog.

# Tables

| Satellite | $\lambda$ (cm) | Dates (yyyy/mm/dd) | Pass | Path | $\theta$ | Mode, Beam | #SAR | #Ifg | Atmcor | DEMcor |
|---|---|---|---|---|---|---|---|---|---|---|
| ENVISAT | 5.56 | 2004/09/03 - 2010/09/17 | A | 48 | 19 | IM1 | 26 | 14 | no | no |
| ENVISAT | 5.56 | 2004/09/22 - 2009/10/21 | A | 320 | 23 | IM2 | 26 | 42 | ERAW2 | yes |
| ENVISAT | 5.56 | 2005/05/24 - 2010/08/31 | D | 313 | 19 | IM1 | 12 | 10 | ERAW2 | no |
| ENVISAT | 5.56 | 2005/05/05 - 2010/10/21 | D | 41 | 23 | IM2 | 28 | 37 | ERAW2 | yes |
| ALOS-1 | 23.8 | 2006/12/30 - 2011/02/25 | A | 197 | 38 | FBD-FBS | 15 | 7 | linear | no |
| ALOS-1 | 23.8 | 2007/01/16 - 2011/03/14 | A | 198 | 39 | FBD-FBS | 19 | N/A | N/A | N/A |
| TerraSAR-X | 3.1 | 2011/07/23 - 2013/07/07 | A | 45 | 21 | strip_003 | 12 | 2* | no | no |
| TerraSAR-X | 3.1 | 2011/07/28 - 2013/10/19 | A | 121 | 35 | strip_009 | 16 | 3* | no | no |
| TerraSAR-X | 3.1 | 2011/07/19 - 2013/10/10 | D | 159 | 28 | strip_006 | 10 | 6* | no | no |

Table 1: Details of the processed SAR data sets. The columns show the satellite name, radar wavelength ($\lambda$), date range (year/month/day), whether the satellite is in an ascending (A) or descending (D) orbit, satellite path, average incidence angle ($\theta$), radar beam except for ALOS-1 where it indicates the radar mode (either FBD or FBS, Fine Beam Double and Fine Beam Single polarization), number of synthetic aperture radar images (SAR) per track, and the number of interferograms used in the time series (Ifg). The asterisk indicates the number of stacked interferograms instead of the number pairs used in the time series inversion. Atmcor is the type of atmospheric correction applied to the data: ERAW2 atmospheric correction with the ERA5 model and an empirical correction with an elevation-dependent term on top of that. DEMcor refers to whether a DEM error correction (*Ducret et al.*, 2014) was used or not.

| **Source model** | **$X_s$ (km)** | **$Y_s$ (km)** | **$Z_s$ (km)** | **L (km)** | **W (km)** | $\theta$ | $\delta$ |
|---|---|---|---|---|---|---|---|
| Sill caldera floor | 537.0** | 4933.2** | 8.7 ** | 57.6** | 18.6** | 54* | 0* |
| Sill NGB | 528.1** | 4940.0** | 10.6 ** | 22.6 | 26.6 | 357 | 0* |

Table 2: Best-fit sill models. $X_s$ centroid EW coordinate, $Y_s$ centroid NS coordinate, $Z_s$ centroid depth, a major semi axis, b semi-minor axis. Centroid coordinates are in WGS84 UTM 12N datum. Model parameters were iteratively inverted for. First we fixed parameters with * since they converge much faster than any of the others in the NA inversion. After many iterations we fixed the parameters with **. Finally we inverted the rest of the NGB model parameters .

| G (GPa) | $\nu$ | H (km) | $H_2$ (km) | $a_s$ (km) | $a_d$ (km) | $\gamma$ | $\Delta\rho$ (kg/m$^3$) | $V_{R_s}$ (km$^3$) | $V_{R_d}$ (km$^3$) | $\beta_m$ (Pa$^{-1}$) |
|---|---|---|---|---|---|---|---|---|---|---|
| 2.1 | 0.25 | 10 | 2 | 15 | 10 | $\frac{8(1-\nu)}{3\pi}$ | 270 | 1000 | 100 | 0-1$\times10^{-10}$ |

Table 3: Parameters for the analytic model of magma injection connecting two reservoirs. G from *Heap et al.* (2020), $H_2$ and $H$ from the best-fit sill inversion (Table 2), $\gamma$ for the crack-like sill reservoirs.

973 **Figures**

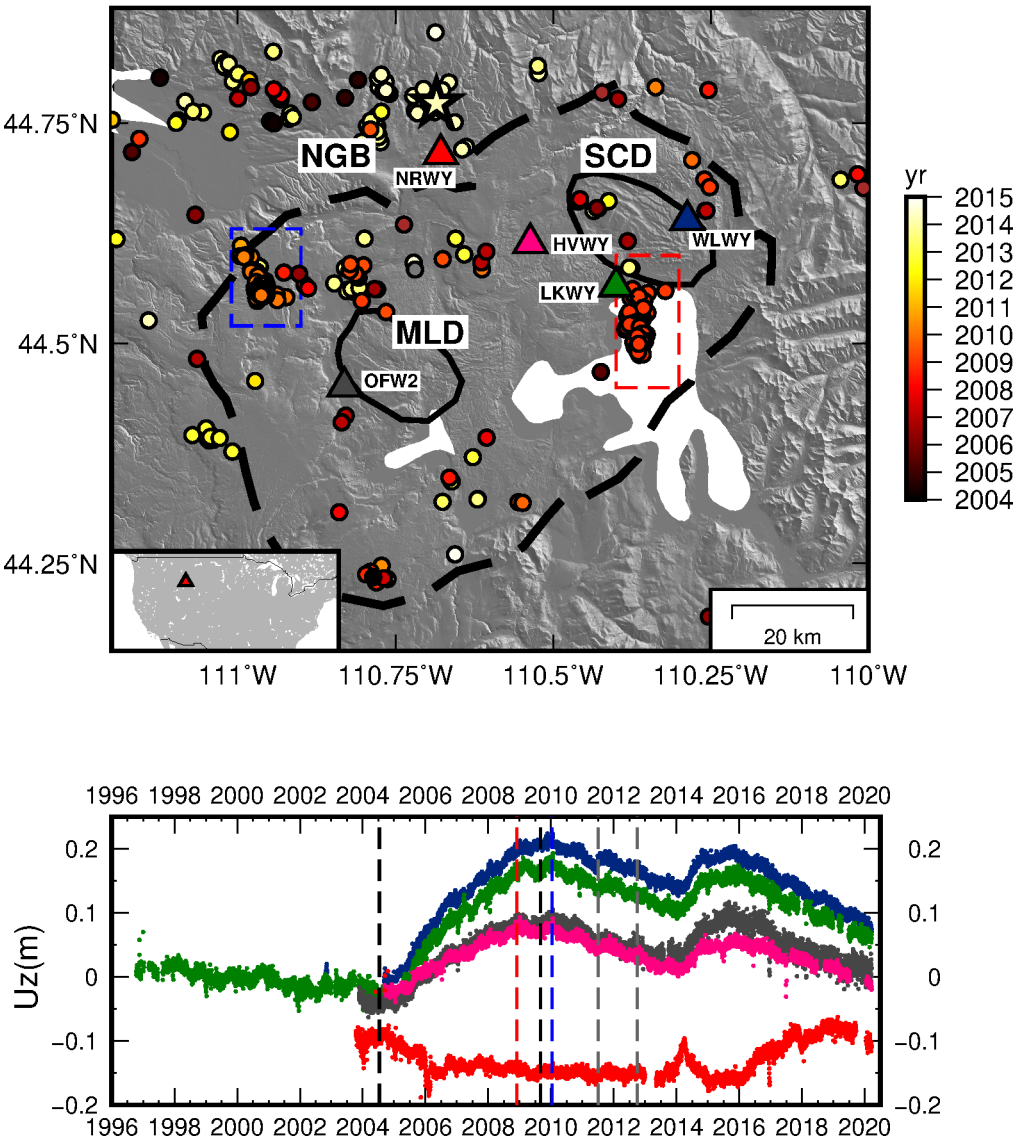


Figure 1: Top. Yellowstone caldera (thick dashed line), Mallard Lake (MLD) and Sour Creek (SCD) resurgent domes (black lines) draped over the 10m shaded NED DEM. Triangles are GPS stations that recorded data during the complete episode of unrest in 2004-2009. The dots show earthquakes from the USGS Earthquake Catalog shallower than 15 km with $M_L > 2.5$. The red and blue dashed rectangles show the December 2008 (*Farrell et al.*, 2010) and January 2010 Madison Plateau (*Shelly et al.*, 2013) seismic swarms. The star is the $M_W$ 4.8 earthquake of March 30 2014 at NGB. Inset shows location of Yellowstone caldera (red triangle) within the United States. Bottom. GPS time series of vertical deformation (colored triangles on top). The dashed black and grey lines show the 2004-2009 episode of unrest, and the caldera subsidence covered by the TSX data during 2011-2012 respectively. The vertical red and blue lines show the December 2008 and January 2010 seismic swarms.

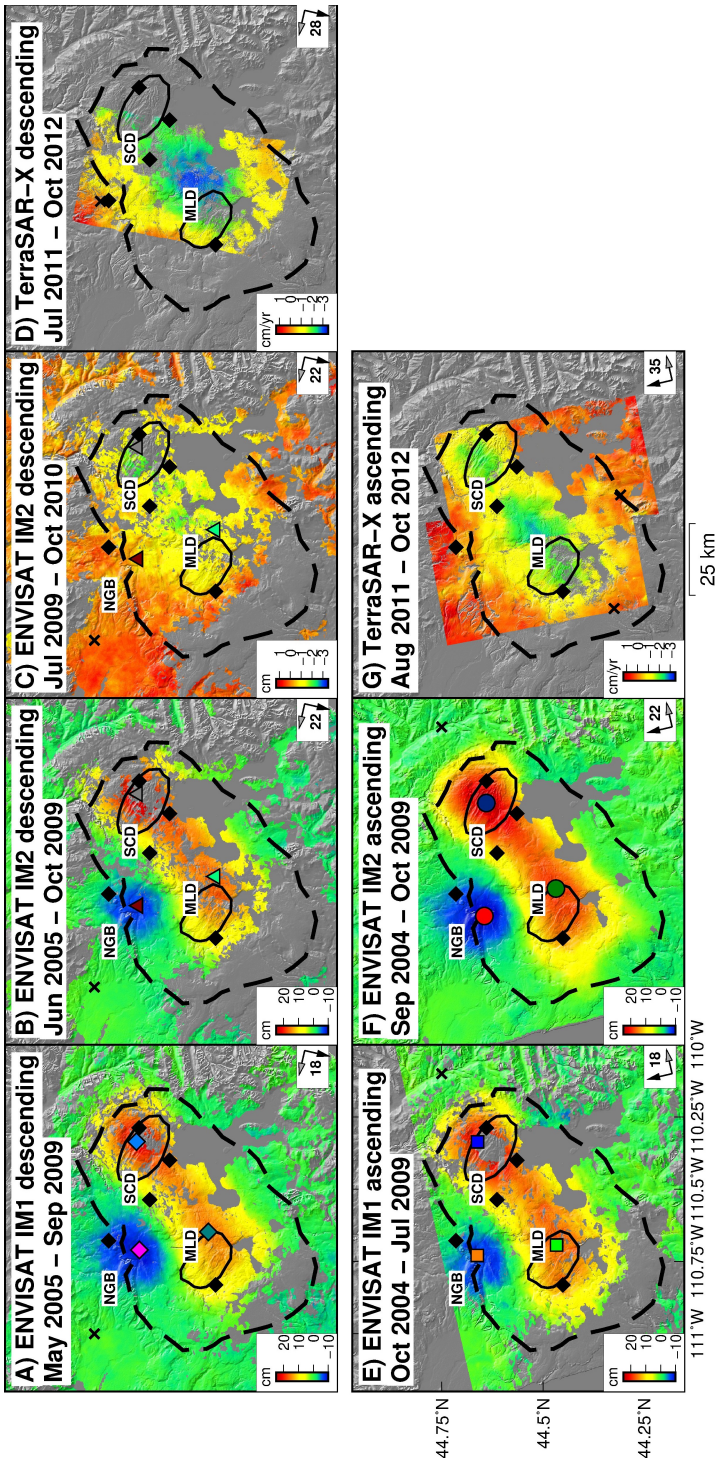


Figure 2: ENVISAT interferograms that record the total displacement at Yellowstone during 2004-2009 from InSAR time series (A, B, C, E, F, units in cm), and mean ground velocities from TSX stacks (D, G, units in cm/yr). The dashed black line is the caldera border and the thin black lines show the MLD) and (SCD). NGB is the Norris Geyser basin. The black diamonds are the continuous GPS stations used in the study (Figure 1). The black crosses are the reference point for each time series. The colored circles, squares, triangles and diamonds in (A, B, C, E, F) show the location of maximum uplift for MLD and SCD, and subsidence for NGB in the time series in Figure 2.

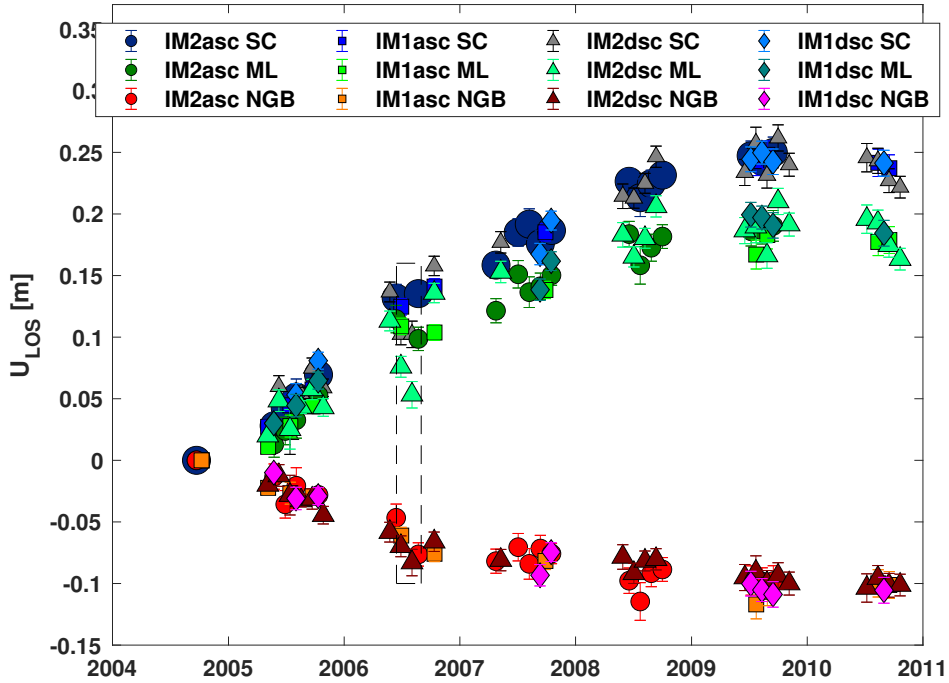


Figure 3: ENVISAT time series for selected pixels of maximum displacement at SCD, MLD and NGB (Figure 2). The IM2dsc data show larger dispersion in the displacement because the interferograms used in the time series contain far more turbulent signals than any of the other three tracks (Supplementary Material). The dashed box shows jumps in the IM2 descending time series not observed in other data sets. Using pairwise logic, these are not indicative of any ground deformation signal.

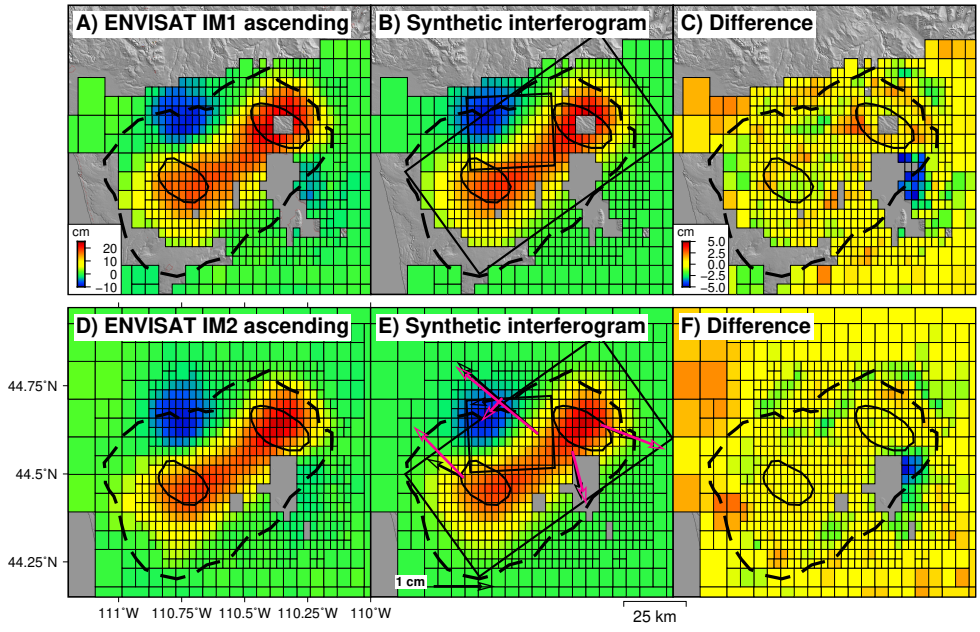


Figure 4: Downsampled (A, D), synthetic (B, E) and residual interferograms (C,F) produced by an opening sill below the caldera and by a closing sill below NG spanning 2004-2009. The black and pink arrows are the GPS data and synthetic data from the best-fit joint inversion. The rectangles are the modeled sills (Figure 5).

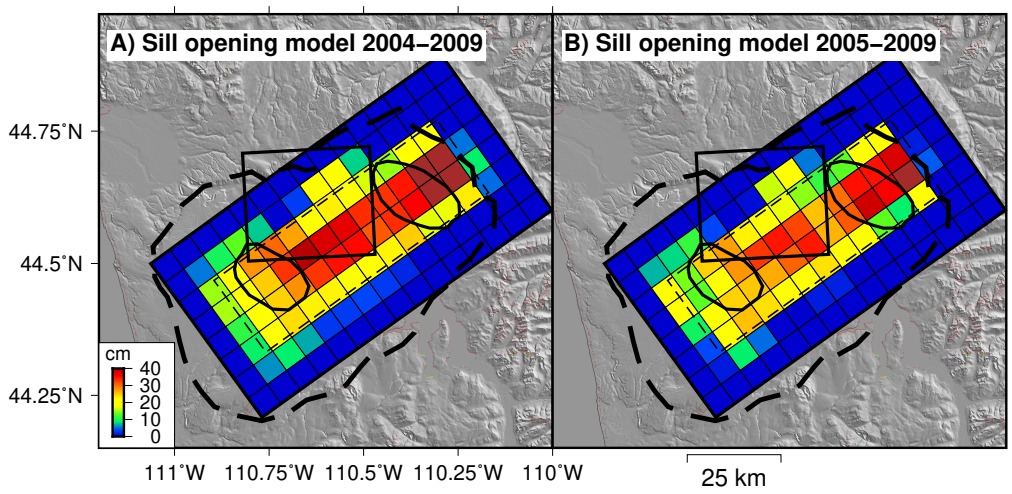


Figure 5: Distributed sill opening models for 2004-2009 (A) and 2005-2009 (B). The thin and dashed rectangles are the NGB and the caldera sources with uniform opening. The thick dashed line is the caldera border and the elliptical polygons are the SCD and MLD.

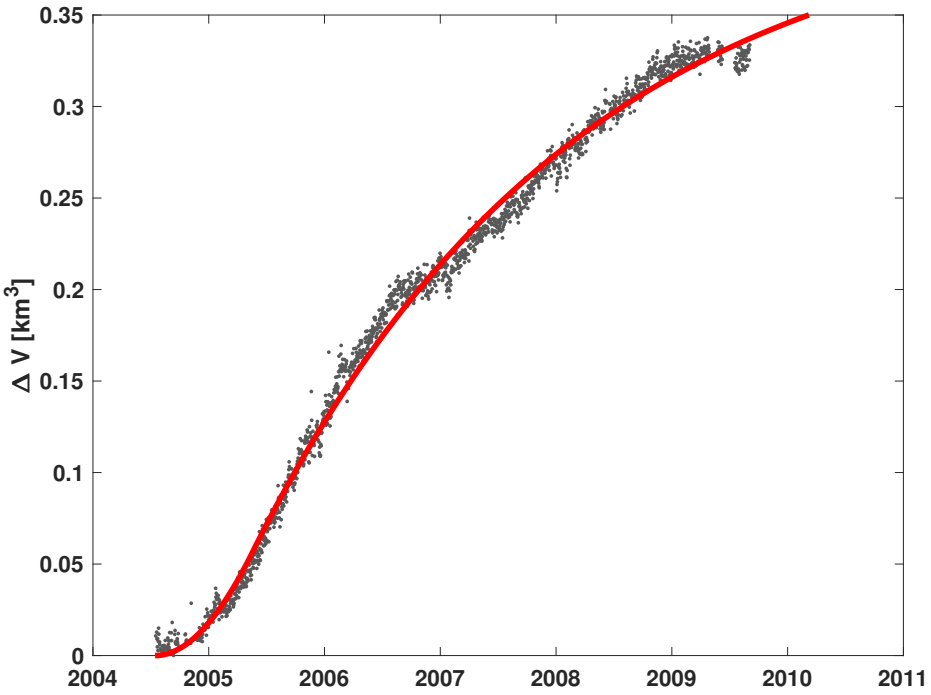


Figure 6: Time series of volume change ($\Delta V$) for the caldera floor source with uniform opening, and inverted from the vertical component ($U_z$) of all the GPS stations. The red line is the best-fit Equation 1, but with P scaled to represent the source volume change.

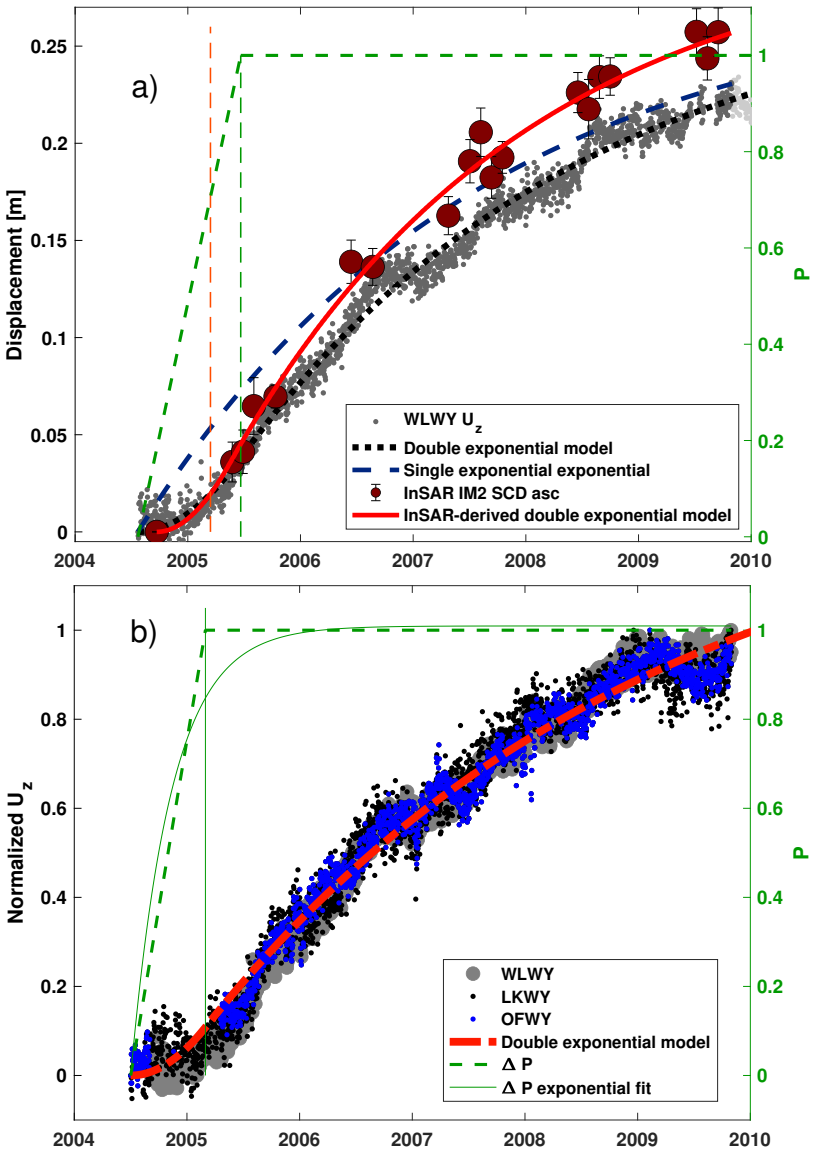


Figure 7: A. Magma injection model fits to GPS (grey dots) and InSAR (red circles) data. Displacement refers to either vertical displacement for GPS data or line-of-sight displacement for InSAR data. The red and black lines are the best-fit models to the InSAR IM2 for SCD and the vertical component of the WLWY station. The blue dashed line is the best-fit function $U = U_f(1 - e^{-t/\tau})$ with $U_f$ the maximum displacement and $\tau$ a time constant. The right axis shows the pressure $P$ in the deep magma source. The vertical lines show the change in the deep magma pressure $P$ between a linearly increasing pressure to a constant pressure and (green line for GPS and orange line for InSAR). B. Best-fit magma injection model (red line) to the normalized vertical displacements of the WLWY, LKWY and OFW2 stations. The dashed green line is the adimensional mantle pressure function ($P_s$), and the green continuous line is the best-fit exponential fit of the form $P_s = P(1 - e^{-t/\tau_m})$. The latter function is used to simulate the magma flow between the caldera and NGB (Figure 10 - Figure 11). The vertical green lines in panels A and B do not agree with each other because in panel A the model is applied only to a single GPS station while in B it is applied to the normalized displacements of the three stations.

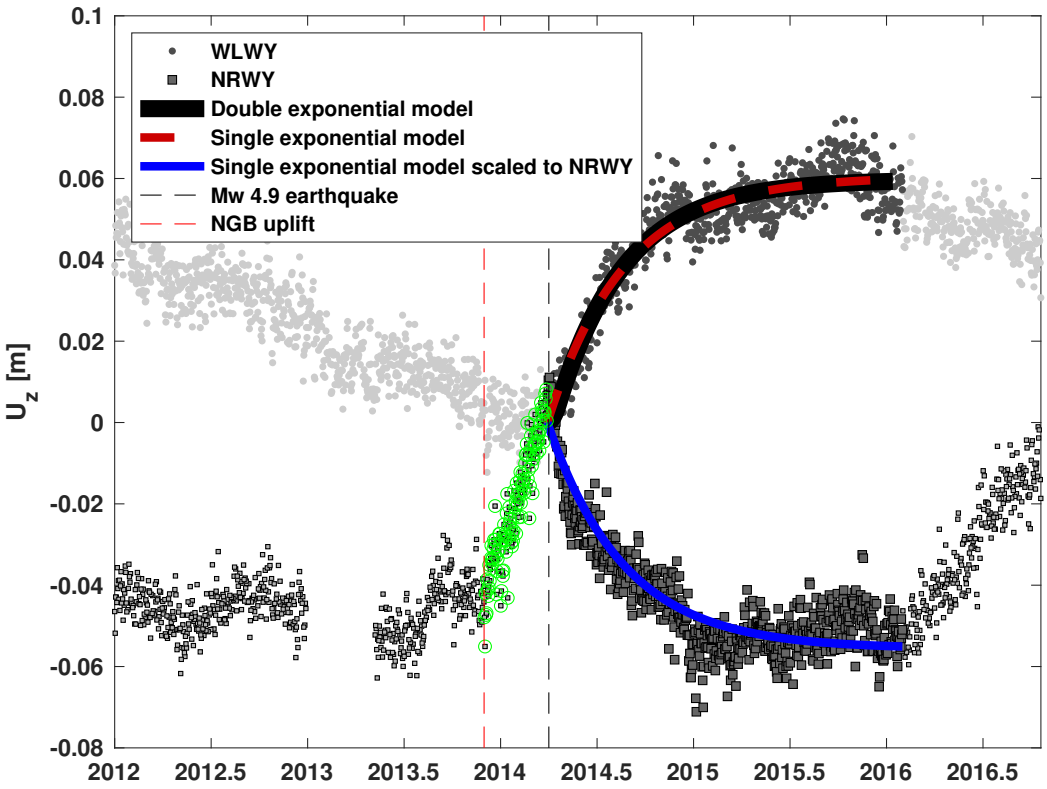


Figure 8: Time series of vertical displacement at stations WLWY and NRWY during 2014-2015, with best-fit models of magma injection for a double exponential (solid black line) and exponential fits of the form $U = U_f(1 - e^{-\frac{t}{\tau}})$ (dashed red line). The green dots show the NGB uplift during December 2013 - March 2014. The blue line is a scaled version of the exponential fit but applied to the NRWY vertical component during the same time span. The dashed vertical line shows the transition from uplift to subsidence at NGB coincident with a Mw 4.9 earthquake on March 30 2014. The model fit to the time series indicates two things. First, that the GPS data is indicative of magma injection at the caldera sill. Second, the NGB subsidence was coeval and with nearly the same time history as that of the caldera source. This coincidence was not observed during 2004-2009 (Figure 7).

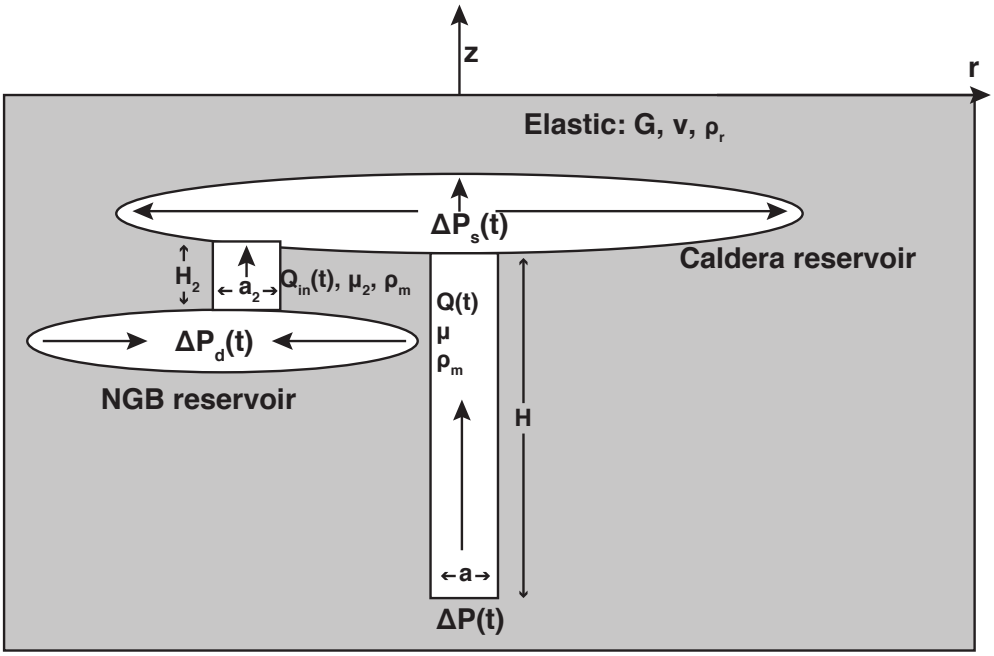


Figure 9: Sketch that shows the main physical parameters involved in the dynamic model of magma injection (Figure 10, Equation 11). The model is made up of two reservoirs that are penny-shaped cracks, but vertically exaggerated in the figure. Here $P_s$ and $P_d$ represent the pressure in the caldera floor and NGB reservoirs which are hydraulically connected. Magma ascends from a mantle source to the caldera source, which is also filled by magma flowing from the NGB source. The model does not consider large areas of partial melt inferred from $V_P$ tomography (*Farrell et al.*, 2014; *Huang et al.*, 2015) and how the melt can either bypass or interact with these areas.

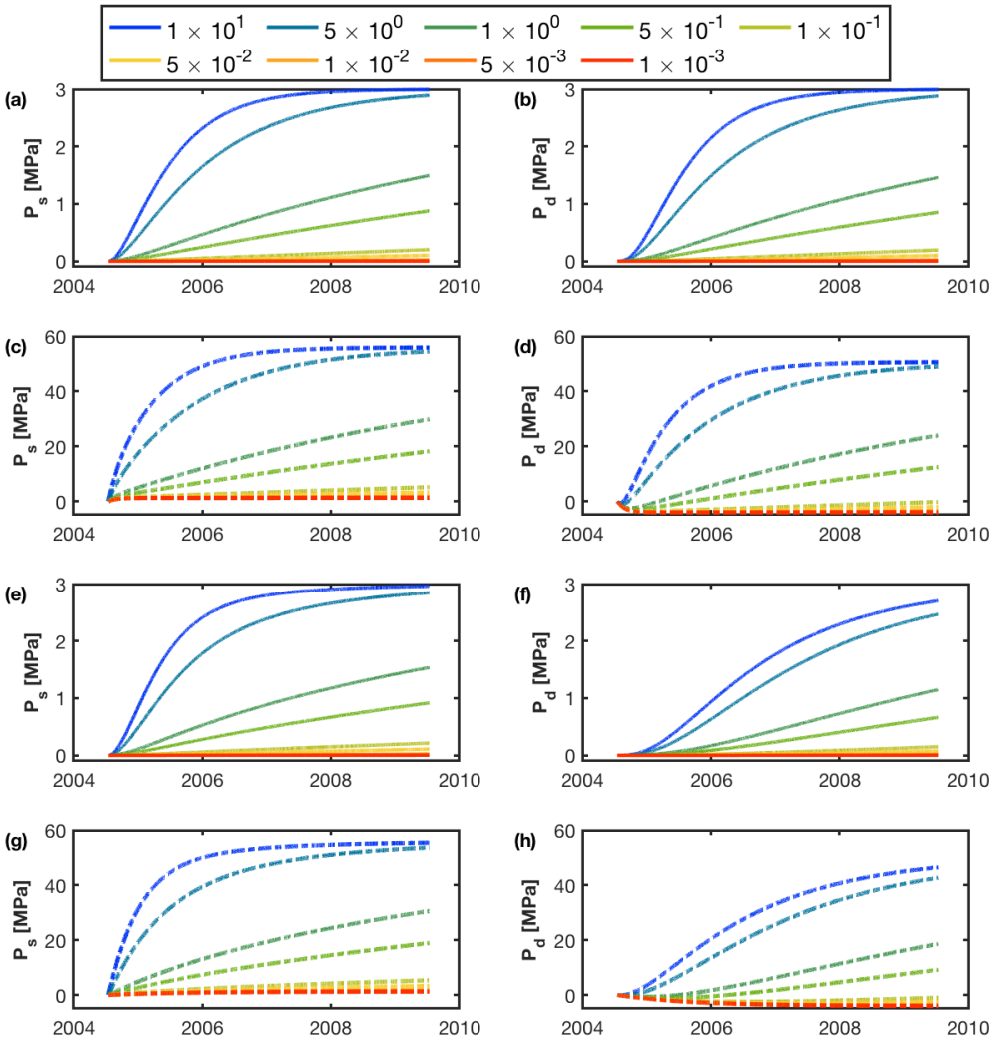


Figure 10: Simulation of the pressure change in the caldera source ($P_s$, a,c,e,g) and NGB ($P_d$, b,d,f,h) reservoirs based on the analytic model of magma transfer between the caldera floor and NGB (Equation 11) for the 2004-2009 time period. Panels a-b) show simulations with conduit flow due to magma overpressure while panels c-d) show models with flow due to both magma overpressure and buoyancy. The colored lines show simulations for different conduit conductivities between the caldera sources and a deep mantle source. a-d) and e-h) show simulations for conduit conductivities of 1 and 0.1 between the caldera sill and the deeper NGB sill. Deformation due to magma injection is proportional to the source pressure change in a linear elastic half-space, so the ground deformation follows functions with the same shape as the source pressure function. The models show that magma extraction from NGB to the caldera floor cannot explain both the deformation trends observed in the GPS (Figure 1) and InSAR (Figure 3) data.

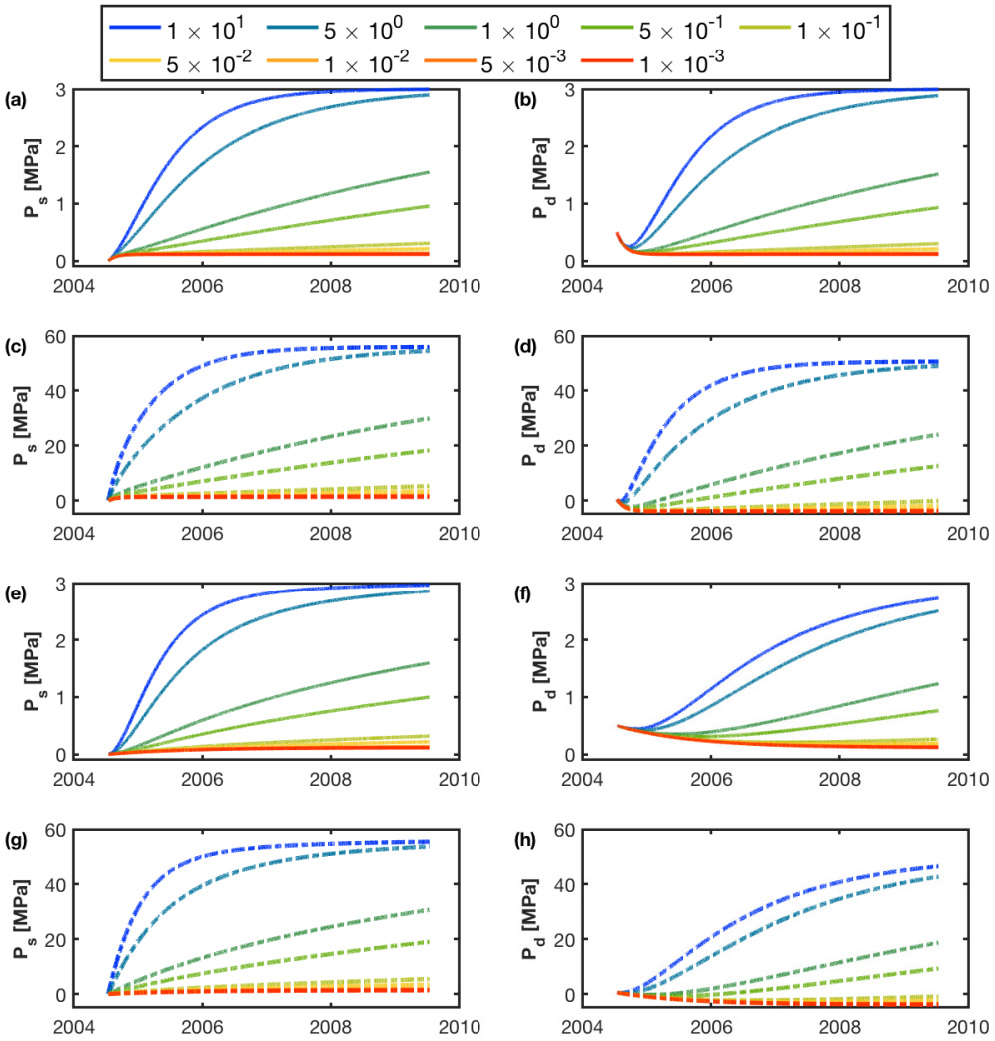


Figure 11: Same as Figure 10 but with $P_{d0} = 0.5$ MPa for the NGB sill. This simulation shows that magma extraction from NGB to the caldera can produce subsidence at NGB with a similar amplitude to that of the caldera uplift only if the NGB sill overpressure is unrealistically higher than the overpressure at the caldera sill.

## References


Acocella, V. (2019), Bridging the gap from caldera unrest to resurgence, *Frontiers in Earth Science*, 10.3389/feart.2019.00173.

Albino, F., and F. Sigmundsson (2014), Stress transfer between magma bodies: Influence of intrusions prior to 2010 eruptions at Eyjafjallajokull volcano, Iceland, *Journal of Geophysical Research-Solid Earth*, *119*(4), 2964–2975, 10.1002/2013jb010510.

Albino, F., V. Pinel, and F. Sigmundsson (2010), Influence of surface load variations on eruption likelihood: application to two Icelandic subglacial volcanoes, Grimsvotn and Katla, *Geophysical Journal International*, *181*(3), 1510–1524, 10.1111/j.1365-246X.2010.04603.x.

Aly, M. H., and E. S. Cochran (2011), Spatio-temporal evolution of Yellowstone deformation between 1992 and 2009 from InSAR and GPS observations, *Bulletin of Volcanology*, 10.1007/s00445-011-0483-y.

Amoruso, A., and L. Crescentini (2009), Shape and volume change of pressurized ellipsoidal cavities from deformation and seismic data, *Journal of Geophysical Research-Solid Earth*, *114*, 10.1029/2008jb005946.

Anderson, K., and P. Segall (2013), Bayesian inversion of data from effusive volcanic eruptions using physics-based models: Application to Mount St. Helens 2004-2008, *Journal of Geophysical Research-Solid Earth*, *118*(5), 2017–2037, 10.1002/jgrb.50169.

Annen, C. (2009), From plutons to magma chambers: Thermal constraints on the accumulation of eruptible silicic magma in the upper crust, *Earth and Planetary Science Letters*, *284*(3-4), 409–416, 10.1016/j.epsl.2009.05.006.

Annen, C., J. D. Blundy, J. Leuthold, and R. S. J. Sparks (2015), Construction and evolution of igneous bodies: Towards an integrated perspective of crustal magmatism, *Lithos*, *230*, 206–221, 10.1016/J.LITHOS.2015.05.008.

Aster, R. C., B. Borchers, and C. H. Thurber (2018), *Parameter estimation and inverse problems*, Elsevier, 10.1016/C2015-0-02458-3.

Bachmann, O., and G. Bergantz (2008), The magma reservoirs that feed supereruptions, *Elements*, *4*(1), 17–21, 10.2113/gselements.4.1.17.

Bachmann, O., and C. Huber (2016), Silicic magma reservoirs in the Earth's crust, *American Mineralogist*, *101*(11), 2377–2404, 10.2138/am-2016-5675.

Bagnardi, M., F. Amelung, and M. P. Poland (2013), A new model for the growth of basaltic shields based on deformation of Fernandina volcano, Galápagos Islands, *Earth and Planetary Science Letters*, 10.1016/j.epsl.2013.07.016.

Berardino, P., G. Fornaro, R. Lanari, and E. Sansosti (2002), A new algorithm for surface deformation monitoring based on small baseline differential SAR interferograms, *Ieee Transactions on Geoscience and Remote Sensing*, *40*(11), 2375–2383, 10.1109/tgrs.2002.803792.

Biggs, J., and C. Annen (2019), The lateral growth and coalesence of magma systems, *Philosophical Transactions of the Royal Society A: Mathematical, Physical and Engineering Sciences*, *377*(2139), 20180,005, 10.1098/rsta.2018.0005.

Blewitt, G., W. Hammond, and C. Kreemer (2018), Harnessing the GPS Data Explosion for Interdisciplinary Science, *Eos*, 10.1029/2018eo104623.

Carrier, A., J. L. Got, A. Peltier, V. Ferrazzini, T. Staudacher, P. Kowalski, and P. Boissier (2015), A damage model for volcanic edifices: Implications for edifice strength, magma pressure, and eruptive processes, *Journal of Geophysical Research: Solid Earth*, 10.1002/2014JB011485.

Cashman, K. V., R. S. J. Sparks, and J. D. Blundy (2017), Vertically extensive and unstable magmatic systems: A unified view of igneous processes, *Science*, 10.1126/science.aag3055.

Cayol, V., and F. H. Cornet (1997), 3D mixed boundary elements for elastostatic deformation field analysis, *International journal of rock mechanics and mining sciences & geomechanics abstracts*, 10.1016/S0148-9062(96)00035-6.

Chang, W.-L., R. B. Smith, C. Wicks, J. M. Farrell, and C. M. Puskas (2007), Accelerated uplift and magmatic intrusion of the Yellowstone caldera, 2004 to 2006, *Science*, *318*(5852), 952–956, 10.1126/science.1146842.

Chang, W.-L., R. B. Smith, J. Farrell, and C. M. Puskas (2010), An extraordinary episode of Yellowstone caldera uplift, 2004-2010, from GPS and InSAR observations, *Geophysical Research Letters*, *37*, 10.1029/2010gl045451.

Chen, C. W., and H. A. Zebker (2001), Two-dimensional phase unwrapping with use of statistical models for cost functions in nonlinear optimization, *Journal of the Optical Society of America a-Optics Image Science and Vision*, *18*(2), 338–351, 10.1364/josaa.18.000338.

Christiansen, R. L. (2001), The Quaternary and Pliocene Yellowstone Plateau volcanic field of Wyoming, Idaho, and Montana, *US Geological Survey Professional Paper*, 10.3133/pp729G.

Cooper, K. M. (2017), What Does a Magma Reservoir Look Like? The "Crystal's-Eye" View, *Elements*, *13*(1), 23–28, 10.2113/gselements.13.1.23.

Cooper, K. M., and A. J. Kent (2014), Rapid remobilization of magmatic crystals kept in cold storage, *Nature*, 10.1038/nature12991.

D'Auria, L., S. Pepe, R. Castaldo, F. Giudicepietro, G. Macedonio, P. Ricciolino, P. Tizzani, F. Casu, R. Lanari, M. Manzo, M. Martini, E. Sansosti, and I. Zinno (2015), Magma injection beneath the urban area of Naples: A new mechanism for the 2012-2013 volcanic unrest at Campi Flegrei caldera, *Scientific Reports*, 10.1038/srep13100.

Davidge, L., C. Ebinger, M. Ruiz, G. Tepp, F. Amelung, D. Geist, D. Coté, and J. Anzieta (2017), Seismicity patterns during a period of inflation at Sierra Negra volcano, Galápagos Ocean Island Chain, *Earth and Planetary Science Letters*, 10.1016/j.epsl.2016.12.021.

de Zeeuw-van Dalfsen, E., H. Rymer, E. Sturkell, R. Pedersen, A. Hooper, F. Sigmundsson, and B. Ófeigsson (2013), Geodetic data shed light on ongoing caldera subsidence at Askja, Iceland, *Bulletin of Volcanology*, 10.1007/s00445-013-0709-2.

Degruyter, W., and C. Huber (2014), A model for eruption frequency of upper crustal silicic magma chambers, *Earth and Planetary Science Letters*, *403*, 117–130, 10.1016/j.epsl.2014.06.047.

Delgado, F. (2020), Rhyolitic volcano dynamics in the Southern Andes: Contributions from 17 years of InSAR observations at Cordón Caulle from 2003 to 2020, *Journal of South American Earth Sciences*, 10.1016/j.jsames.2020.102841.

Delgado, F., M. E. Pritchard, D. Basualto, J. Lazo, L. Cordova, and L. E. Lara (2016), Rapid reinflation following the 2011-2012 rhyodacite eruption at Cordon Caulle volcano (Southern Andes) imaged by InSAR: Evidence for magma reservoir refill, *Geophysical Research Letters*, *43*(18), 9552–9562, 10.1002/2016gl070066.

Delgado, F., M. Pritchard, S. Samsonov, and L. Córdova (2018), Renewed post-eruptive uplift following the 2011-2012 rhyolitic eruption of Cordón Caulle (Southern Andes, Chile): evidence for transient episodes of magma reservoir recharge during 2012-2018, *Journal of Geophysical Research: Solid Earth*, 10.1029/2018JB016240.

Delgado, F., J. Kubanek, K. Anderson, P. Lundgren, and M. Pritchard (2019), Physicochemical models of effusive rhyolitic eruptions constrained with InSAR and DEM data: A case study of the 2011-2012 Cordón Caulle eruption, *Earth and Planetary Science Letters*, *524*, 115,736, 10.1016/J.EPSL.2019.115736.

Doin, M. P., C. Lasserre, G. Peltzer, O. Cavalie, and C. Doubre (2009), Corrections of stratified tropospheric delays in SAR interferometry: Validation with global atmospheric models, *Journal of Applied Geophysics*, *69*(1), 35–50,

10.1016/j.jappgeo.2009.03.010.

Doin, M.-P., F. Lodge, S. Guillaso, R. Jolivet, C. Lasserre, G. Ducret, R. Grandin, E. Pathier, and V. Pinel (2011), Presentation of the small baseline NSBAS processing chain on a case example: the Etna deformation monitoring from 2003 to 2010 using Envisat data, in *Proceedings of the ESA Fringe Workshop*.

Druitt, T. H., D. M. Pyle, and T. A. Mather (2019), Santorini volcano and its plumbing system, *Elements*, 10.2138/gselements.15.3.177.

Ducret, G., M.-P. Doin, R. Grandin, C. Lasserre, and S. Guillaso (2014), DEM Corrections Before Unwrapping in a Small Baseline Strategy for InSAR Time Series Analysis, *Ieee Geoscience and Remote Sensing Letters*, *11*(3), 696–700, 10.1109/lgrs.2013.2276040.

Dvorak, J. J., and G. Berrino (1991), Recent ground movenet and seismic activity in Campi Flegrei, southern Italy: episodic growth of a resurgent dome, *Journal of Geophysical Research-Solid Earth and Planets*, *96*(B2), 2309–2323, 10.1029/90jb02225.

Dzurisin, D., and Z. Lu (2007), Interferometric synthetic-aperture radar (InSAR), in *Volcano Deformation*, edited by D. Dzurisin, chap. 5, pp. 153–194, Springer, Berlin, Heidelberg, 10.1007/978-3-540-49302-0_5.

Dzurisin, D., J. C. Savage, and R. O. Fournier (1990), Recent crustal subsidence at Yellowstone Caldera, Wyoming, *Bulletin of Volcanology*, 10.1007/BF00304098.

Dzurisin, D., C. Wicks, and W. Thatcher (1999), Renewed uplift at the Yellowstone caldera measured by leveling surveys and satellite radar interferometry, *Bulletin of Volcanology*, 10.1007/s004450050277.

Dzurisin, D., C. W. Wicks, and M. P. Poland (2012), History of surface displacements at the Yellowstone Caldera, Wyoming, from leveling surveys and InSAR observations, 19232008, *U.S. Geological Survey Professional Paper*, *1788*, 68 p.

Dzurisin, D., Z. Lu, M. P. Poland, and C. W. Wicks (2019), Space-Based Imaging Radar Studies of U.S. Volcanoes, *Frontiers in Earth Science*, *6*, 249, 10.3389/feart.2018.00249.

Evans, W. C., D. Bergfeld, M. C. van Soest, M. A. Huebner, J. Fitzpatrick, and K. M. Revesz (2006), Geochemistry of low-temperature springs northwest of Yellowstone caldera: Seeking the link between seismicity, deformation, and fluid flow, *Journal of Volcanology and Geothermal Research*, 10.1016/j.jvolgeores.2006.01.001.

Farrell, J. (2014), Seismicity and tomographic imaging of the Yellowstone crustal magmatic-tectonic system, Ph.D. thesis, University of Utah.

Farrell, J., S. Husen, and R. B. Smith (2009), Earthquake swarm and b-value characterization of the Yellowstone volcano-tectonic system, *Journal of Volcanology and Geothermal Research*, 10.1016/j.jvolgeores.2009.08.008.

Farrell, J., R. B. Smith, T. Taira, W.-L. Chang, and C. M. Puskas (2010), Dynamics and rapid migration of the energetic 2008-2009 Yellowstone Lake earthquake swarm, *Geophysical Research Letters*, *37*(19), n/a–n/a, 10.1029/2010GL044605.

Farrell, J., R. B. Smith, S. Husen, and T. Diehl (2014), Tomography from 26years of seismicity revealing that the spatial extent of the Yellowstone crustal magma reservoir extends well beyond the Yellowstone caldera, *Geophysical Research Letters*, 10.1002/2014GL059588.

Feigl, K. L., H. Le Mével, S. T. Ali, L. Cordova, N. L. Andersen, C. DeMets, and B. S. Singer (2014), Rapid uplift in Laguna del Maule volcanic field of the Andean Southern Volcanic zone (Chile) 2007-2012, *Geophysical Journal International*, *196*(2), 885–901, 10.1093/gji/ggt438.

Fialko, Y. (2004a), Evidence of fluid-filled upper crust from observations of postseismic deformation due to the 1992 Mw7.3 Landers earthquake, *Journal of Geophysical Research: Solid Earth*, 10.1029/2004JB002985.

Fialko, Y. (2004b), Probing the mechanical properties of seismically active crust with space geodesy: Study of the coseismic deformation due to the 1992

1134 M <sub> w </sub> 7.3 Landers (southern California)
1135 earthquake, *Journal of Geophysical Research*, *109*(B3), B03,307, 10.1029/
1136 2003JB002756.
1137 Fialko, Y., M. Simons, and Y. Khazan (2001a), Finite source modelling of magmatic
1138 unrest in Socorro, New Mexico, and Long Valley, California, *Geophysical Journal*
1139 *International*, 10.1046/j.1365-246X.2001.00453.x.
1140 Fialko, Y., Y. Khazan, and M. Simons (2001b), Deformation due to a pressur-
1141 ized horizontal circular crack in an elastic half-space, with applications to vol-
1142 cano geodesy, *Geophysical Journal International*, *146*(1), 181–190, 10.1046/
1143 j.1365-246X.2001.00452.x.
1144 Fournier, R. O. (1989), Geochemistry and dynamics of the Yellowstone National
1145 Park hydrothermal system, *Annual review of earth and planetary sciences. Vol.*
1146 *17*, 10.1146/annurev.earth.17.1.13.
1147 Fournier, R. O. (2007), Hydrothermal systems and volcano geochemistry, in *Vol-*
1148 *cano Deformation*, edited by D. Dzurisin, chap. 10, pp. 323–341, Springer, Berlin,
1149 Heidelberg, 10.1007/978-3-540-49302-0_10.
1150 Fukushima, Y., V. Cayol, P. Durand, and D. Massonnet (2010), Evolution of magma
1151 conduits during the 1998-2000 eruptions of Piton de la Fournaise volcano, Reunion
1152 Island, *Journal of Geophysical Research-Solid Earth*, *115*, 10.1029/2009jb007023.
1153 Gerbault, M. (2012), Pressure conditions for shear and tensile failure around a cir-
1154 cular magma chamber; insight from elasto-plastic modelling, *Geological Society,*
1155 *London, Special Publications*, *367*, 111-130, 10.1144/SP367.8.
1156 Giordano, D., and D. B. Dingwell (2003), Non-Arrhenian multicomponent melt vis-
1157 cosity: A model, *Earth and Planetary Science Letters*, 10.1016/S0012-821X(03)
1158 00042-6.
1159 Giudicepietro, F., G. Macedonio, and M. Martini (2017), A Physical Model of Sill
1160 Expansion to Explain the Dynamics of Unrest at Calderas with Application to
1161 Campi Flegrei, *Frontiers in Earth Science*, *5*(54), 10.3389/feart.2017.00054.
1162 Goldstein, R. M., H. A. Zebker, and C. L. Werner (1988), Satellite radar inter-
1163 ferometry - two-dimensional phase unwrapping, *Radio Science*, *23*(4), 713–720,
1164 10.1029/RS023i004p00713.
1165 Heap, M. J., M. Villeneuve, F. Albino, J. I. Farquharson, E. Brothelande,
1166 F. Amelung, J. L. Got, and P. Baud (2020), Towards more realistic values of
1167 elastic moduli for volcano modelling, *Journal of Volcanology and Geothermal*
1168 *Research*, 10.1016/j.jvolgeores.2019.106684.
1169 Heimisson, E. R., P. Einarsson, F. Sigmundsson, and B. Brandsdottir (2015),
1170 Kilometer-scale Kaiser effect identified in Krafla volcano, Iceland, *Geophysical*
1171 *Research Letters*, *42*(19), 7958–7965, 10.1002/2015gl065680.
1172 Henderson, S. T., F. Delgado, J. Elliott, M. E. Pritchard, and P. R. Lund-
1173 gren (2017), Decelerating uplift at Lazufre volcanic center, Central Andes,
1174 from A.D. 2010 to 2016, and implications for geodetic models, *Geosphere*,
1175 10.1130/GES01441.1.
1176 Hildreth, W. (2017), Fluid-driven uplift at Long Valley Caldera, California: Geo-
1177 logic perspectives, *Journal of Volcanology and Geothermal Research*, *341*, 269–286,
1178 10.1016/j.jvolgeores.2017.06.010.
1179 Hill, D., E. Montgomery-Brown, D. R. Shelly, A. Flinders, and S. Prejean (2020),
1180 Post-1978 Tumescence at Long Valley Caldera, California: a Geophysical Perspec-
1181 tive, *Journal of Volcanology and Geothermal Research*, 10.1016/j.jvolgeores.2020
1182 .106900.
1183 Huang, H. H., F. C. Lin, B. Schmandt, J. Farrell, R. B. Smith, and V. C. Tsai
1184 (2015), The Yellowstone magmatic system from the mantle plume to the upper
1185 crust, *Science*, 10.1126/science.aaa5648.
1186 Huber, C., O. Bachmann, and J. Dufek (2010), The limitations of melting on the
1187 reactivation of silicic mushes, *Journal of Volcanology and Geothermal Research*,

1188 10.1016/j.jvolgeores.2010.06.006.
1189 Huber, C., O. Bachmann, and J. Dufek (2011), Thermo-mechanical reactivation of
1190 locked crystal mushes: Melting-induced internal fracturing and assimilation pro-
1191 cesses in magmas, *Earth and Planetary Science Letters*, 10.1016/j.epsl.2011.02.022.
1192 Huber, C., O. Bachmann, and J. Dufek (2012), Crystal-poor versus crystal-
1193 rich ignimbrites: A competition between stirring and reactivation, *Geology*,
1194 10.1130/G32425.1.
1195 Hutnak, M., S. Hurwitz, S. E. Ingebritsen, and P.A. Hsieh (2009), Numerical models
1196 of caldera deformation: Effects of multiphase and multicomponent hydrothermal
1197 fluid flow, *Journal of Geophysical Research*, *114*(B04411), 10.1029/2008JB006151.
1198 Hurwitz, S., and J. B. Lowenstern (2014), Dynamics of the Yellowstone hydrother-
1199 mal system, *Reviews of Geophysics*, *52*(3), 375–411, 10.1002/2014rg000452.
1200 Hurwitz, S., and M. Manga (2017), The Fascinating and Complex Dynam-
1201 ics of Geyser Eruptions, *Annual Review of Earth and Planetary Sciences*,
1202 10.1146/annurev-earth-063016-015605.
1203 Hurwitz, S., L. B. Christiansen, and P. A. Hsieh (2007a), Hydrothermal fluid flow
1204 and deformation in large calderas: Inferences from numerical simulations, *Journal*
1205 *of Geophysical Research-Solid Earth*, *112*(B2), 10.1029/2006jb004689.
1206 Hurwitz, S., J. B. Lowenstern, and H. Heasler (2007b), Spatial and temporal geo-
1207 chemical trends in the hydrothermal system of Yellowstone National Park: Infer-
1208 ences from river solute fluxes, *Journal of Volcanology and Geothermal Research*,
1209 10.1016/j.jvolgeores.2007.01.003.
1210 Hurwitz, S., W. C. Evans, and J. B. Lowenstern (2010), River solute fluxes reflect-
1211 ing active hydrothermal chemical weathering of the Yellowstone Plateau Volcanic
1212 Field, USA, *Chemical Geology*, 10.1016/j.chemgeo.2010.07.001.
1213 Hurwitz, S., A. G. Hunt, and W. C. Evans (2012), Temporal variations of geyser
1214 water chemistry in the Upper Geyser Basin, Yellowstone National Park, USA,
1215 *Geochemistry, Geophysics, Geosystems*, 10.1029/2012GC004388.
1216 Jaupart, C., and S. Tait (1990), Dynamics of eruptive phenomena, *Reviews in Min-*
1217 *eralogy*, *24*, 213–238.
1218 Jay, J., F. Costa, M. Pritchard, L. Lara, B. Singer, and J. Herrin (2014), Locating
1219 magma reservoirs using InSAR and petrology before and during the 2011-2012
1220 Cordon Caulle silicic eruption, *Earth and Planetary Science Letters*, *403*, 463,
1221 10.1016/j.epsl.2014.07.021.
1222 Jellinek, A. M., and D. J. DePaolo (2003), A model for the origin of large silicic
1223 magma chambers: precursors of caldera-forming eruptions, *Bulletin of Volcanol-*
1224 *ogy*, *65*(5), 363–381, 10.1007/s00445-003-0277-y.
1225 Jolivet, R., R. Grandin, C. Lasserre, M. P. Doin, and G. Peltzer (2011), Systematic
1226 InSAR tropospheric phase delay corrections from global meteorological reanalysis
1227 data, *Geophysical Research Letters*, *38*, 10.1029/2011gl048757.
1228 Jolivet, R., P. S. Agram, N. Y. Lin, M. Simons, M.-P. Doin, G. Peltzer, and Z. H. Li
1229 (2014), Improving InSAR geodesy using Global Atmospheric Models, *Journal of*
1230 *Geophysical Research-Solid Earth*, *119*(3), 2324–2341, 10.1002/2013jb010588.
1231 Le Mével, H., K. L. Feigl, L. Córdova, C. DeMets, and P. Lundgren (2015), Evolu-
1232 tion of unrest at Laguna del Maule volcanic field (Chile) from InSAR and GPS
1233 measurements, 2003 to 2014, *Geophysical Research Letters*, *42*(16), 6590–6598,
1234 10.1002/2015GL064665.
1235 Le Mével, H., P. Gregg, and K. L. Feigl (2016), Magma injection into a long-lived
1236 reservoir to explain geodetically measured uplift: application to the 20072014
1237 unrest episode at Laguna del Maule volcanic field, Chile, *Journal of Geophysical*
1238 *Research: Solid Earth*, pp. n/a–n/a, 10.1002/2016JB013066.
1239 Lengline, O., D. Marsan, J. L. Got, V. Pinel, V. Ferrazzini, and P. G. Okubo
1240 (2008), Seismicity and deformation induced by magma accumulation at three
1241 basaltic volcanoes, *Journal of Geophysical Research-Solid Earth*, *113*(B12), 12,

10.1029/2008jb005937.

Lewicki, J. L., P. J. Kelly, D. Bergfeld, R. G. Vaughan, and J. B. Lowenstern (2017), Monitoring gas and heat emissions at Norris Geyser Basin, Yellowstone National Park, USA based on a combined eddy covariance and Multi-GAS approach, *Journal of Volcanology and Geothermal Research*, 10.1016/j.jvolgeores.2017.10.001.

Liu, Z., D. Dong, and P. Lundgren (2011), Constraints on time-dependent volcanic source models at Long Valley Caldera from 1996 to 2009 using InSAR and geodetic measurements, *Geophysical Journal International*, *187*(3), 1283–1300, 10.1111/j.1365-246X.2011.05214.x.

Lohman, R. B., and M. Simons (2005), Some thoughts on the use of InSAR data to constrain models of surface deformation: Noise structure and data downsampling, *Geochemistry Geophysics Geosystems*, *6*, 12, 10.1029/2004gc000841.

Lowenstern, J. B., and S. Hurwitz (2008), Monitoring a supervolcano in repose: Heat and volatile flux at the yellostone caldera, *Elements*, 10.2113/GSELEMENTS.4.1.35.

Lowenstern, J. B., D. Bergfeld, W. C. Evans, and A. G. Hunt (2015), Origins of geothermal gases at Yellowstone, 10.1016/j.jvolgeores.2015.06.010.

Lowenstern, J. B., T. W. Sisson, and S. Hurwitz (2017), Probing magma reservoirs to improve volcano forecasts, *EOS*, *98*, doi.org/10.1029/2017EO085189.

Lu, Z., and D. Dzurisin (2010), Ground surface deformation patterns, magma supply, and magma storage at Okmok volcano, Alaska, from InSAR analysis: 2. Coeruptive deflation, July-August 2008, *Journal of Geophysical Research-Solid Earth*, *115*, 10.1029/2009jb006970.

Lu, Z., T. Masterlark, D. Dzurisin, R. Rykhus, and C. Wicks (2003), Magma supply dynamics at Westdahl volcano, Alaska, modeled from satellite radar interferometry, *Journal of Geophysical Research-Solid Earth*, *108*(B7), 10.1029/2002jb002311.

Lu, Z., D. Dzurisin, J. Biggs, C. Wicks, and S. McNutt (2010), Ground surface deformation patterns, magma supply, and magma storage at Okmok volcano, Alaska, from InSAR analysis: 1. Intereruption deformation, 1997-2008, *Journal of Geophysical Research-Solid Earth*, *115*, 10.1029/2009jb006969.

Lundgren, P., S. Usai, E. Sansosti, R. Lanari, M. Tesauro, G. Fornaro, and P. Berardino (2001), Modeling surface deformation observed with synthetic aperture radar interferometry at Campi Flegrei caldera, *Journal of Geophysical Research: Solid Earth*, *106*(B9), 19,355–19,366, 10.1029/2001JB000194.

Manga, M., I. Beresnev, E. E. Brodsky, J. E. Elkhoury, D. Elsworth, S. E. Ingebritsen, D. C. Mays, and C. Y. Wang (2012), Changes in permeability caused by transient stresses: Field observations, experiments, and mechanisms, *Reviews of Geophysics*, 10.1029/2011RG000382.

McTigue, D. F. (1987), Elastic stress and deformation near a finite spherical magma body: Resolution of the point source paradox, *Journal of Geophysical Research: Solid Earth*, *92*(B12), 12,931–12,940, 10.1029/JB092iB12p12931.

Miller, C. A., H. Le Mevel, G. Currenti, G. Williams-Jones, and B. Tikoff (2017), Microgravity changes at the Laguna del Maule volcanic field: Magma-induced stress changes facilitate mass addition, *Journal of Geophysical Research-Solid Earth*, *122*(4), 3179–3196, 10.1002/2017jb014048.

Miller, C. F., and D. A. Wark (2008), Supervolcanoes and their explosive supereruptions, *Elements*, *4*(1), 11–15, 10.2113/gselements.4.1.11.

Montgomery-Brown, E. K., C. W. Wicks, P. F. Cervelli, J. O. Langbein, J. L. Svarc, D. R. Shelly, D. P. Hill, and M. Lisowski (2015), Renewed inflation of Long Valley Caldera, California (2011 to 2014), *Geophysical Research Letters*, *42*(13), 5250–5257, 10.1002/2015gl064338.

Newman, A. V., T.H. Dixon, and N. Gourmelen (2006), A four-dimensional viscoelastic deformation model for Long Valley Caldera, California, between 1995 and 2000, *Journal of Volcanology and Geothermal Research*, *150*(1-3), 244–269,

10.1016/j.jvolgeores.2005.07.017

Novoa, C., D. Remy, M. Gerbault, J.C. Baez, A. Tassara, L. Cordova, C. Cardona, M. Granger, S. Bonvalot, and F. Delgado (2019), Viscoelastic relaxation: A mechanism to explain the decennial large surface displacements at the Laguna del Maule silicic volcanic complex, *Earth and Planetary Science Letters*, *521*, 49–59, 10.1016/j.epsl.2019.06.005.

Okada, Y. (1985), Surface deformation due to shear and tensile faullts in a half-space, *Bulletin of the Seismological Society of America*, *75*(4), 1135–1154.

Parks, M. M., J. Biggs, P. England, T. A. Mather, P. Nomikou, K. Palamartchouk, X. Papanikolaou, D. Paradissis, B. E. Parsons, D. M. Pyle, C. Raptakis, and V. Zacharis (2012), Evolution of Santorini Volcano dominated by episodic and rapid fluxes of melt from depth, *Nature Geoscience*, *5*(10), 749–754, 10.1038/ngeo1562.

Pascal, K., J. Neuberg, and E. Rivalta (2014), On precisely modelling surface deformation due to interacting magma chambers and dykes, *Geophysical Journal International*, *196*(1), 253–278, 10.1093/gji/ggt343.

Pedersen, R., and F. Sigmundsson (2006), Temporal development of the 1999 intrusive episode in the Eyjafjallajokull volcano, Iceland, derived from InSAR images, *Bulletin of Volcanology*, *68*(4), 377–393, 10.1007/s00445-005-0020-y.

Pelton, J. R., and R. B. Smith (1979), Recent crustal uplift in Yellowstone National Park, *Science*, 10.1126/science.206.4423.1179.

Pierce, K. L., K. P. Cannon, G. A. Meyer, M. J. Trebesch, and R. D. Watts (2002), Post-Glacial Inflation-Deflation Cycles, Tilting, and Faulting in the Yellowstone Caldera Based on Yellowstone Lake Shorelines Open-File Report 02-0142, *US Geological Survey Professional Paper*.

Pinel, V., and C. Jaupart (2003), Magma chamber behavior beneath a volcanic edifice, *Journal of Geophysical Research-Solid Earth*, *108*(B2), 10.1029/2002jb001751.

Pinel, V., C. Jaupart, and F. Albino (2010), On the relationship between cycles of eruptive activity and growth of a volcanic edifice, *Journal of Volcanology and Geothermal Research*, *194*(4), 150–164, 10.1016/j.jvolgeores.2010.05.006.

Poland, M., R. Bürgmann, D. Dzurisin, M. Lisowski, T. Masterlark, S. Owen, and J. Fink (2006), Constraints on the mechanism of long-term, steady subsidence at Medicine Lake volcano, northern California, from GPS, leveling, and InSAR, *Journal of Volcanology and Geothermal Research*, 10.1016/j.jvolgeores.2005.07.007.

Poland, M. P., and E. Zeeuwvan Dalfsen (2019), Assessing Seasonal Changes in Microgravity at Yellowstone Caldera, *Journal of Geophysical Research: Solid Earth*, p. 2018JB017061, 10.1029/2018JB017061.

Pritchard, M. E., and M. Simons (2004), An InSAR-based survey of volcanic deformation in the southern Andes, *Geophysical Research Letters*, *31*(15), 4, 10.1029/2004gl020545.

Pritchard, M. E., T. A. Mather, S. R. McNutt, F. J. Delgado, and K. Reath (2019), Thoughts on the criteria to determine the origin of volcanic unrest as magmatic or non-magmatic, *Philosophical Transactions of the Royal Society A: Mathematical, Physical and Engineering Sciences*, *377*(2139), 20180,008, 10.1098/rsta.2018.0008.

Puskas, C. M., R. B. Smith, C. M. Meertens, and W. L. Chang (2007), Crustal deformation of the Yellowstone-Snake River Plain volcano-tectonic system: Campaign and continuous GPS observations, 1987-2004, *Journal of Geophysical Research: Solid Earth*, 10.1029/2006JB004325.

Reverso, T., J. Vandemeulebrouck, F. Jouanne, V. Pinel, T. Villemin, E. Sturkell, and P. Bascou (2014), A two-magma chamber model as a source of deformation at Grimsvotn Volcano, Iceland, *Journal of Geophysical Research-Solid Earth*, *119*(6), 4666–4683, 10.1002/2013jb010569.

Rivalta, E. (2010), Evidence that coupling to magma chambers controls the volume history and velocity of laterally propagating intrusions, *Journal of Geophysical*

*Research: Solid Earth*, 10.1029/2009JB006922.

Rosen, P. A., S. Hensley, G. Peltzer, and M. Simons (2004), Updated repeat orbit interferometry package released, *Eos, Transactions American Geophysical Union*, *85*(5), 47, 10.1029/2004EO050004.

Rubin, A. E., K. M. Cooper, C. B. Till, A. J. Kent, F. Costa, M. Bose, D. Gravley, C. Deering, and J. Cole (2017), Rapid cooling and cold storage in a silicic magma reservoir recorded in individual crystals, *Science*, 10.1126/science.aam8720.

Russo, E., G. Waite, and A. Tibaldi (2017), Evaluation of the evolving stress field of the Yellowstone volcanic plateau, 1988 to 2010, from earthquake first-motion inversions, *Tectonophysics*, *700-701*, 80–91, 10.1016/J.TECTO.2017.02.009.

Sambridge, M. (1999), Geophysical inversion with a neighbourhood algorithm - I. Searching a parameter space, *Geophysical Journal International*, *138*(2), 479–494, 10.1046/j.1365-246X.1999.00876.x.

Schmandt, B., C. Jiang, and J. Farrell (2019), Seismic perspectives from the western U.S. on magma reservoirs underlying large silicic calderas, 10.1016/j.jvolgeores.2019.07.015.

Segall, P. (2013), Volcano deformation and eruption forecasting, *Remote Sensing of Volcanoes and Volcanic Processes: Integrating Observation and Modelling*, *380*, 85–106, 10.1144/sp380.4.

Segall, P. (2019), Magma chambers: What we can, and cannot, learn from volcano geodesy, 10.1098/rsta.2018.0158.

Shelly, D. R., D. P. Hill, F. Massin, J. Farrell, R. B. Smith, and T. Taira (2013), A fluid-driven earthquake swarm on the margin of the Yellowstone caldera, *Journal of Geophysical Research E: Planets*, 10.1002/jgrb.50362.

Sigmundsson, F., S. Hreinsdottir, A. Hooper, T. Arnadottir, R. Pedersen, M. J. Roberts, N. Oskarsson, A. Auriac, J. Decriem, P. Einarsson, H. Geirsson, M. Hensch, B. G. Ofeigsson, E. Sturkell, H. Sveinbjornsson, and K. L. Feigl (2010), Intrusion triggering of the 2010 Eyjafjallajokull explosive eruption, *Nature*, *468*(7322), 426–U253, 10.1038/nature09558.

Sparks, R. S. J., and K. V. Cashman (2017), Dynamic Magma Systems: Implications for Forecasting Volcanic Activity, *Elements*, *13*(1), 35–40, 10.2113/gselements.13.1.35.

Sparks, R. S. J., C. Annen, J. D. Blundy, K. V. Cashman, A. C. Rust, and M. D. Jackson (2019), Formation and dynamics of magma reservoirs, *Philosophical Transactions of the Royal Society A: Mathematical, Physical and Engineering Sciences*, *377*(2139), 20180,019, 10.1098/rsta.2018.0019.

Taira, T., R. B. Smith, and W. L. Chang (2010), Seismic evidence for dilatational source deformations accompanying the 2004-2008 Yellowstone accelerated uplift episode, *Journal of Geophysical Research: Solid Earth*, 10.1029/2008JB006281.

Tait, S., C. Jaupart, and S. Vergniolle (1989), Pressure, gas content and eruption periodicity of a shallow, crystallizing magma chamber, *Earth and Planetary Science Letters*, *92*(1), 107–123, 10.1016/0012-821x(89)90025-3.

Tarantola, A., and B. Valette (1982), Generalized nonlinear inverse problems solved using the least squares criterion, 10.1029/RG020i002p00219.

Tizzani, P., M. Battaglia, R. Castaldo, A. Pepe, G. Zeni, and R. Lanari (2015), Magma and fluid migration at Yellowstone Caldera in the last three decades inferred from InSAR, leveling, and gravity measurements, *Journal of Geophysical Research-Solid Earth*, *120*(4), 2627–2647, 10.1002/2014jb011502.

Todesco, M., A.P. Rinaldi, and M. Bonafede, (2010), Modeling of unrest signals in heterogeneous hydrothermal systems, *Journal of Geophysical Research-Solid Earth*, *115*, B09213, 10.1029/2010JB007474.

Townsend, M., C. Huber, W. Degruyter, and O. Bachmann (2019), Magma chamber growth during inter-caldera periods: insights from thermo-mechanical modeling with applications to Laguna del Maule, Campi Flegrei, Santorini, and Aso, *Geo-*

*chemistry, Geophysics, Geosystems*, 10.1029/2018GC008103.

Trasatti, E., M. Polcari, M. Bonafede, and S. Stramondo (2015), Geodetic constraints to the source mechanism of the 2011-2013 unrest at Campi Flegrei (Italy) caldera, *Geophysical Research Letters*, 10.1002/2015GL063621.

Troise, C., G. De Natale, R. Schiavone, R. Somma, and R. Moretti (2019), The Campi Flegrei caldera unrest: Discriminating magma intrusions from hydrothermal effects and implications for possible evolution, 10.1016/j.earscirev.2018.11.007.

Vasco, D. W., C. M. Puskas, R. B. Smith, and C. M. Meertens (2007), Crustal deformation and source models of the Yellowstone volcanic field from geodetic data, *Journal of Geophysical Research: Solid Earth*, 10.1029/2006JB004641.

Waite, G. P., and R. B. Smith (2002), Seismic evidence for fluid migration accompanying subsidence of the Yellowstone caldera, *Journal of Geophysical Research: Solid Earth*, 10.1029/2001jb000586.

Walwer, D., M. Ghil, and E. Calais (2019), Oscillatory nature of the Okmok volcano's deformation, *Earth and Planetary Science Letters*, 10.1016/j.epsl.2018.10.033.

Wdowinski, S., and S. H. Hong (2015), Wetland inSAR: A review of the technique and applications, in *Remote Sensing of Wetlands: Applications and Advances*, 10.1201/b18210.

Wicks, C., W. Thatcher, and D. Dzurisin (1998), Migration of fluids beneath Yellowstone caldera inferred from satellite radar interferometry, *Science*, *282*(5388), 458–462, 10.1126/science.282.5388.458.

Wicks, C. W., W. Thatcher, D. Dzurisin, and J. Svarc (2006), Uplift, thermal unrest and magma intrusion at Yellowstone caldera, *Nature*, 10.1038/nature04507.

Wicks, C. W., D. Dzurisin, J. B. Lowenstern, and J. Svarc (2020), Magma intrusion and volatile ascent beneath Norris Geyser Basin, Yellowstone National Park, *Journal of Geophysical Research: Solid Earth*, *n/a*(n/a), e2019JB018,208, 10.1029/2019JB018208.

linedepth linedepth

# Supporting Information for "Dynamics of episodic magma injection and migration at Yellowstone caldera: revisiting the 2004-2009 episode of caldera uplift with InSAR and GPS data"

Francisco Delgado[1], Raphaël Grandin[1]

[1]Université de Paris, Institut de Physique du Globe de Paris, CNRS, F-75005 Paris, France

## Contents of this file

1. Text S1 to S4

2. Figures S1 to S10

**Text S1. GPS processing**

We use daily position time series processed by the Nevada Geodetic Laboratory (Blewitt et al., 2018) with the JPL GIPSY-OASIS software and a precise point positioning method. These time series are equivalent in quality compared to those used by Wicks et al., (2020) in their study of unrest at Yellowstone between 1996 and 2020. Solutions are referenced to stable North America in the NA12 reference frame (Figure S1), which represents the North America stable interior far from plate boundary effects and post glacial rebound. Since the Yellowstone caldera is located east of the active Basin and Range province, no other geologic processes except for volcano deformation, the post-seismic signal of the 1959 Hebgen Lake earthquake (Puskas et al., 2007), and seasonal processes like surface loading are recorded by the GPS data. We calculate the cumulative displacement of GPS vectors as the difference between the average positions in time windows spanning 10 days before the onset of uplift on July 15 2004, and afterwards on September 1 2009. This way, the GPS data spans the same time interval than the InSAR data. Since the end and start of uplift occurred in the summer, the time-averaged static displacements contain the same amount of seasonal signal, which cancels out when subtracting the total displacements between the two time periods of interest. Puskas et al., (2007) have shown that the velocities calculated by campaign GPS stations during 2000-2003 are almost insensitive to the post-seismic effects of the Hebgen Lake earthquake. Therefore we consider these effects to be negligible with respect to the large magnitude of volcanic unrest in the GPS data.

We also attempted to use the same GPS data but processed by UNAVCO. These time series have more data points between 2000 and 2004 that span the onset of deformation

for the WLWY, LKWY and HVWY stations. However, the horizontal vectors calculated for some stations have different magnitudes than the vectors calculated from the Nevada data. Furthermore, the UNAVCO GPS data provide a worse fit to the two sill model with uniform opening (next section). Therefore, we do not consider this data further.

**Text S2. InSAR processing**

We use InSAR data acquired by the ENVISAT, ALOS-1 and TerraSAR-X/TanDEM-X satellites. Perpendicular baseline ($B_{perp}$) plots for all data are shown in Figure S2. Winter C-band and X-band data were not used because interferograms calculated with these images are incoherent.

**ENVISAT data**

The ENVISAT data span from September 2003 to October 2010. Although there are two ENVISAT IM2 images acquired in September 2003, the large Doppler centroid differences of these images with respect to the rest of the data set precludes estimation of the time series before September 2004. Hence, the InSAR does not have a high enough temporal resolution to resolve the onset of inflation at the caldera floor in September/October 2004. ENVISAT interferograms were processed with the ISTerre NSBAS software (Doin et al., 2011), which is partially based on the JPL ROI_PAC software (Rosen et al., 2004). This processing chain includes a series of corrections that are designed to enhance the coherence of ENVISAT data, including common Doppler centroid filtering, spectral range filtering, geometric coregistration to a master SLC, DEM error corrections, and corrections to atmospheric phase delays prior to phase unwrapping (Doin et al., 2011; Jolivet et al., 2011). Unlike other software, corrections with NSBAS are directly applied on the unfiltered wrapped data.

The topographic phase was removed with the 1 arcsec SRTM DEM. Afterwards, pixels were averaged to 20 looks in azimuth and 4 in range. Interferograms were corrected for atmospheric phase delays with the ERA5 (ECMWF re-analysis) atmospheric model and an empirical function that correlates the phase and the topography on top of the ERA5 corrected interferograms. These corrections were not applied to the IM1 ascending data because they increased the data variance (Figure S3). The relatively low-relief of ∼300 m at Yellowstone implies that most of the atmospheric signals are turbulent and not correlated with the topography, except outside the caldera. Therefore, the ERA-5 correction slightly reduces the variance except for the IM2 descending track because this data set contains the most turbulent atmospheric signals, and these signals cannot be corrected with the ERA-5 model (Figure S3). Empirical atmospheric corrections and range and azimuth ramps were removed directly on the wrapped interferograms and re-estimated with a network-consistent inversion. DEM error corrections (Ducret et al., 2014) were applied only for the IM2 tracks because this correction relies on a heavily redundant interferometric network which is not the case of the IM1 data. Interferograms were filtered with a cascade sliding window algorithm and unwrapped with both the branch and cut (Goldstein et al., 1988) and SNAPHU minimum cost flow algorithms (Chen and Zebker, 2001). In general, coherence is quite good, allowing us to calculate interferograms that span up to two years and with perpendicular baselines ($B_{perp}$) smaller than 500 m (Figure S2). Interferograms with clear double-bounce signals in areas with wetlands (e.g., Wdowinski and Hong, 2015) introduce sharp phase discontinuities that lead to phase unwrapping errors, even after filtering. Therefore small baseline interferograms with these artifacts were not included in the time series.

ENVISAT time series were calculated with the GIAnT toolbox and the SBAS method (Berardino et al., 2002) for pixels that are coherent in all the selected interferograms (pairs with dashed lines in Figure S2). Prior to time series analysis, interferograms were referenced to a stable non-deforming area (black crosses in Figure 2). We calculate interferograms of total displacement subtracting the first to the last epoch spanning the unrest episode in the reconstructed time series (interferogram hereafter). We prefer this over rate maps of mean velocity because the deformation is non-linear during the episode of uplift. We calculate data uncertainties with the data standard deviation in areas of no deformation. In general the data uncertainty ranges between 0.6 and 0.9 cm for the interferograms, $\sim$20 times lower than the amplitude of the deformation signals. Had we used the grids of mean velocity, the data uncertainty would be even lower because velocity fitting results in a low pass filtering procedure. However, this approach does not consider the non-linearity of the cumulative deformation signal. The noisiest interferogram is from the IM2 descending track because it contains more turbulent atmospheric signals than any of the other three sets.

**ERS-1/2 data**

We use ERS-1/2 descending data (Figure S4) to qualitatively compare the caldera subsidence during 1992-1995 (Aly and Cochran, 2011; Wicks et al., 1998) and uplift at NGB during 1996-2000 (Wicks et al., 2006) with that of the 2004-2009 unrest. The 1992-1995 data are a stack of two interferograms acquired during 1992-1993 and 1993-1995 and processed with 20 looks in azimuth and 4 in range with a power spectrum filtering strength of 0.5. Ramps were removed from the interferograms prior to stacking. The 1996-2000 interferogram was processed with 40 looks in azimuth and 8 looks in range and with a

power spectrum filtering strength of 0.7 to increase the coherence. Since the ERS-1/2 and ENVISAT IM2 descending have the same viewing geometry and the satellite paths are the same, these descending interferograms can be directly compared with each other for changes in the wavelength and location of the line-of-sight deformation. ERS-2 data after 2001 have inaccurate Doppler centroids, resulting in focusing problems and very few useful images for interferometry. We selected the same error-free ERS-2 images that Tizzani et al., (2015) processed during 2004-2009, but the data have very low coherence, resulting in very few coherent interferograms. Therefore ERS-2 data from 2004-2009 were not considered further.

**ALOS-1 data**

ALOS-1 data were processed with the NSBAS software with the same workflow as the ENVISAT data. We do not use ALOS-1 data between 2007-2010 due to its much lower sensitivity to subtle displacements of 2 cm/yr or less. Indeed, the caldera uplift and the subsidence at NGB that should be detected in 2007-2009 interferograms are not observed in many ALOS-1 pairs, even if they span almost 3 years. Several winter to winter pairs and interferograms that span different seasons of the year show strong double-bounce effects in wetlands. These effects are more problematic for L-band than C-band data. The ALOS-1 data for track 197 was chain stacked to span early 2010 to early 2011 when ENVISAT did not acquire data (Figure S2). We use a strong cascade sliding window filter for the interferograms with the double-bounce effects, but this is not able to cope with the phase discontinuities and tropospheric anomalies that cannot be completely corrected with the ERA-5 and empirical corrections. The stack of seven strict small baseline interferograms

records multiple unwrapping errors, double bounce signals and no clear evidence of caldera subsidence during February 2010 - February 2011 (Figure S5).

**TerraSAR-X data**

TerraSAR-X data were processed with the ISCE software following standard procedures, and with the 10 m USGS DEM to remove the topographic phase. Pixels were averaged 16 times prior to filtering and phase unwrapping and pixels below a coherence threshold of 0.35 were masked. Prior to the InSAR time series calculation, interferograms were referenced to a 100 by 100 pixel box in the few non-deforming areas (black crosses in Figure 2). We prefer this procedure instead of removing a ramp with an arbitrary offset due to the almost lack of non-deforming areas in the small TSX swaths. GPS deramping was not successful due to the small number of stations available during the time period – at most 4 per TSX track. Due to the small number of acquisitions during 2011 and 2012, and the near secular subsidence observed during this time period by the GPS data, we decided to stack the best interferograms that span this subsidence episode (2-6 per track). Atmospheric corrections were attempted with the North American Regional Reanalysis (NARR) and ERA-I atmospheric models implemented in the GIAnT toolbox (Jolivet et al., 2014), but the poor temporal resolution of these corrections imply that they do not significantly reduce the atmospheric phase delays. Hence, these interferograms were not corrected for atmospheric phase delays.

**Text S3. Data inversion**

Prior to source modeling, linear ramps were estimated in areas with no deformation and removed from the interferograms. The data were then downsampled with a resolution-based algorithm (Lohman and Simons, 2005) with a sill geometry at a depth of 15 km.

This source is only used to focus the downsampling in areas with deformation signals, with coarser downsampling in far-field areas with residual atmospheric phase delays (e.g., Fig. 7a-c in Lohman and Simons, 2005), and not to enforce a prior source model. Downsampling with a shallower sill does not result in a vastly different number of downsampled patches. We use a diagonal data covariance matrix for the InSAR data because the data have a very weak spatial correlation no bigger than a few downsampled pixels and because the far-field data standard deviation in non-deforming areas is $\sim$7 mm. Both GPS and InSAR data were weighted with the inverse of their uncertainties. For InSAR, this only takes into account the effect of the atmospheric phase delays that remain in the data after multiple corrections. Data were inverted with the neighborhood algorithm (Sambridge, 1999) (hereafter NA), a non-linear inversion method which iteratively searches for the best-fit model parameters avoiding local minima, and the Levenberg-Marquardt (LM) algorithm. Due to the vastly different amount of GPS and InSAR data points – 10 vs $\sim$2500 points, the GPS data should be weighted such that the InSAR data will not dominate the best-fit model. Hence, the GPS data were weighted with factors of 1, 0.2 and 0.1 to augment the relative weight of this data set with respect to InSAR and to test the optimal weighting for joint inversions (e.g., Fialko, 2004). Inversions with these weighting factors result in models that do not significantly differ from each other, fitting both the GPS and InSAR data equally well. Hence, both data sets are assigned equal weights in the non-linear inversion.

We invert the data in the following way. After the NA inversion converged resulting in models that do not significantly differ from each other, we use the best-fit NA model as the initial point of an inversion with the LM algorithm to find the global best-fit model.

Inversions for all 14 non-linear model parameters (X and Y sill centroid, depth, strike, dip, width, length) for the two sub-horizontal dislocations fail to converge to a stable family of solutions because the sources lie on top of each other and thereby have strong trade-offs. After several iterations we fix the dip and strike of the caldera source to $0^{o}$ and $54^{o}$ and the NGB source dip to $0^{o}$ because they converge rapidly to these values. Inversions for the rest of the 11 model parameters converge for the caldera source but not for the NGB source. At this point we discard models in which the NGB and the caldera sills intersect with each other. We then fix the 7 caldera source parameters and the NGB source centroid and depth, and invert for the NGB sill strike, length and width (Figure S6, Figure S7). This is similar to other studies where multiple deformation sources are iteratively determined (e.g., Bagnardi et al., 2013). Because we iteratively fixed the model parameters to ensure inversion convergence, it is neither feasible nor meaningful to calculate model parameter uncertainties. However, we calculate the source depths uncertainties with RMS plots in which all model parameters are fixed except for the sill centroid depths (Figure S8). To ensure that the model is robust, we also inverted the data with a different algorithm based on a non-linear least square iterative inversion (Tarantola and Valette, 1982), which gave very similar results. We use the best-fit caldera sill model as the starting point for an inversion for a sill and an ellipsoidal crack with the boundary element code DEFVOLC for the IM2 interferogram (Figure S9).

The distributed sill opening model is regularized with Laplacian smoothing to avoid unrealistic oscillatory opening and the amount of smoothing is chosen by the "L curve" corner (Aster et al., 2018). We jointly invert GPS and InSAR data with weighting factors $\alpha_W$ between 1 (equal weight for GPS and InSAR), 0.5 and 0.2 to augment the GPS con-

tribution with respect to InSAR. The model fit to the GPS data improves with $\alpha_W = 0.5$ at the expense of a worst data fit to the InSAR data near NGB. Smaller values of $\alpha_W$ result in a near complete fit to the GPS data but higher residuals for the InSAR data. Therefore, we invert the data with $\alpha_W = 0.5$ which provides good data fits without significantly increasing the residual for the NGB signal recorded by the interferograms (Figure 4-5, Figure S10).

**Text S4. Solution to the equations of pressure change for the caldera and NGB sills**

**Magma compressibility**

For the general case of volume change due to a pressure change in a reservoir (Equation 1)

$$\Delta P_{s,d} = \frac{\Delta V_{s,d}}{V_{s,d}(\beta_m + \beta_w)} \tag{1}$$

with $V$ the reservoir volume, $\beta_m$ the magma compressibility and $\beta_w$ the reservoir compressibility, equal to $\frac{3}{4G}$ for a sphere and $\frac{8(1-\nu)}{3\pi}\frac{a_{s,d}^3}{G}\frac{1}{V}$ for a penny-shaped crack (Amoruso and Crescentini, 2009). This results in the Equation 2

$$\Delta V_{s,d} = \Delta P_{s,d}(\frac{\pi a_{s,d}^3 \gamma}{G} + V_{s,d}\beta_m) \tag{2}$$

If magma compressibility is taken into account, then the time constants in Equation 10 become

$$\begin{aligned}\beta &= \frac{\pi a_2^4 G}{8\mu_2 H_2(\pi a_s^3\gamma + GV_s\beta_m)} \\ \alpha &= \frac{\pi a^4 G}{8\mu H(\pi a_s^3\gamma + GV_s\beta_m)} \\ \epsilon &= \frac{\pi a_2^4 G}{8\mu_2 H_2(\pi a_d^3\gamma + GV_d\beta_m)}\end{aligned} \tag{3}$$

**Method of solution**

Rearranging terms results in Equations 8-9 in the main text

$$\frac{d\Delta P_s}{dt} = -\Delta P_s(\alpha+\beta) + \Delta P_d\beta + \alpha(\Delta\bar{P} + \Delta\rho g H) + \beta\Delta\rho_2 g H_2 \tag{4}$$

$$\frac{d\Delta P_d}{dt} = \Delta P_s\epsilon - \Delta P_d\epsilon - \epsilon\Delta\rho_2 g H_2 \tag{5}$$

Equation 4 - Equation 5 form a linear system of non-homogeneous differential equations that can be casted in matrix form (Equation 6 - Equation 7)

$$\begin{bmatrix}\frac{d\Delta P_s}{dt} \\ \frac{d\Delta P_d}{dt}\end{bmatrix} = \begin{bmatrix}-\alpha-\beta & \beta \\ \epsilon & -\epsilon\end{bmatrix}\begin{bmatrix}\Delta P_s \\ \Delta P_d\end{bmatrix} + \begin{bmatrix}\beta\Delta\rho_2 g H_2 + \alpha\Delta\rho g H + \alpha\Delta\bar{P} \\ -\epsilon\Delta\rho_2 g H_2\end{bmatrix} \tag{6}$$

$$\frac{d\bar{P}}{dt} = G\bar{P} + H \tag{7}$$

with $\bar{P} = [\Delta P_s, \Delta P_d]^T$ the vector that contains the functions for the shallow and deep reservoir pressure. The solution to Equation 7 is a function of the form $\vec{\bar{P}}(t) = \vec{v_1}e^{\lambda_1 t} + \vec{v_2}e^{\lambda_2 t} + \vec{a}e^{-\frac{t}{\tau_m}} + \vec{b}$ with $\vec{v_{1,2}}$ and $\lambda_{1,2}$ the eigenvectors and eigenvalues of $G$, and the last two terms are vectors derived from the method of undetermined coefficients for the non-homogeneous terms (last term on the right-hand side of Equation 7).

## Figures

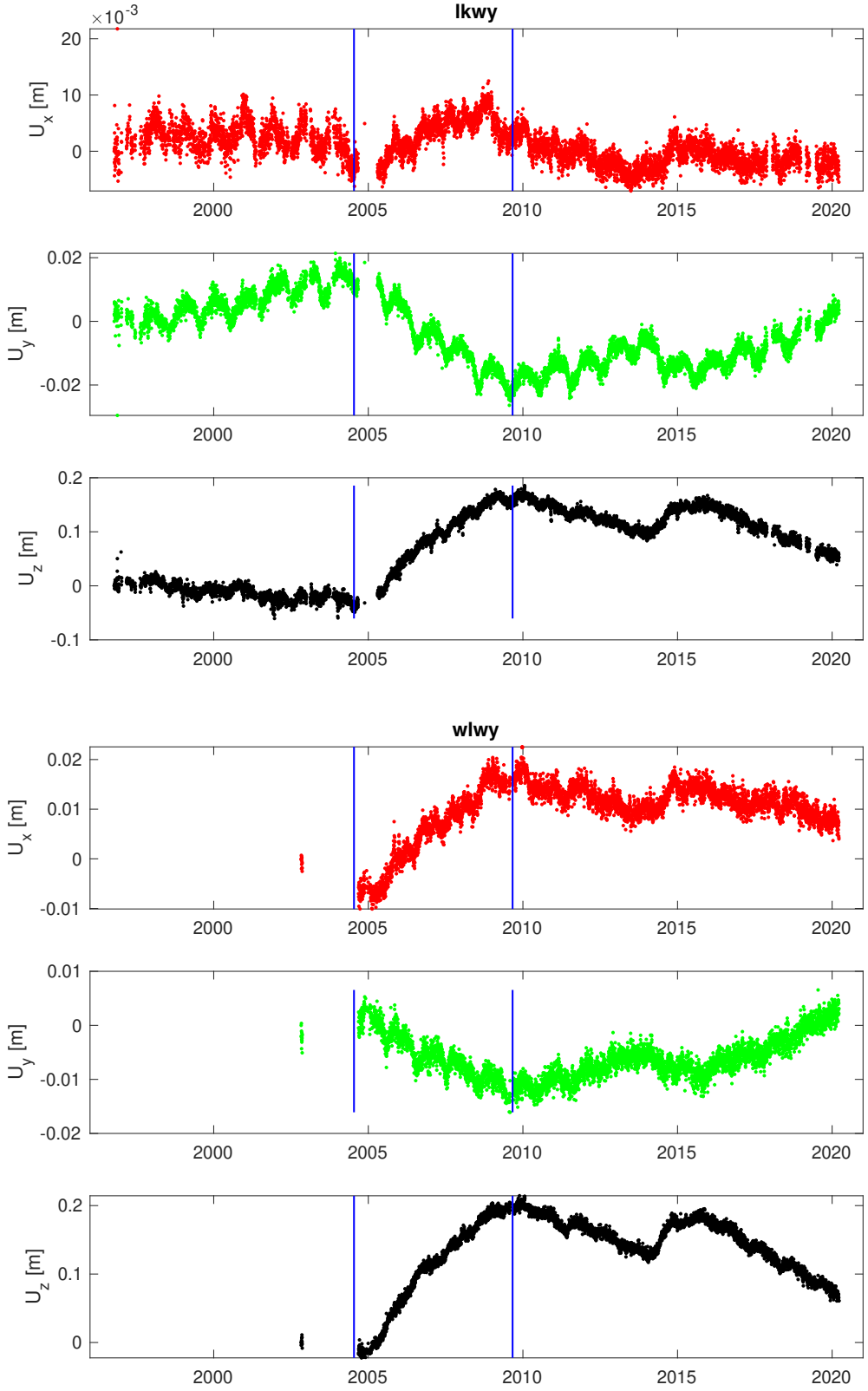

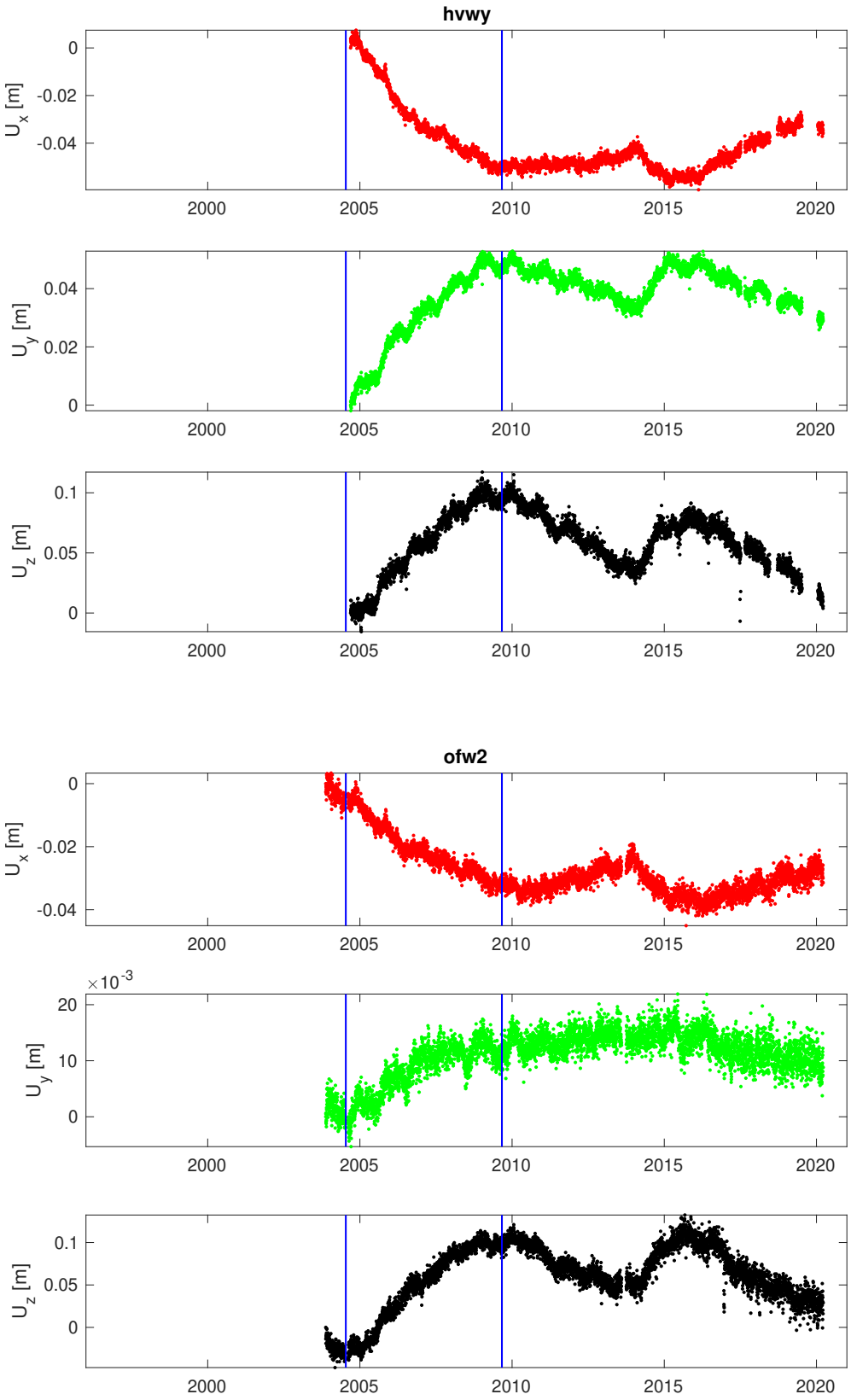
hvwy
U_x [m]
0
-0.02
-0.04
2000
2005
2010
2015
2020
U_y [m]
0.04
0.02
0
U_z [m]
0.1
0.05
ofw2
×10^-3
20
10

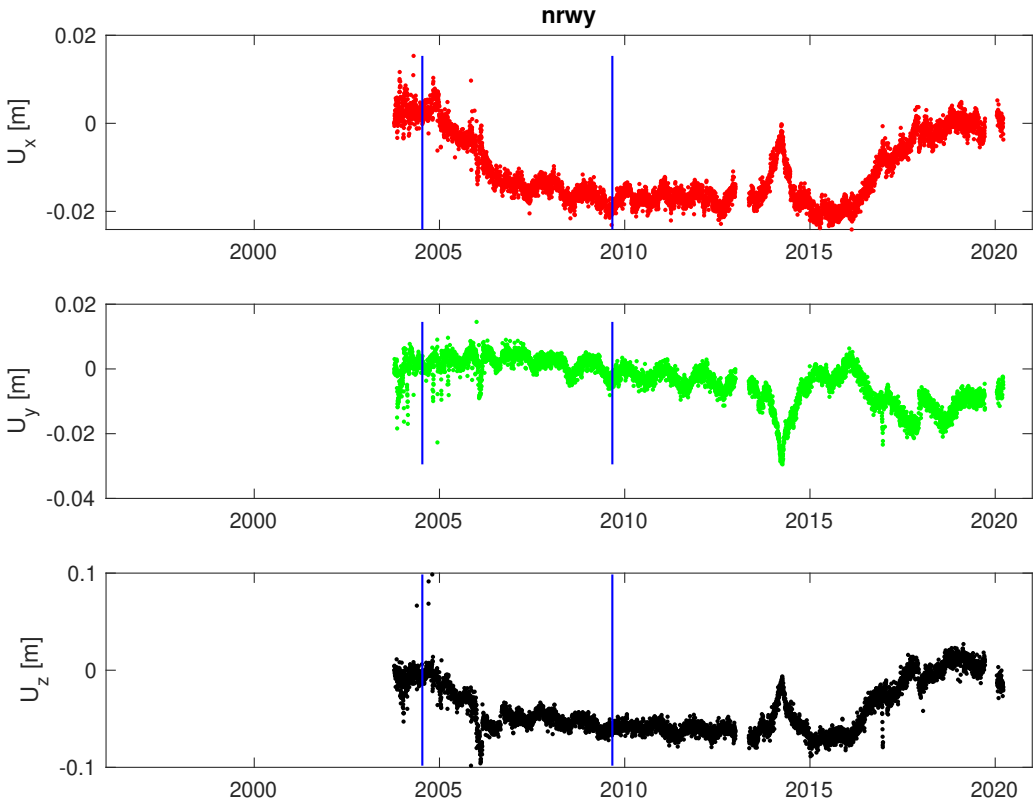


Figure S1: Continuous GPS time series for east ($U_x$), north ($U_y$) and vertical ($U_z$) components. The figure title shows the station name. Vertical blue lines show the 2004-2009 episode of uplift for which positions were averaged on windows of +/-10 days and subtracted to retrieve the total displacement for each component.

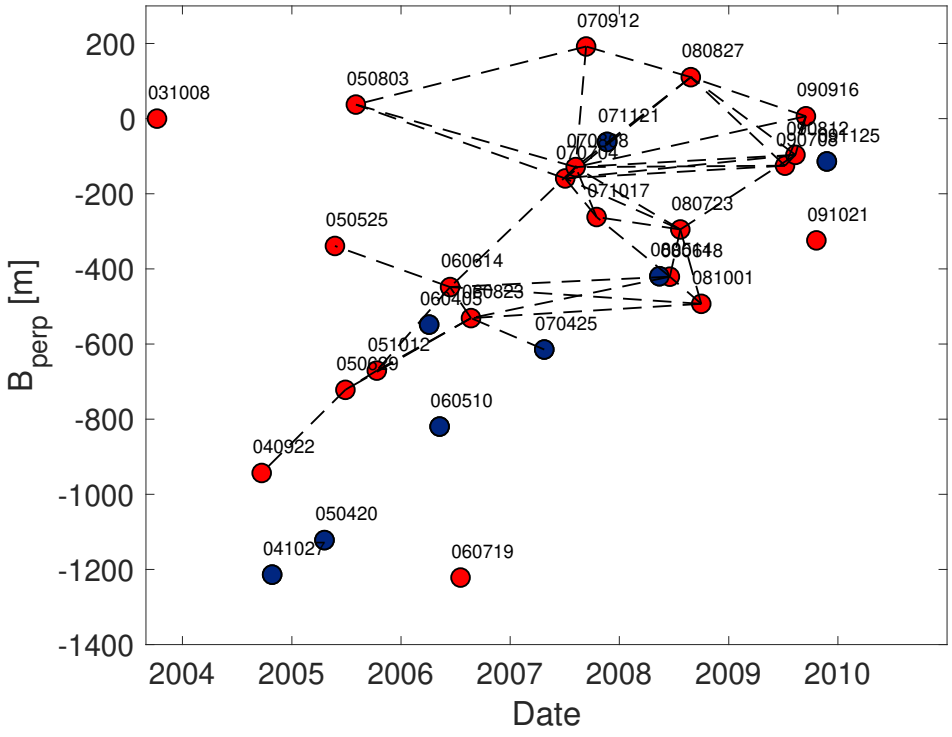

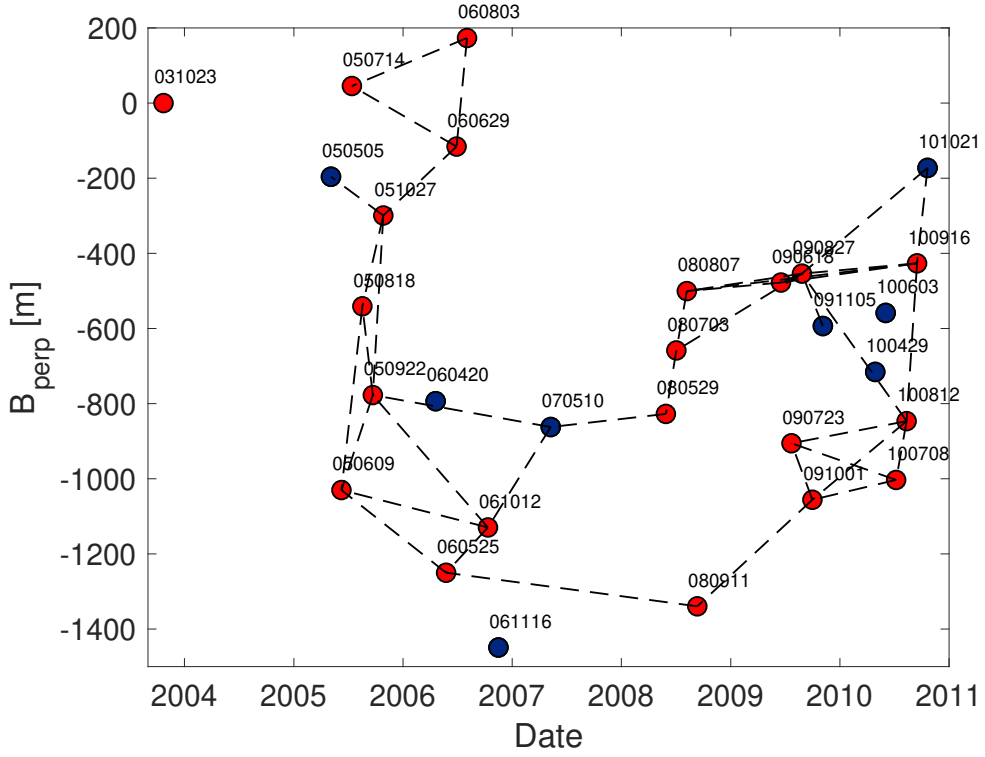
060803
050714
031023
060629
050505
101021
051027
090827
100916
080807
090618
050818
100603
091105
080703
100429
050922
060420
080529
100812
070510
090723
050609
100708
091001
061012
060525
080911
061116
200
0
-200
-400
-600
-800
-1000
-1200
-1400
B perp [m]
2004
2005
2006
2007
2008
2009
2010
2011
Date

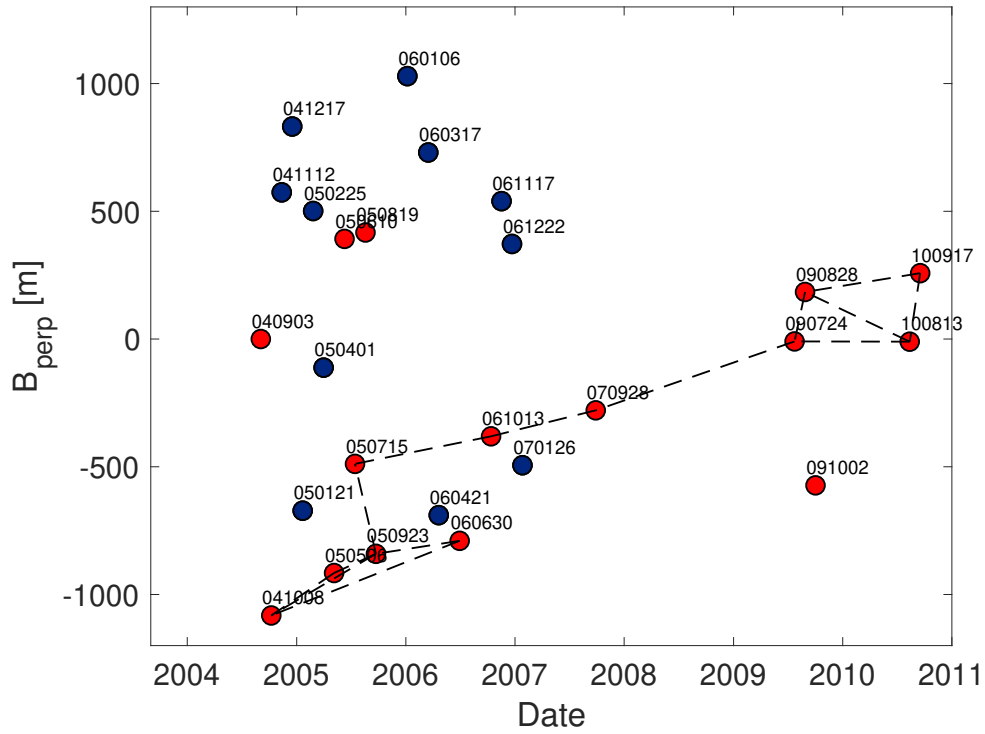
060106
041217
060317
041112
050225
061117
050819
061222
100917
090828
040903
090724
100813
050401
070928
061013
050715
070126
091002
050121
060421
060630
050923
041008
1000
500
0
-500
-1000
B perp [m]
2004
2005
2006
2007
2008
2009
2010
2011
Date

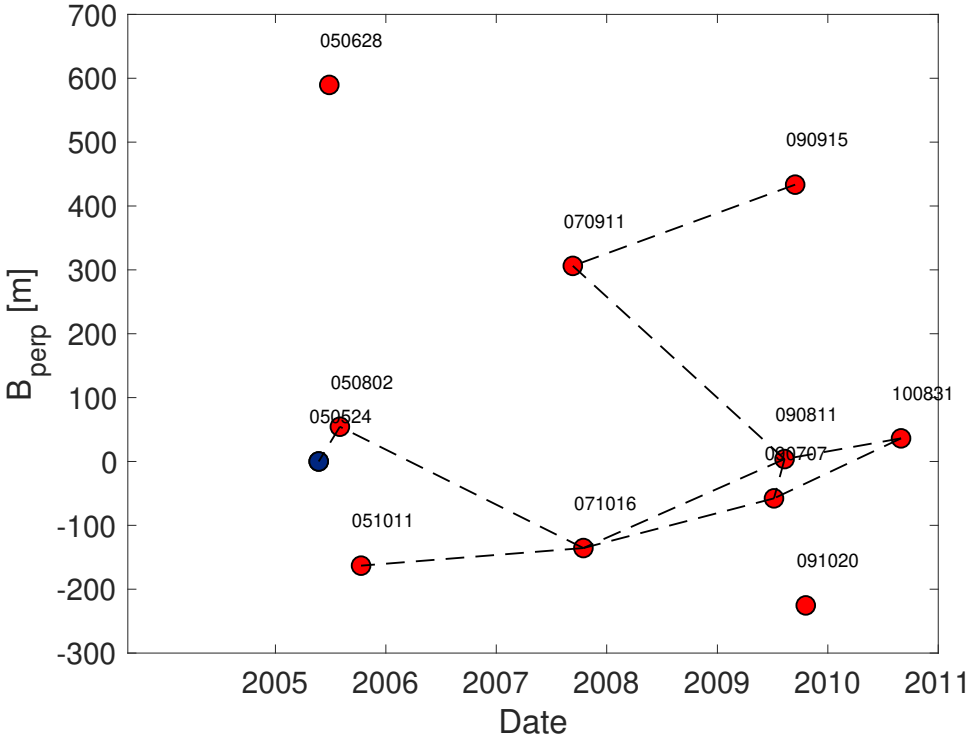
700
600
500
400
300
200
100
0
-100
-200
-300
B perp [m]
2005
2006
2007
2008
2009
2010
2011
Date
050628
090915
070911
050802
050524
090811
100831
090707
071016
051011
091020

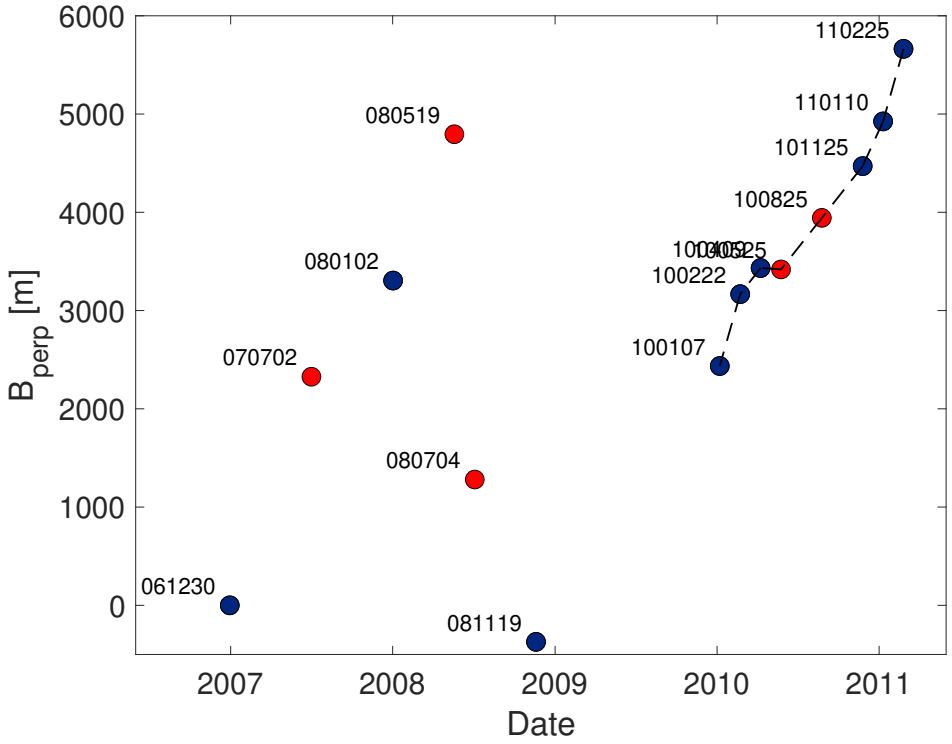
6000
5000
4000
3000
2000
1000
0
B perp [m]
2007
2008
2009
2010
2011
Date
110225
080519
110110
101125
100825
080102
100222
070702
100107
080704
061230
081119

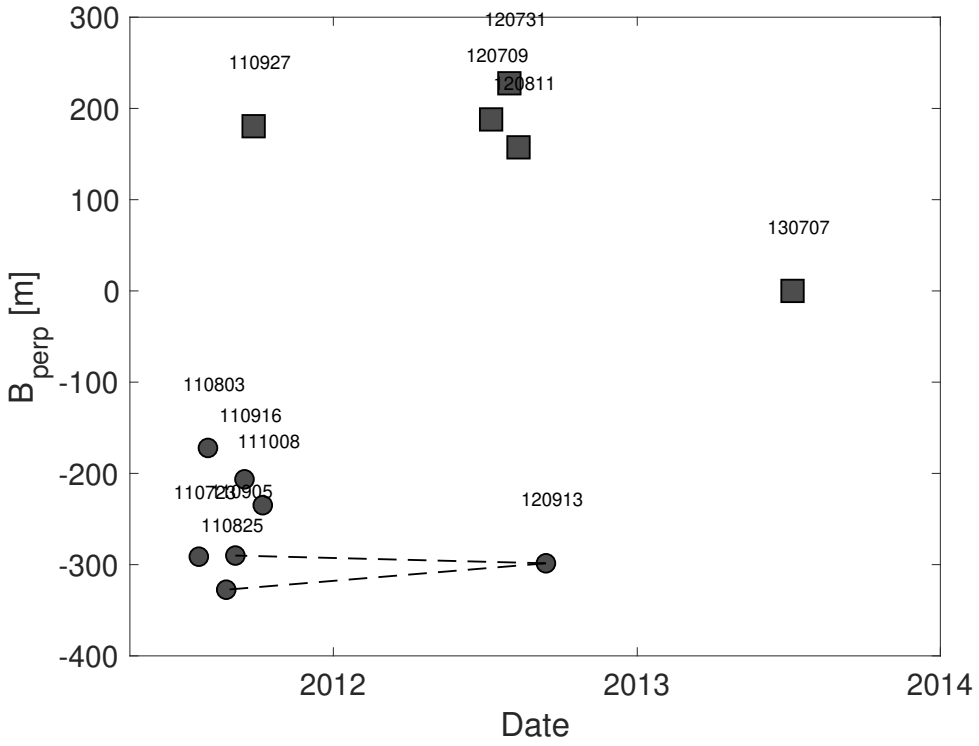
300
200
100
0
-100
-200
-300
-400
B perp [m]
2012
2013
2014
Date
120731
110927
120709
120811
130707
110803
110916
111008
110825
120913

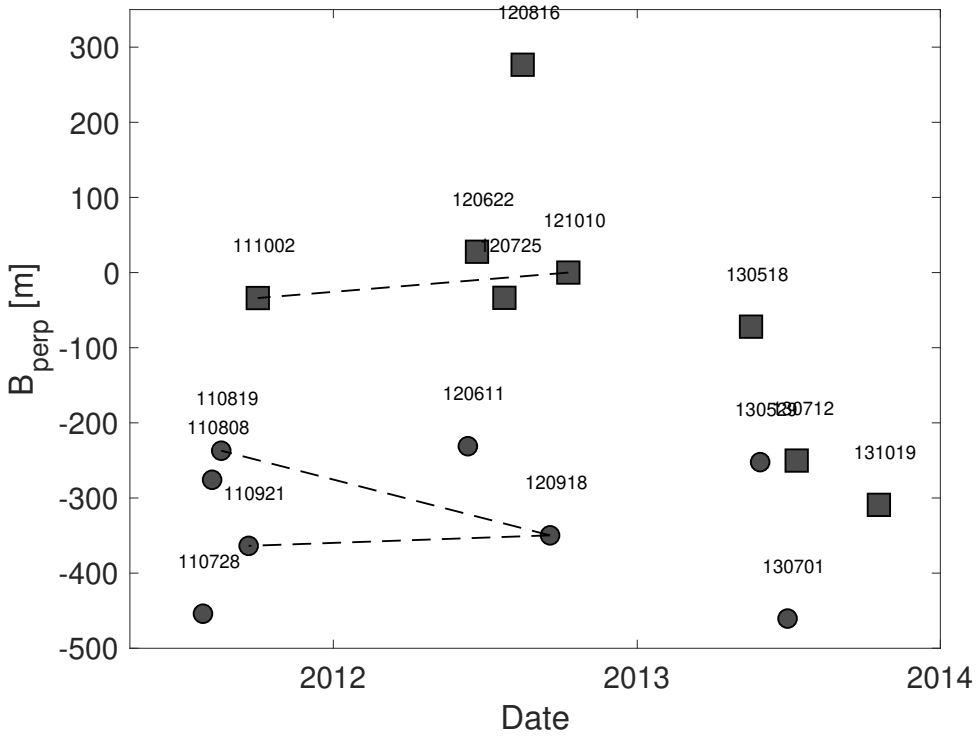
300
200
100
0
-100
-200
-300
-400
-500
B perp [m]
2012
2013
2014
Date
120816
120622
121010
111002
120725
130518
110819
120611
110808
120918
131019
110921
110728
130701

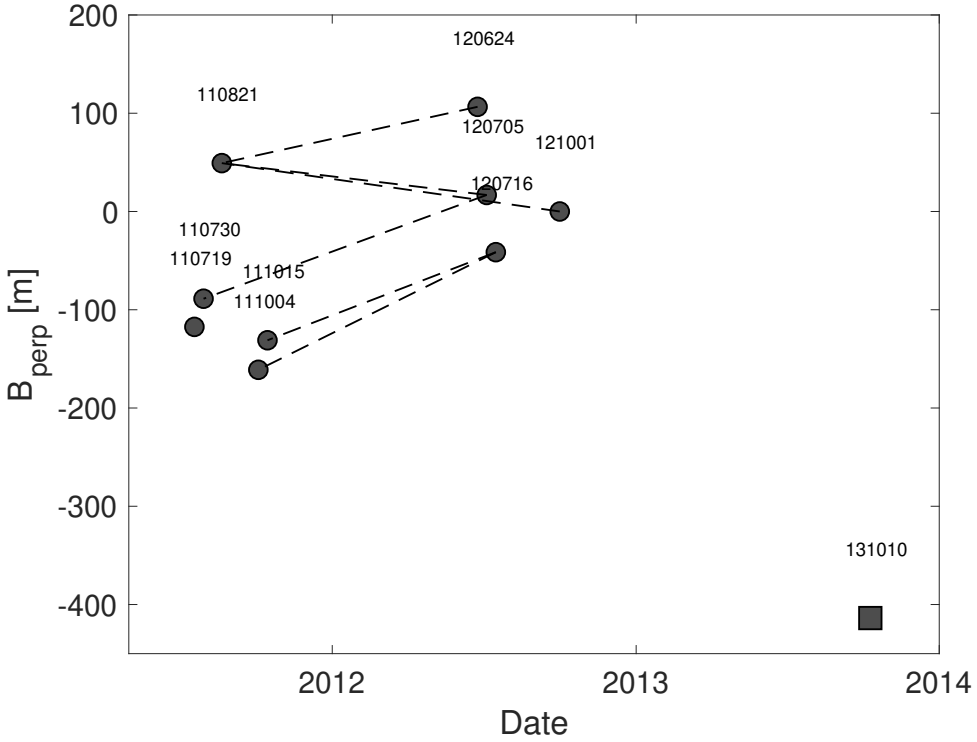


Figure S2: $B_{perp}$ plot for ENVISAT (a IM2 ascending track 320, b IM2 descending track 48, c IM1 ascending track 48, d IM1 descending track 31), ALOS-1 (e ascending path 197) and TerraSAR-X/TanDEM-X data (f ascending orbit 45, g ascending orbit 121, h descending orbit 159). Red and blue dots are winter and non-winter images for the ENVISAT and ALOS-1 data. Winter images were not included in the $B_{perp}$plot for the ENVISAT descending tracks. Circles and squares are TerraSAR-X and TanDEM-X images.

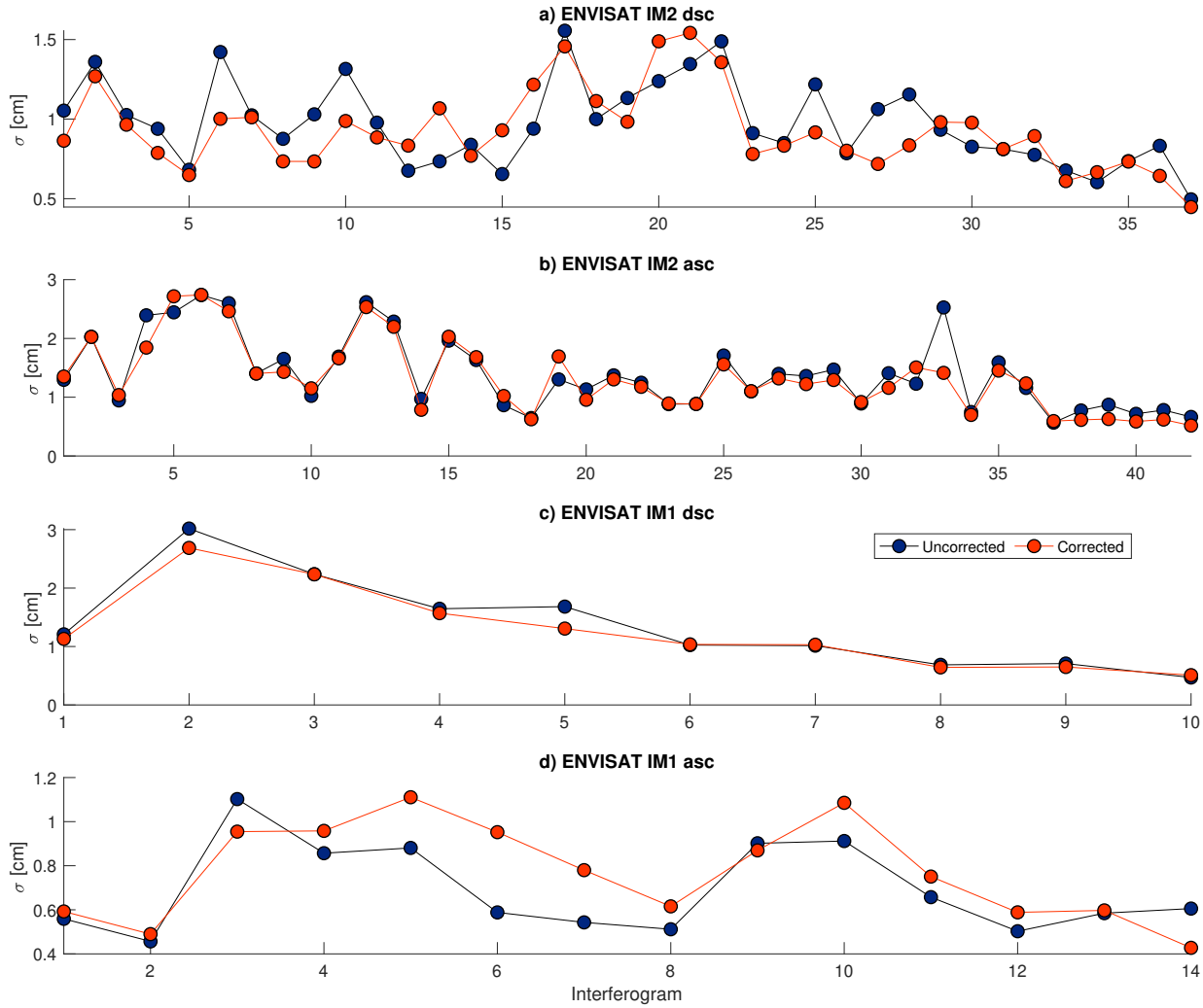


Figure S3: Statistics of atmospheric phase delays for the interferograms used in each of the ENVISAT time series. The title shows the ENVISAT track. The blue and orange circles are the standard deviation in non-deforming areas uncorrected and corrected with the ERA5 atmospheric model. The figure shows that ERA5 reduces the data standard deviation in more than half of the interferograms per track except for the ENVISAT IM1. Therefore this track was not corrected with ERA5.

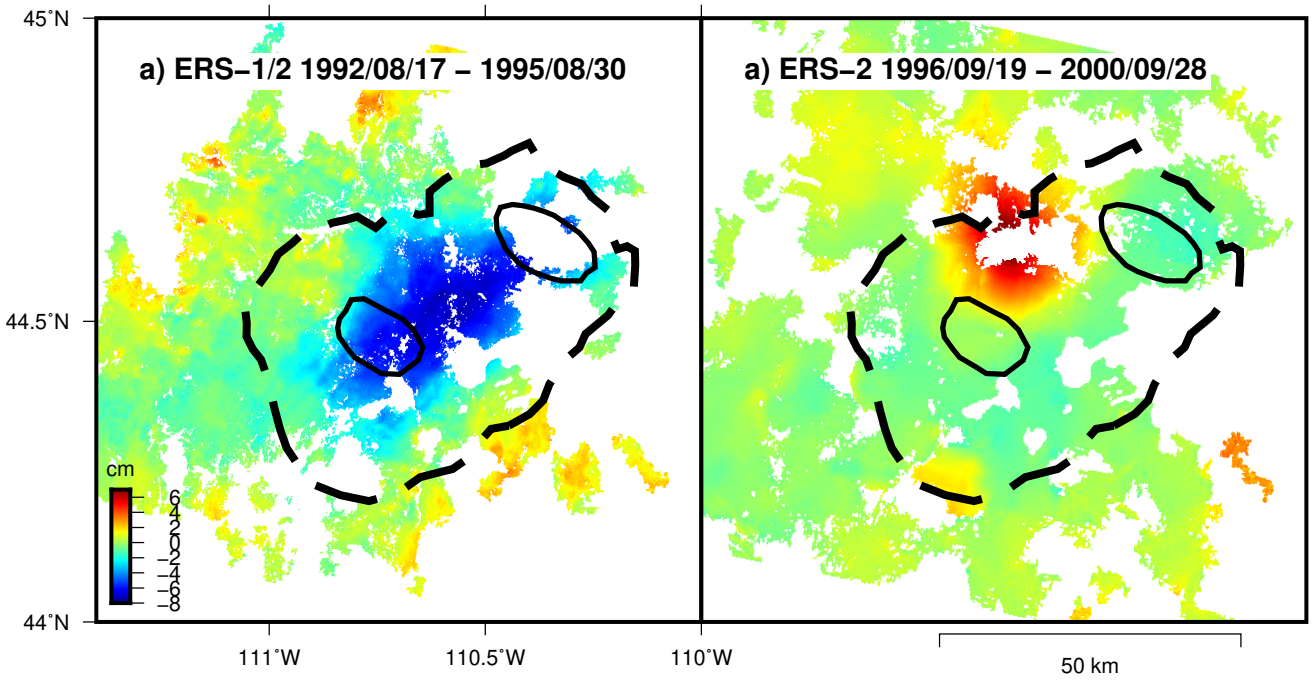


Figure S4: ERS-1/2 interferograms recorded between 1992 and 2000. A) Stack of two interferograms that spans 1992/08/17 - 1993/06/28 and 1993/06/28 - 1995/08/30 showing caldera subsidence (Wicks et al., 1998, Aly and Cochran, 2011) in a different location than uplift during 2004-2009 and subsidence during 2010-2012. B) Interferogram that spans 1996/09/19 - 2000/09/28 showing uplift at NGB (Wicks et al., 2006, Aly and Cochran, 2011) but in a different location than the subsidence during 2004-2009. The data are not modeled and only shown for visual comparison with the ENVISAT interferograms (Figure 2).

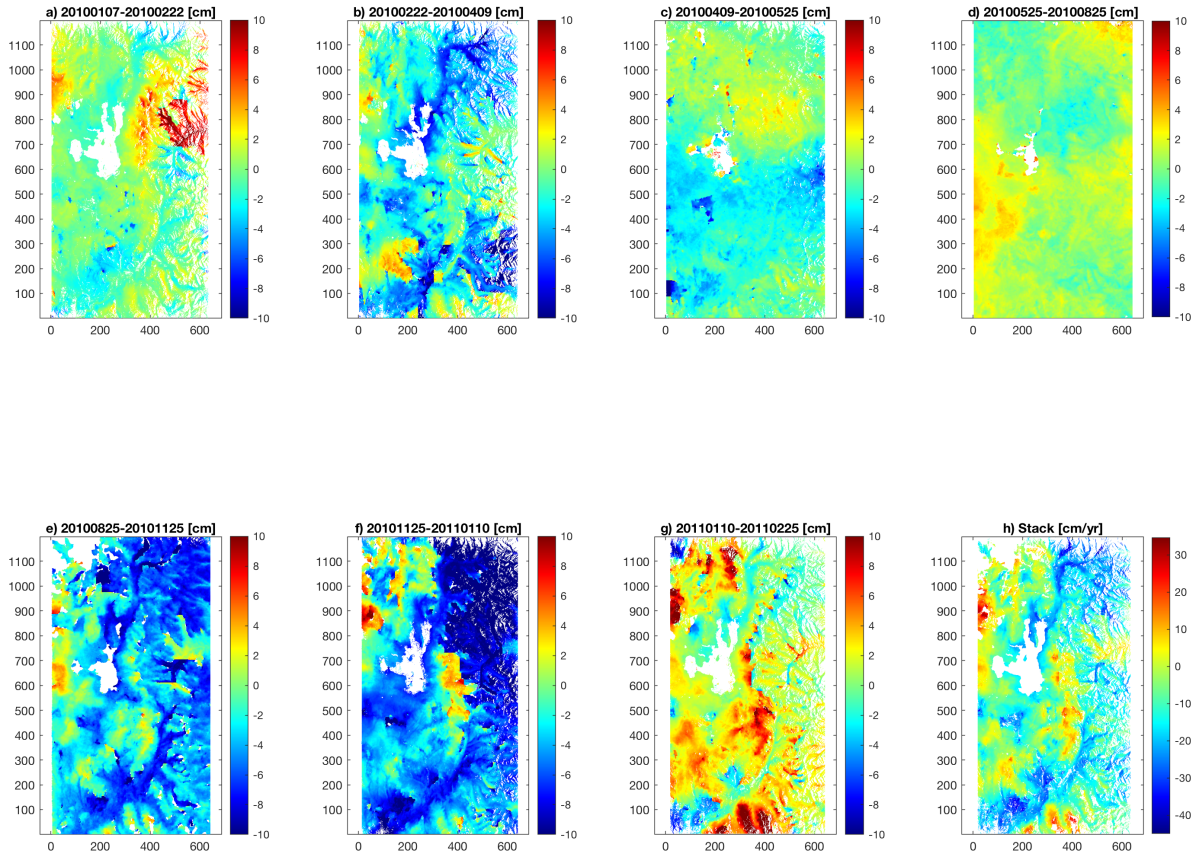


Figure S5: a-g) ALOS-1 interferograms in radar coordinates that span 46-92 days between January 2010 and February 2011 (Figure S2e). The titles show the date span of each interferogram. The data show several double bounce signals and unwrapping errors due to topography correlated phase delays that cannot be corrected with a linear function that correlates phase and topography. h) Mean ground velocity in the LOS direction calculated by stacking the preceding interferograms.

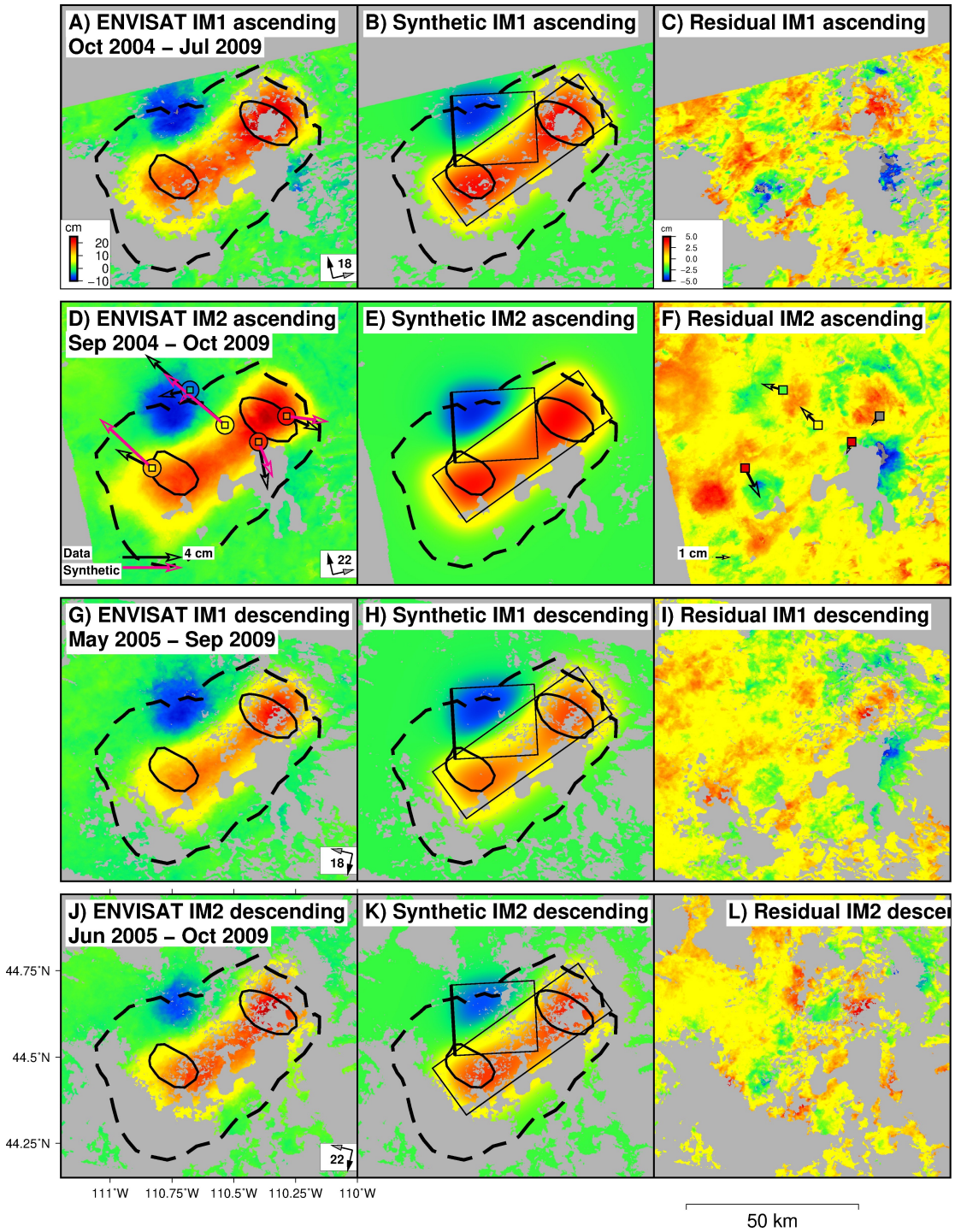


Figure S6: Interferograms (A,D,G,J), synthetic interferograms and GPS vectors (B,E,H,K), and residuals (C,F,I,L) for the ENVISAT interferograms for the inversion of two sub-horizontal dislocations with uniform opening. The black and pink arrows show the GPS vectors (Figure S1) and predicted displacement by best-fit sill models (black rectangles in E-H). The dots and squares in B show the GPS vertical displacement and synthetic displacements. The vertical component was not included in the inversion because they are less accurate than the horizontal components. Hence we only calculate the synthetic vertical displacement from the best-fit source model and subtract it from the data.

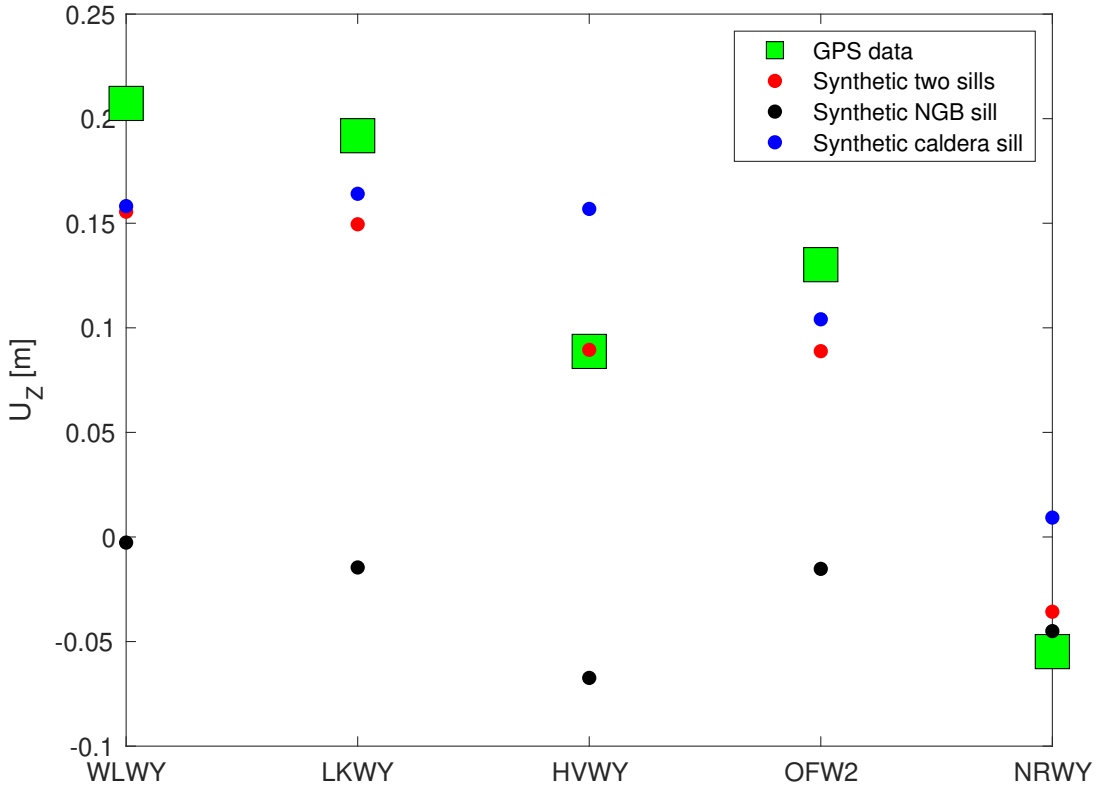


Figure S7: GPS vertical displacement (green squares) and displacement predicted by the best-fit model of two sills with uniform opening (dots). The blue and black circles show the synthetic displacement predicted by the caldera and NGB sources with uniform opening. The red dots show the synthetic vertical displacement predicted by the two sills. The figure shows that the vertical displacements measured by stations WLWY, LKWY and OFW2 are almost completely modeled by the opening of the caldera source. Therefore the GPS time series vertical displacement of these stations are sensitive to the caldera sill opening. The misfits of ∼5 cm with respect to the GPS data show that distributed opening is required to model the data due to localized uplift at SCD and MLD.

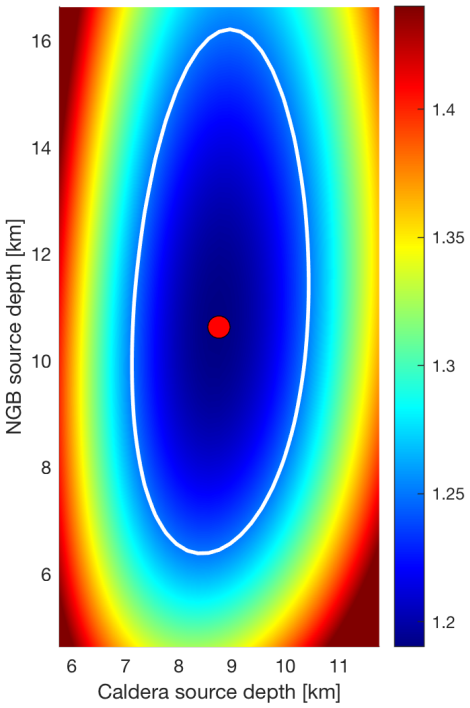


Figure S8: Root mean square (RMS) trade-off plot in cm for the caldera and NGB sill sources depths. The red dot is the RMS global minimum. The white line is the 5% contour above the global minimum and is used as a proxy for the sources depth uncertainties. Since the sources cannot intersect with each other, the NGB source depth uncertainty is much narrower than the prediction of the RMS white contour.

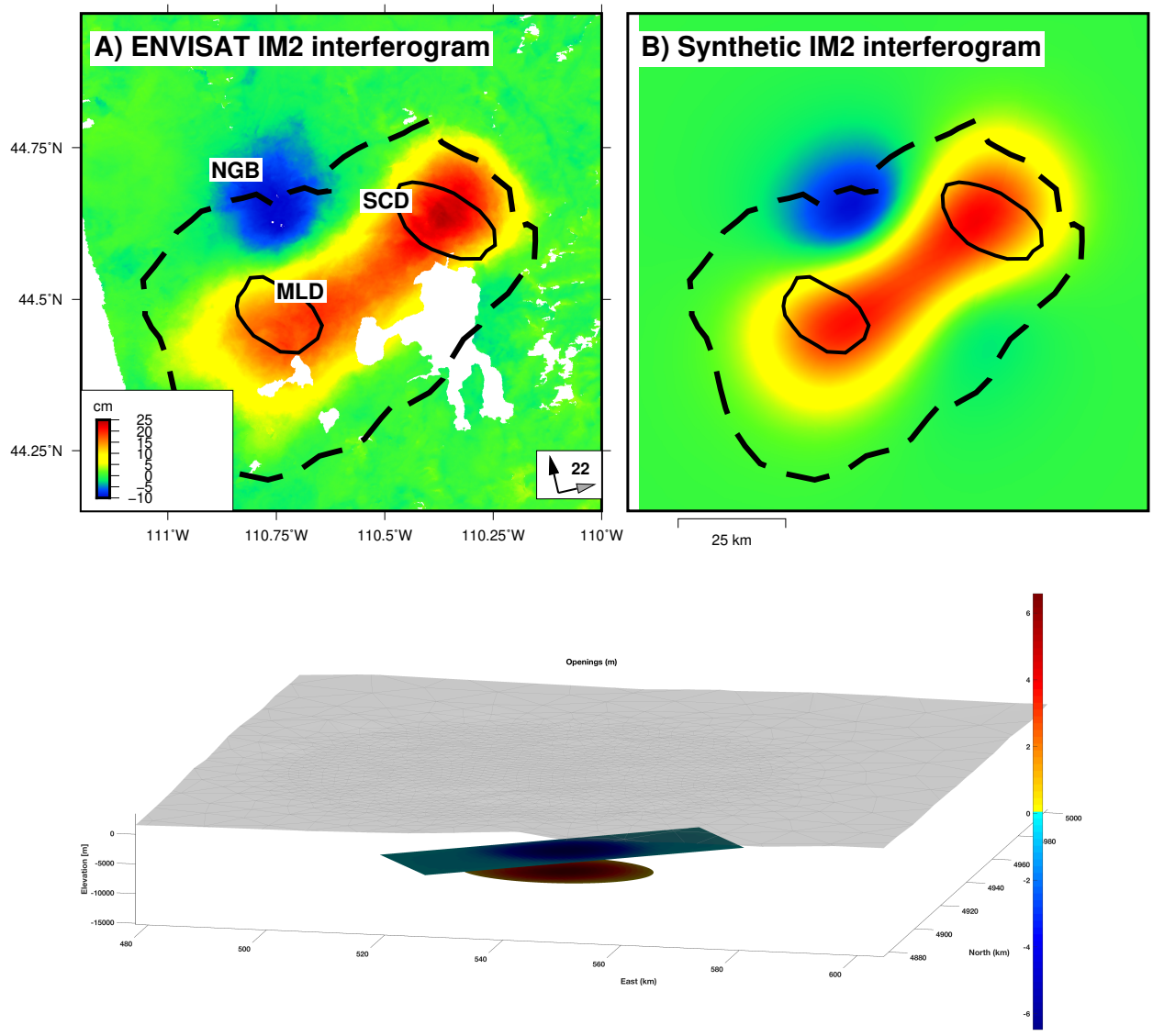


Figure S9: Boundary element model. Top. IM2 ascending ENVISAT interferogram (A), synthetic interferogram (B). Bottom. Perspective view of the boundary element caldera sill and NGB ellipsoid. Positive colors show ellipsoid closing and negative colors show sill opening.

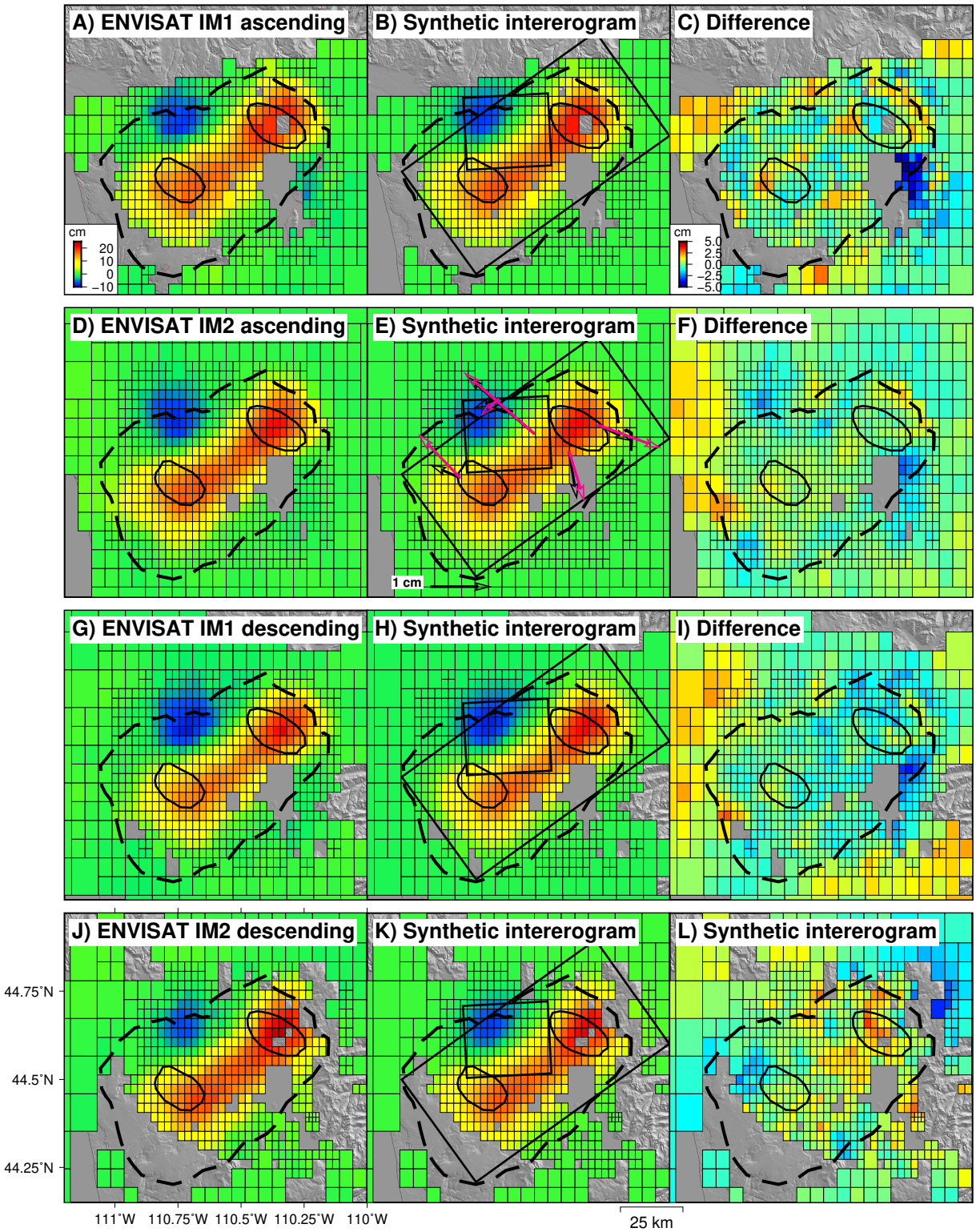


Figure S10: ENVISAT interferograms (A,D,G,J), synthetic data (B,E,H,K) and residuals (C,F,I,L) for the inversion of two sub-horizontal dislocations with distributed opening during 2005-2009 (Figure 5B). The black and pink arrows in E show the GPS vectors and predicted displacement by best-fit sill models.